Review

Corrosion behavior of severely plastically deformed Mg and Mg alloys

Ahmad Bahmani[a], Mehrab Lotfpour[b], Milad Taghizadeh[c], Woo-Jin Kim[d],*

[a] *Department of Advanced Materials and Renewable Energy, Iranian Research Organization for Science and Technology, Tehran 3313193685, Iran*
[b] *Department of Mechanical Engineering, University of Nevada, Reno, NV 89557, USA*
[c] *Department of Mechanical Engineering, Clemson University, Clemson, SC 29634, USA*
[d] *Department of Materials Science and Engineering, Hongik University, Mapo-gu, Sangsu-dong 72-1, Seoul 121-791, Republic of Korea*

Abstract

Magnesium (Mg) alloys have several advantages, such as low density, high specific strength and biocompatibility. However, they also suffer weak points, such as high corrosion, low formability and easy ignition, which makes their applications limited. Many studies have been conducted to overcome these disadvantages and further improve the advantages of Mg alloys. Severe plastic deformation (SPD) is one of the most important techniques and has great effects on the microstructure refinement of Mg alloys and improvements in their strength and formability. Several researchers have studied the corrosion behavior of SPD-processed Mg alloys in recent decades. However, these studies have reported some controversial effects of SPD on the corrosion of Mg alloys, which makes the research roadmap ambiguous. Therefore, it is important to review the literature related to the corrosion properties of Mg alloys prepared by SPD and understand the mechanisms controlling their corrosion behavior. Effective grain refinement by SPD improves the corrosion properties of pure Mg and Mg alloys, but control of the processing conditions is a key factor for achieving this goal because texture, dislocation density, size and morphology of secondary phase also importantly affects the corrosion properties of Mg alloys. Reduced grain size in the fine grain-size range can decrease the corrosion rate due to the increased barrier effect of grain boundaries against corrosion and the formation of a stable passivation layer on the surface of fine grains. Basal texture reduces the corrosion rate because basal planes with the highest atomic planar density are more corrosion resistant than other planes. Increased dislocation density after SPD deteriorates the corrosion resistance of the interior grains and thus proper annealing after SPD is important. The fine and uniform distribution of secondary phase particles during SPD is important to minimize the micro-galvanic corrosion effect and retain small grains during annealing treatment for removing dislocations.

1. Introduction

In recent decades, the energy crisis and human health have been critical issues, resulting in the development of new materials to solve these related problems. Magnesium alloys are one of these new materials that have attracted the attention of researchers [1] due to their low density (1.74 g/cm^3), high specific strength, and positive biological effects [2,3]. Thanks to these advantages, they have been utilized as structural components in a large variety of applications, such as auto- motive [4–8], electrical [6,9], railway transportation [10,11], aerospace [12,13], and biological applications [14,15]. However, their weaknesses, such as poor plastic formability and high and non-uniform corrosion behavior, remain obstacles for the widespread use of Mg alloys [16].

Severe plastic deformation (SPD) is an effective way to bring remarkable grain refinement in metals [17]. Although substantial grain refinement has been achieved via conventional/traditional methods, such as extrusion and rolling, obtaining ultrafine grains (UFGs) with high-angle grain boundaries has been difficult. However, SPD processes have the capability to produce microstructures comprised of UFGs with a high fraction of high-angle grain boundaries [17–20]. Fur-

* Corresponding author.

E-mail address: kimwj@wow.hongik.ac.kr (W.-J. Kim).

A. Bahmani, M. Lotfpour, M. Taghizadeh et al. *Journal of Magnesium and Alloys xxx (xxxx) xxx*

thermore, when conventional techniques, such as rolling and extrusion processes, are used, a significant reduction in the thickness and diameter of the products occurs, resulting in a limited use due to the reduced size constraints. In most SPD methods, it is possible to impose large amounts of strain (through the accumulation of high shear deformation) on samples without (or minimally) changing the overall dimensions [17].

Despite these remarkable characteristics of SPD-processed (SPDed) materials, industrial applications of UFG material products are still limited. Industrialized application of UFG materials depends on the capability to reduce the production cost and fabricate products on a large scale [21]. Until now, the SPDed materials have been most commonly used for biomedical, sports, and hydrogen storage applications [21,22]. However, modifications that have been made to conventional continuous processing, such as rolling, allow researchers and engineers to produce a material with no size limitations. For instance, applying a large shear force through differential speed rolling resulted in the formation of UFGed material sheets in a continuous process [23–25]. The most suitable areas for the use of UFG materials are in the field of medical implants. Ti alloys are popular materials for this design due to their high strength, good formability, high corrosion resistance, and low toxicity [26,27]. However, they suffer from a high material cost (almost 20 times higher than magnesium alloys), a secondary surgery for the removal of the implant, a surface treatment for activation *in vivo* and a higher elastic modulus than human bones (which causes the stress shielding effect). Mg alloys have attracted much attention recently regarding their low density and elastic modulus, which are much closer to human bones than other materials, such as titanium and steel. [28,29]. Moreover, the biodegradability of Mg alloys in the body, which removes the cost and inconvenience of secondary surgery for removing the implant after healing, makes them a suitable option as biomaterial implants [30–33]. Furthermore, Mg-based implants have antitumor properties (through the release of H_2 and Mg^{2+} ions *in vivo*) by catching metastatic cancer cells before they grow into tumors [34–39]. In addition to the medical fields, SPDed Mg alloys have a potential use for hydrogen storage applications [21,22,40]. This is because by reducing the grain size to the submicron or nanoscale, the H-absorption kinetics can be substantially accelerated due to the highly increased volume fraction of grain boundaries and triple junctions [41].

To the best of the authors' knowledge, from the corrosion behavior viewpoint, the first study investigating the effect of the SPD process on the corrosion behavior of Mg alloys was in 2006, in which the equal channel angular pressing (ECAP) process was applied to refine the microstructure and enhance the corrosion resistance of AZ31 alloys [42]. In 2007, the *in vitro* corrosion behavior of the ECAPed AZ31 alloy was studied by Wang et al. [43]. After approximately 15 years of research, investigations on the corrosion behavior of magnesium alloys were extended to other SPD methods, such as shot peening (ShP) [44], friction stir processing (FSP) (or friction stir welding (FSW)) [45–47],

cryogenic machining (CM) [48,49], HPT [50,51], high-ratio differential speed rolling (HRDSR) [52–54], multidirectional forging (MDF) [55–57], screw rolling (SR) or three roll planetary milling [58–60], dual directional extrusion (DDE) [61], groove pressing (GP) [62,63], laser shot peening (LSP) [64,65], high strain rate rolling (HSRR) [66,67], rotary swaging (RS) [68,69], sliding friction treatment [70,71], friction stir extrusion [72], cyclic extrusion-compression [73], ultrasonic nanocrystal surface modification [74,75], large strain extrusion machining [76–78], accumulative channel-die compression bonding (ACCB) [79], repeated upsetting process [80], surface mechanical attrition treatment (SMAT) [81,82] and accumulative roll bonding (ARB) [83,84]. In 2016, Sunil et al. [85] studied the *in vivo* performance of an ultrafine-grained AZ31 alloy prepared via ECAP. The schematic timeline evolution of several studies regarding the use of various SPD methods on the corrosion behavior of Mg alloys is shown in Fig. 1. The numbers of published papers on the corrosion behavior of Mg alloys prepared by various SPD methods are presented in Fig. 2 (a). Notably, the total number of investigations has increased during the last 15 years. The pie chart of various SPD methods in Fig. 2 (b) shows that ECAP and FSP have the highest contributions.

Regarding the lack of summarizing articles about the corrosion properties of SPDed Mg alloys and controversies over the SPD effect on the corrosion behavior of Mg alloys, in this study, the available literatures on the effects of various SPD routes on the corrosion properties of Mg alloys are reviewed, and efforts are made to understand the importance of various microstructural parameters on the corrosion behavior of SPDed Mg alloys.

2. Effects of microstructural parameters on corrosion behavior of Mg alloys

The overall corrosion reaction for Mg in aqueous solution is [90,91]:

$$Mg + 2H_2O \rightarrow Mg^{2+} + 2(OH)^- + H_2 \uparrow \qquad (1)$$

The reaction indicates that the metallic Mg is transformed into Mg^{2+}, and a molecule of H_2 is liberated during the corrosion process. The cathodic reaction of the above-mentioned reaction is hydrogen evolution, which can be written as:

$$2H_2O + 2e^- \rightarrow H_2 \uparrow + 2(OH)^- \qquad (2)$$
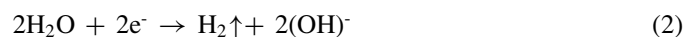
And the anodic reaction is given as:

$$Mg \rightarrow Mg^{2+} + 2e^- \qquad (3)$$

In practice, significant amounts of Mg^{2+} precipitate as $Mg(OH)_2$, which has a low solubility in water [3]. The volume of H_2 per unit time represents the rate of Mg degradation, which is called the hydrogen evolution rate. In addition to hydrogen evolution measurements, the corrosion rate of Mg alloys has been evaluated by using weight loss measurements
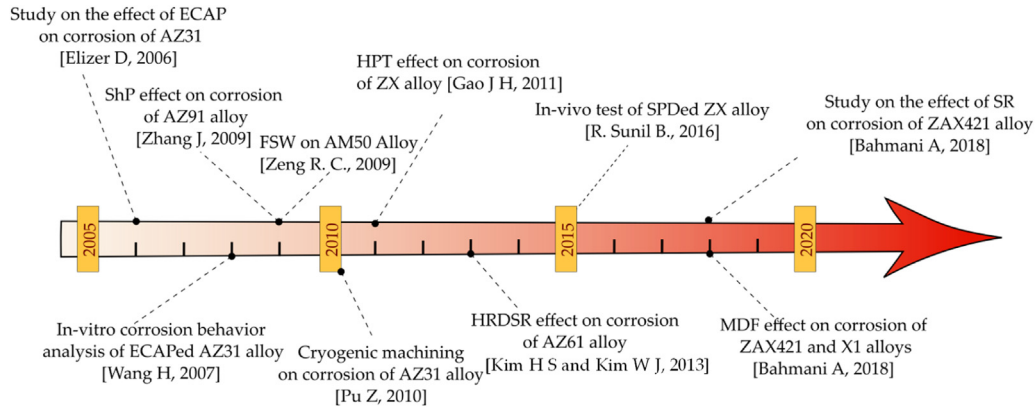
Fig. 1. Schematic timeline representations of studies that investigated the corrosion behavior of SPDed Mg alloys. The data are quoted from the references of [42–45,48,50,53,60,86,87].
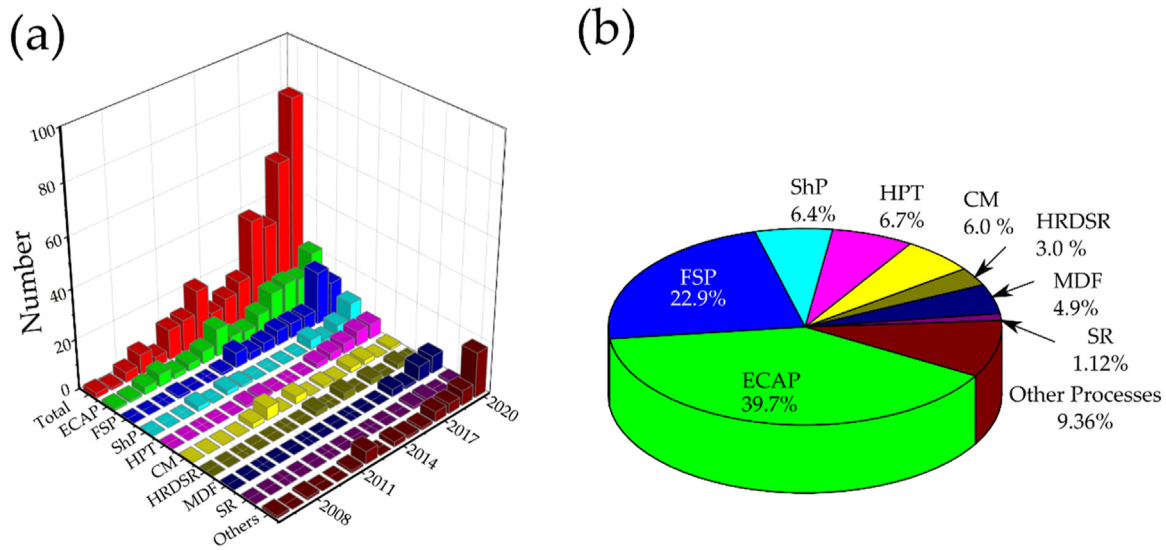

Fig. 2. (a) The number of research papers by year with the different SPD methods and (b) a pie chart of the contribution of different SPDs to the investigation of corrosion behavior. The graphs are plotted based on the statistical data extracted from the Scopous and Google Scholar websites [88,89]. All the index keywords and abbreviations are mentioned in the Table S1.

and an electrochemical analysis [3,92]. For a given corrosion environment, the chemical composition is the key parameter that determines the corrosion properties of materials. This is because addition of alloying elements can dramatically change surface potential of substrate and surface potential of secondary phase. It is well known, however, that the corrosion properties of materials can be also greatly affected by microstructure parameters even at a fixed composition [93]. Therefore, it is essential to recognize the influence of each microstructural feature on the corrosion behavior. By knowing the effect of each microstructural parameter, one can understand how a specific process and its controlling parameters, such as deformation directions, strain rate, temperature, and number of processing passes, affect the corrosion behavior of the material. Here, we have reviewed the literature explaining the effect of microstructural features on the corrosion behavior of Mg alloys. Understanding of the effect of microstructural parameters on corrosion behavior of Mg alloys is important

for depicting the effect of SPD on corrosion properties of pure Mg and Mg alloys.

2.1. Grain size

One of the most principal microstructural features is the grain size (d), which can be greatly reduced through SPD processes. Given that there are more lattice defects and dislocations at grain boundaries than inside grains, grain boundaries are expected to corrode faster during exposure to corrosive environments. Thus, grain boundaries are considered to accelerate the corrosion rate. It is then anticipated that a single crystal of pure Mg has a very low corrosion rate and that decreasing d increases the corrosion rate. There are, however, several controversial reports on the effect of grain size on the corrosion rate of pure Mg and Mg alloys [94]. Some studies have reported a reduction in the corrosion rate by increasing the grain size, while others have stated the opposite. Song
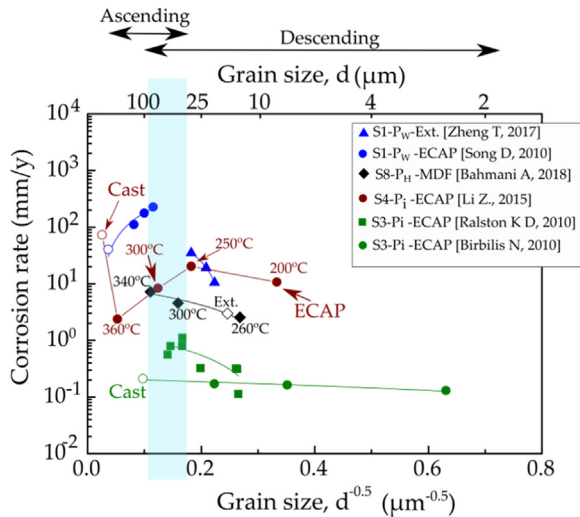
Fig. 3. Effect of the grain size on the corrosion rate of pure Mg in various studies. The data are quoted from the references of [94,95,101–105]. P_i, P_W and P_H represent the corrosion rates obtained from the electrochemical, weight loss and hydrogen evolution methods, respectively. The types of solution media have been mentioned in Table S3. Open symbols represent the initial materials (cast or extruded samples).

et al. [95] observed that the corrosion rate of pure cast Mg (*d*: 800-1500 μm) increased after the ECAP process and the authors attributed this result to the highly increased density of dislocations and lattice defects after heavy deformation via ECAP. The corrosion rate of the AZ91 alloy also increased after the SPD process, which was attributed to the accumulation of a high dislocation density and the change in the morphology of the β phase from a continuous net shape into isolated particles during the SPD process [96]. However, Chen et al. [97] reported that more effective grain refinement of Mg alloys by high strain rate rolling compared to conventional rolling resulted in a better corrosion resistance. Ralston et al. [98] introduced the relationship between the corrosion rate and the grain size with a Hall-Petch type equation, which will be called the Ralston equation here. Several researchers used this equation to explain the corrosion behavior that changed after grain refinement via plastic deformation [60,99,100].

To understand the role of the grain size on the corrosion rate of pure Mg and Mg alloys, it is better to consider its effect in pure Mg first. The corrosion behaviors of pure Mg with different grain sizes studied by several authors are summarized in Fig. 3. As seen in the plot of the corrosion rate vs. $d^{-0.5}$, the slope is positive at large grain sizes and negative at small grain sizes ($d^{-0.5} > 0.2$). This result shows that the grain-size effect on corrosion can be different even in an identical material, depending on the grain-size range. Golappudi [106] compared the corrosion rates of ECAPed pure Mg (studied by Song et al. [95] and Birbilis et al. [103]) in solutions with low and high NaCl contents (Fig. 3) and suggested that the grain size plays a different role in different solutions. In solutions with a low NaCl content, grain boundaries act as sites for releasing the mismatching energy between the surface layer and the substrate, and
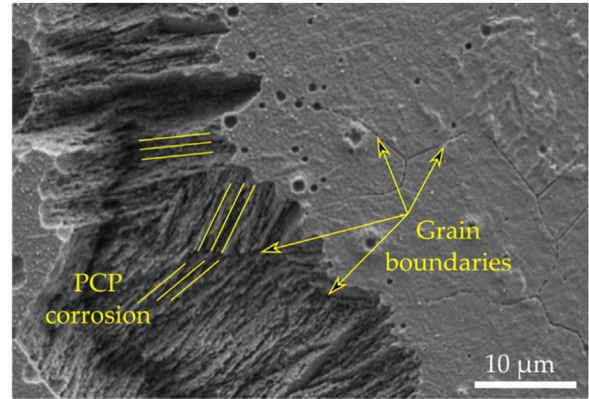

Fig. 4. PCP corrosion in extruded pure Mg after immersion in a 3.5 wt. % NaCl solution saturated with $Mg(OH)_2$ (unpublished authors' work).

hence allow the formation of a more stable and protecting layer on the surface of the Mg substrate [103]. Thus, the passivation capability becomes enhanced as the grain size decreases. However, in solutions with a high content of NaCl (such as 3.5 wt. %), passivation does not occur, and thus grain boundaries corrode faster during immersion due to the anodic effect of grain boundaries against the grain interior [103]. Grain boundaries may also play a role as corrosion barriers. It has been shown that grains were preferentially corroded parallel to close-packed planes, such as basal planes [106–108]. This type of corrosion is called preferential crystallographic pitting (PCP). An example of PCP corrosion is shown in Fig. 4, where pure Mg was immersed in a 3.5 wt. % NaCl solution media saturated with $Mg(OH)_2$ for 2 h. It can be seen that corrosion propagated on the surface by corroding the grain interiors with preferential crystallographic pitting, forming parallel lines on the grains. PCP appears to have been stopped temporarily after reaching a grain boundary to find a preferential orientation in the next grain. In this regard, the grain boundaries are considered to act as corrosion barriers [109]. Thus, when PCP is an important reactive corrosion mechanism, as the grain size is smaller, the corrosion rate is expected to decrease (Fig. 5).

Fig. 3 shows that when $d^{-0.5}$ is larger than 0.2 (i.e., $d <$ 25 μm), the corrosion rate tends to decrease regardless of the solution type and concentration, implying that effective grain refinement through SPD strongly improves the corrosion resistance. This may be because when the grain size is fine enough, uniform corrosion occurs on the surface, and grain boundaries act as barriers for PCP and stabilize the passivation layer on the surface. These issues will be discussed in detail later.

2.2. Secondary phase

The addition of alloying elements can result in the formation of a solid solution or a secondary phase based on the solubility in the matrix. The increased amount of secondary phase usually accelerates the corrosion phenomena by forming micro-galvanic cells. Then, depending on
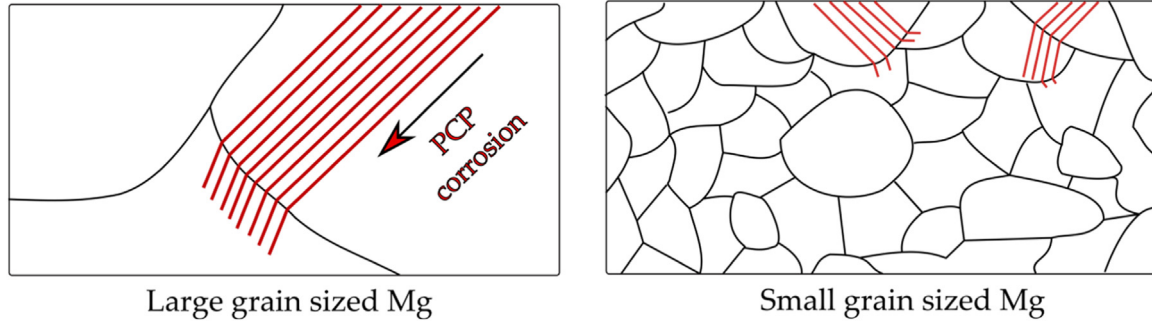
Fig. 5. Schematic representation of the effect of the grain size on the PCP corrosion mechanism [109,110].
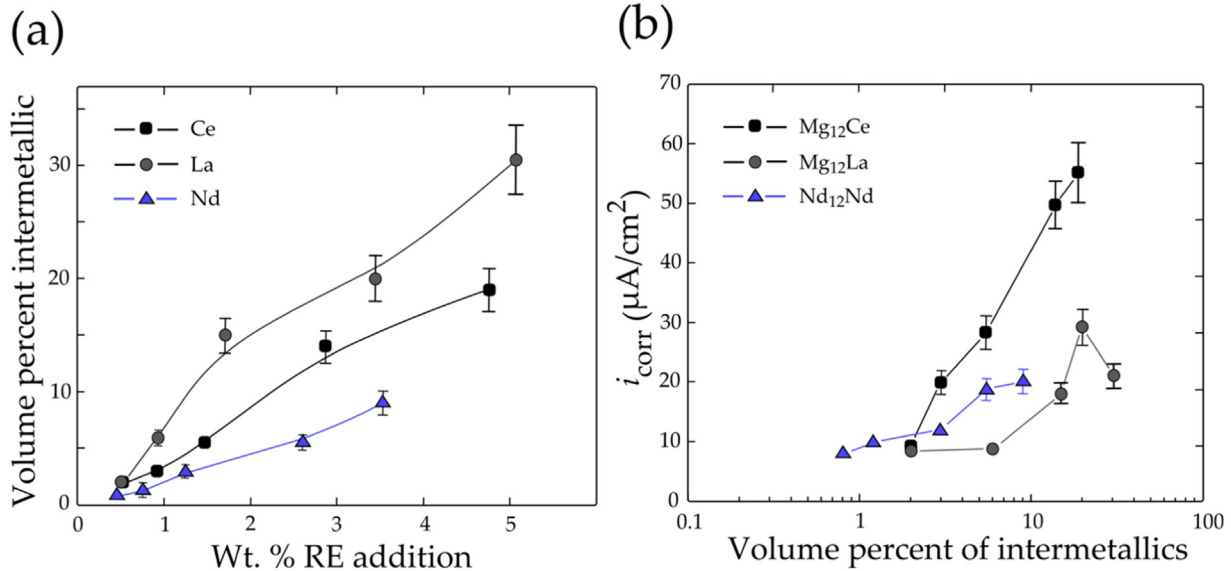

Fig. 6. Volume percent of intermetallics as a function of wt. % RE alloying addition for the HPDC Mg-Ce/La/Nd alloys [114].

the potential difference between the substrate and the secondary phase, one of them begins to degrade [94]. Therefore, the potential difference of the secondary phase compared to the Mg matrix [111–113] and the fraction, distribution, and morphology of the secondary phase are the essential parameters that determine the corrosion characteristics of Mg alloys in the presence of a secondary phase [94]. Fig. 6 shows that the volume percent of intermetallic phases in the Mg alloy increases with increasing added amounts of rare earth elements (Fig. 6 (a)), and this increase results in an increase in the corrosion current density (i_{corr}) (Fig. 6 (b)). The difference in the slopes of the i_{corr} relative to the volume percent of secondary phases may be related to the Volta-potential difference of intermetallics relative to the Mg matrix, which will be discussed later.

In addition to the fraction of the secondary phase, the secondary-phase morphology also plays a vital role in the corrosion properties of Mg alloys. When the alloy surface is in contact with the corrosive media, the anodic phase begins to degrade. As shown in Fig. 7, if the matrix functions as an anode and the secondary phase functions as a cathode, and if the cathodic phase distributes in the form of a continuously

connected network over the matrix, then the cathodic phase is expected to stop corrosion progress effectively because it is electrochemically nobler than the matrix and the anodic-cathodic circuit is cut off after degradation of the exposed matrix [115–120]. A discontinuous cathodic secondary phase, however, can act as a dispersed galvanic cell, and thus accelerate degradation. In this case, the anodic phase (Mg matrix) corrodes fast without any barrier. This is why cast Mg alloys with high concentrations of alloying elements, such as AZ91 and AZ80, with the net-shaped β phase have a low corrosion rate, while their corrosion rate significantly increases after fragmentation of the net-shaped β phase via plastic deformation [90,96].

A different story applies for the anodic secondary phase. The continuous net-like Mg_2Ca intermetallics in the cast alloys accelerate the corrosion rate because corrosion propagates inside the material by preferentially corroding the secondary phase (Fig. 7). Moreover, non-Faraday corrosion occurs in places where some parts of the matrix are removed before complete degradation. When the anodic secondary phase is discontinuous, however, these events hardly occur, and thus the corrosion rate decreases [121,122].
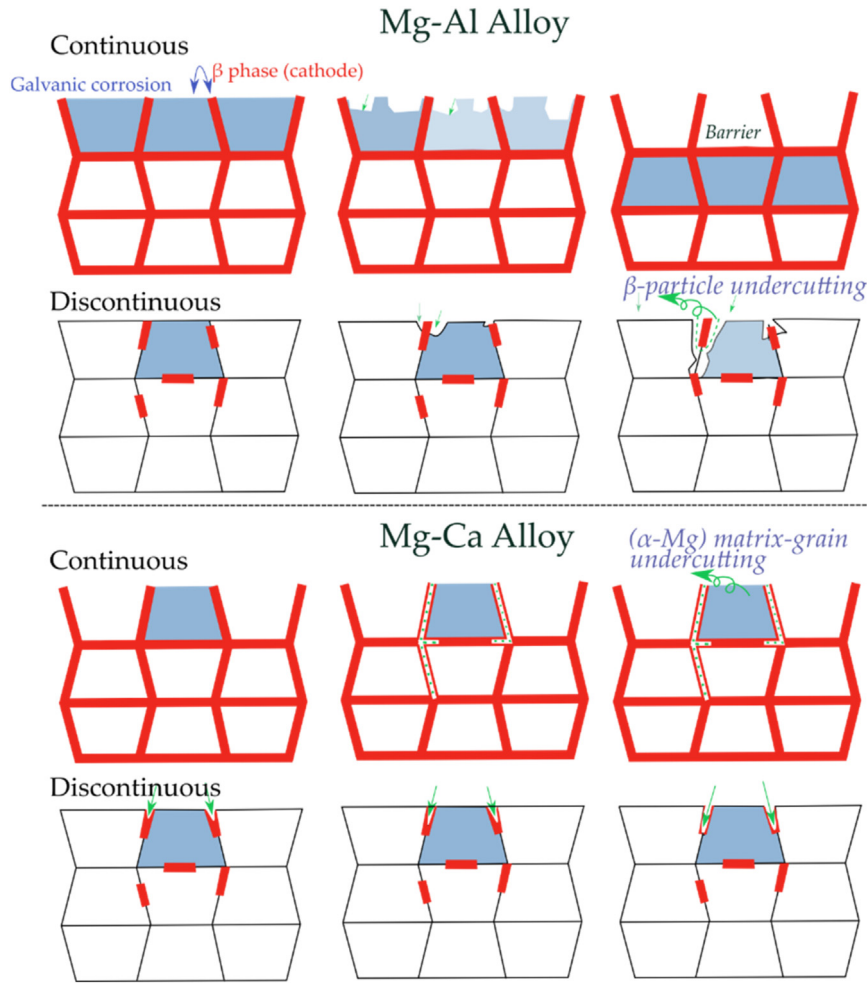
Fig. 7. Schematic representation of the morphological role of the (a) cathodic and (b) anodic secondary phases on the corrosion attack [117].

When the cathodic secondary phase is discontinuous in initial microstructure, refinement of secondary phase by plastic deformation is beneficial in improving the corrosion resistance. This is because uniform corrosion is promoted as the secondary phase is crushed into smaller particles and uniformly dispersed in the matrix. For the Mg-Zn-Ca alloys processed by HPT [123], with increasing the number of HPT revolution, not only the grain size was significantly refined, but also the secondary phase was highly broken up and distributed uniformly over the matrix. Unlike in its initial microstructure where formation of localized corrosion pits occurred due to micro-galvanic corrosion near coarse secondary phase along grain boundaries, the entire surface of the HPT-processed alloy corroded at the similar rate, indicating a change of corrosion mode from pitting corrosion to uniform corrosion after the microstructural refinement by HPT (Fig. 8).

The effect of the fraction of secondary phase and their Volta potential difference with the matrix on the corrosion behavior of Mg when the secondary phase acts as a cathode is schematically shown in Fig. 9 [94]. As the amount of secondary phase increases, more sites for corrosion are provided. As the Volta-potential difference between the sec-

ondary phase and matrix increases, the galvanic cells become more active. It is worthwhile to note that there are several methods for measuring the Volta potential difference between the matrix and secondary phase, such as the use of scanning Kelvin probe force microscopy (SKPFM) [94,113,124], the OCP measurement of each phase [111,112], and the calculation of the work function of each phase using the first principle calculation method [125–127]. Recently, an empirical model that can depict the effect of the amount of secondary phase ($f_{A,i}$) and the volta-potential difference between the matrix and secondary phase (ΔE) on the corrosion rate of Mg alloys has been proposed by Bahmani et al. [94].

2.3. Texture

Generally, each grain has its orientation, and is separated from the neighboring grains by high-angle grain boundaries. Magnesium and its alloys have a hexagonal close-packed (HCP) structure, which gives them strong anisotropic properties. Thus, the mechanical and corrosion properties of Mg alloys are dependent on the crystallographic orientation [128]. Liu et al. [129] found that grains with misorientations closer

ARTICLE IN PRESS

JID: JMAA [m5+;October 15, 2022;1:50]

A. Bahmani, M. Lotfpour, M. Taghizadeh et al. Journal of Magnesium and Alloys xxx (xxxx) xxx
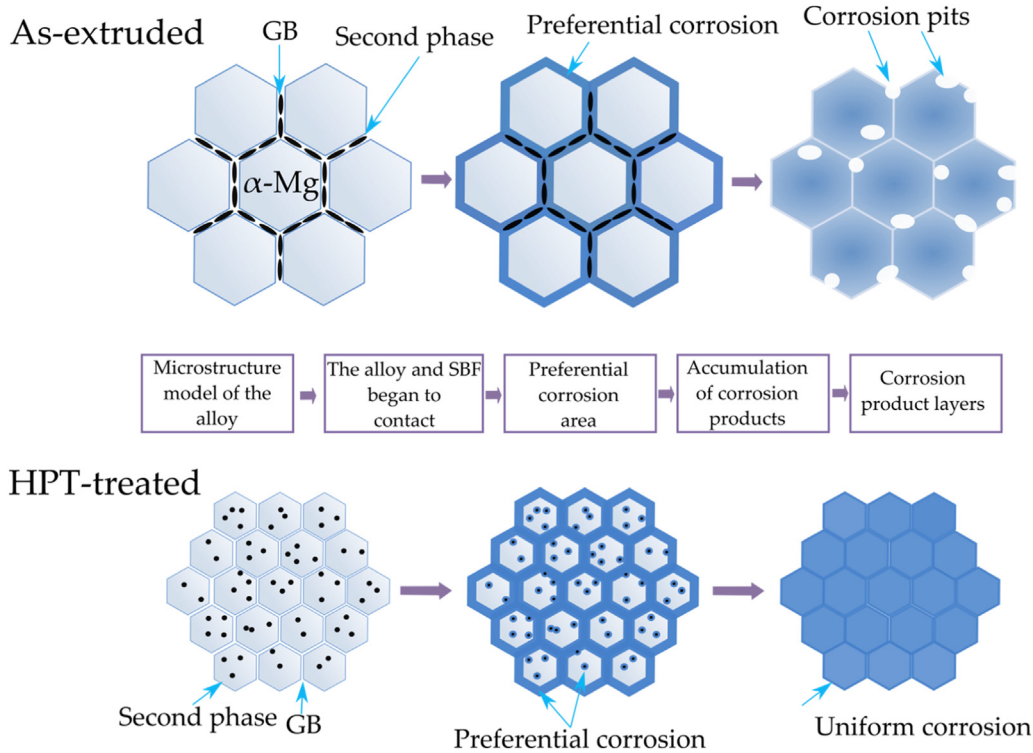
Fig. 8. Uniform corrosion enhanced by refinement of grains and secondary phase [123].
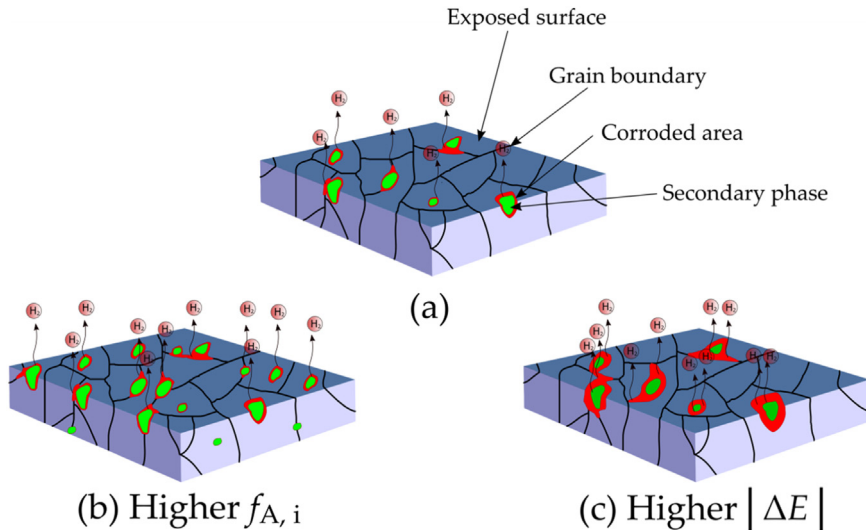

Fig. 9. Effect of the Volta-potential difference and the fraction of secondary phases on the corrosion rate: (a) corrosion of the matrix adjacent to the cathodic (secondary) phase, (b) enhanced corrosion due to the presence of a higher fraction of secondary phase (higher $f_{A,i}$), and (c) an enhanced corrosion rate due to a higher volta-potential difference between the matrix and secondary phase (ΔE) [94].

to the basal plane corroded more slowly than those with orientations far from the basal plane (Fig. 10). Moreover, research studies on a single crystal of Mg [130], Mg-Al, and Mg-Cu alloys [131] showed the dependence of corrosion progression on the grain orientations: the orientations closer to the basal and prismatic planes showed a lower corrosion than the atomic planes with less packing density. Polycrystalline Mg alloys also showed a similar orientation (texture) effect on their corrosion behavior [53,132–134]. Since the work func-

tion of grains with orientations near the basal planes is higher than that of grains with non-highly packed planes [135], a higher energy is required to remove atoms from the surface of packed planes, and hence grains with more highly packed planes have a lower corrosion rate [109,130,136]. Since the basal planes are closely packed, it is difficult to remove atoms from them, and thus it is difficult for corrosion to propagate perpendicular to the basal plane direction. Fig. 11 shows the PCP corrosion pits introduced into the matrix of Mg through
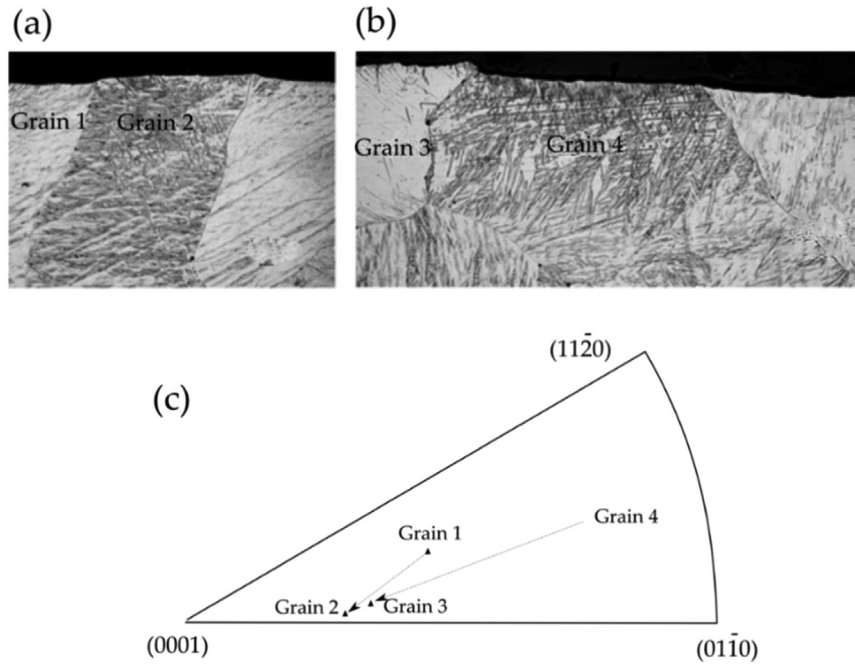
Fig. 10. (a, b) Cross section of the corroded surface showing the obvious difference in the corroded grains regarding their orientation and (c) the orientation of each grain presented in the standard stereographic triangle [129].
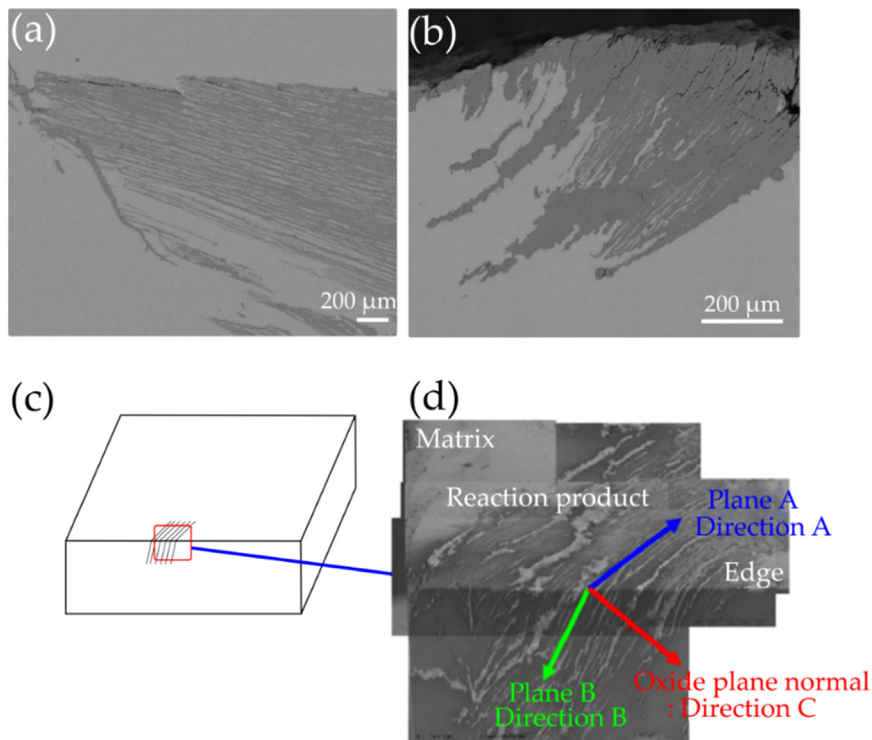
Fig. 11. (a), (b) SEM micrographs showing the areas corroded by PCP corrosion, (c) schematic of the PCP corrosion and (d) an SEM micrograph showing PCP that propagated along a preferential crystallographic orientation [109].

some lines that are parallel to the basal planes [109]. As the basal plane is the most corrosion resistance plane, dissolution might have occurred parallel (rather than perpendicular) to the basal plane. This observation suggests that if the Mg matrix with a basal texture has fine grains, then the corrosion

rate is expected to be more synergistically reduced due to the increased barrier effect of grain boundaries against PCP corrosion (Fig. 5).

Fig. 12 shows the corrosion of the extruded Mg sample immersed in 3.5 wt.% NaCl saturated with an Mg(OH)$_2$ so-

Fig. 12. SEM/EBSD analysis of the cross-sections of the extruded Mg alloy (Mg-Zn-Al-Ca-Mn alloy) after 3 h of immersion in 3.5 wt.% NaCl saturated with an $Mg(OH)_2$ solution [108].

lution. It is observed that the basal textured region (composed of subgrains with low angle grain boundaries) that faces the solution media with prismatic plane has been more locally corroded compared to the randomly orien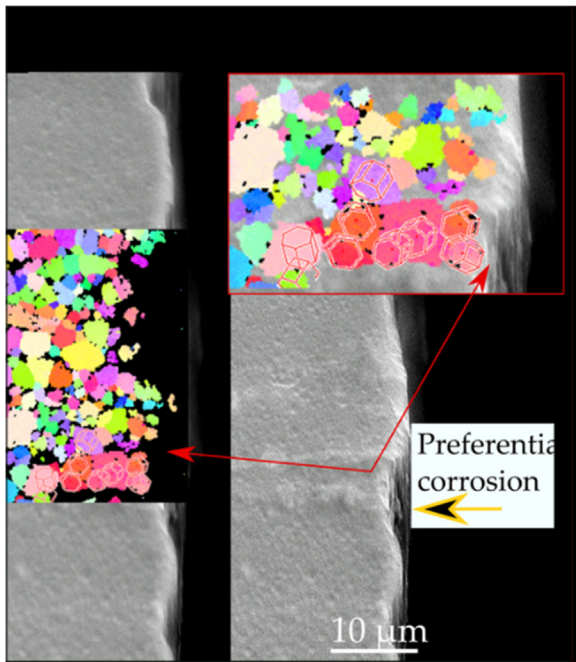ted grains with high angle grain boundaries [108]. This might have occurred because the barrier effect of subgrain boundaries was weaker than that of high angle grain boundaries, such that corrosion propagated faster into the direction parallel to the basal plane.

This result suggests the importance of the grain boundary characteristics againstPCP corrosion.

2.4. Dislocations and twins

Lattice defects such as dislocations can act as anodic sites relative to the matrix and lead to fast localized corrosion. Dislocation sites are places with fewer atomic bonds than dislocation-free zones, and thus it is easier to remove atoms there. Grains with dislocations are sensitive to degradation in corrosive media. In other words, dislocations are anodic sites relative to the matrix in the grain interior; hence, increasing the dislocation density increases the corrosion rate. For this reason, SPDed materials processed at low temperatures (with no post-annealing) with a high density of dislocations (Fig. 13) usually suffer a higher corrosion rate.

Zhang et al. [123,137] studied the corrosion behavior of Mg-Zn-Ca alloys processed by HPT and subsequently annealed at 90–270°C for 30 min and investigated corrosion resistance in simulated body fluid. Fig. 14 (a) shows the grain-size and the corrosion rate calculated based on measurements of the volume of released hydrogen as a function of annealing temperature [123] and Fig. 14 (b) show the curve of corrosion rates against $d^{-0.5}$, plotted based on the data given in (a). As the grain size increases by annealing, the corrosion rate decreases, but above 210°C where the grain-size increase is rapid, the corrosion rate increases as the grain size increases. This result may be interpreted as follows: below 210°C the effect of the decreasing dislocation density with increasing annealing temperature is higher than the effect of increasing the grain size and thus the corrosion rate decreases though the grain size increases. When the dislocation density is sufficiently reduced above 210°C, however, the increasing grain size increases the corrosion rate.
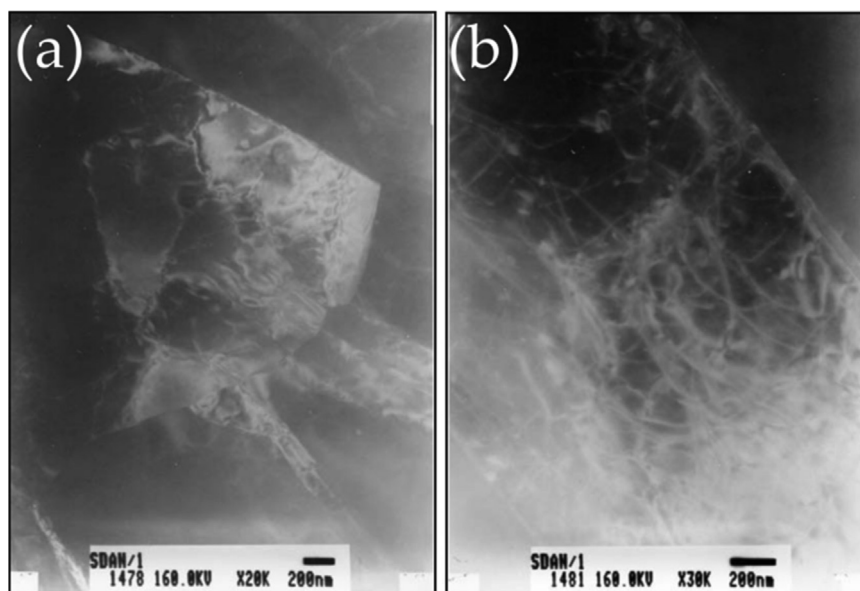

Fig. 13. TEM images of highly deformed grains in pure Mg after ECAP [95]. (a) Morphology of the grains (and subgrains) and (b) dislocation distribution in a subgrain.
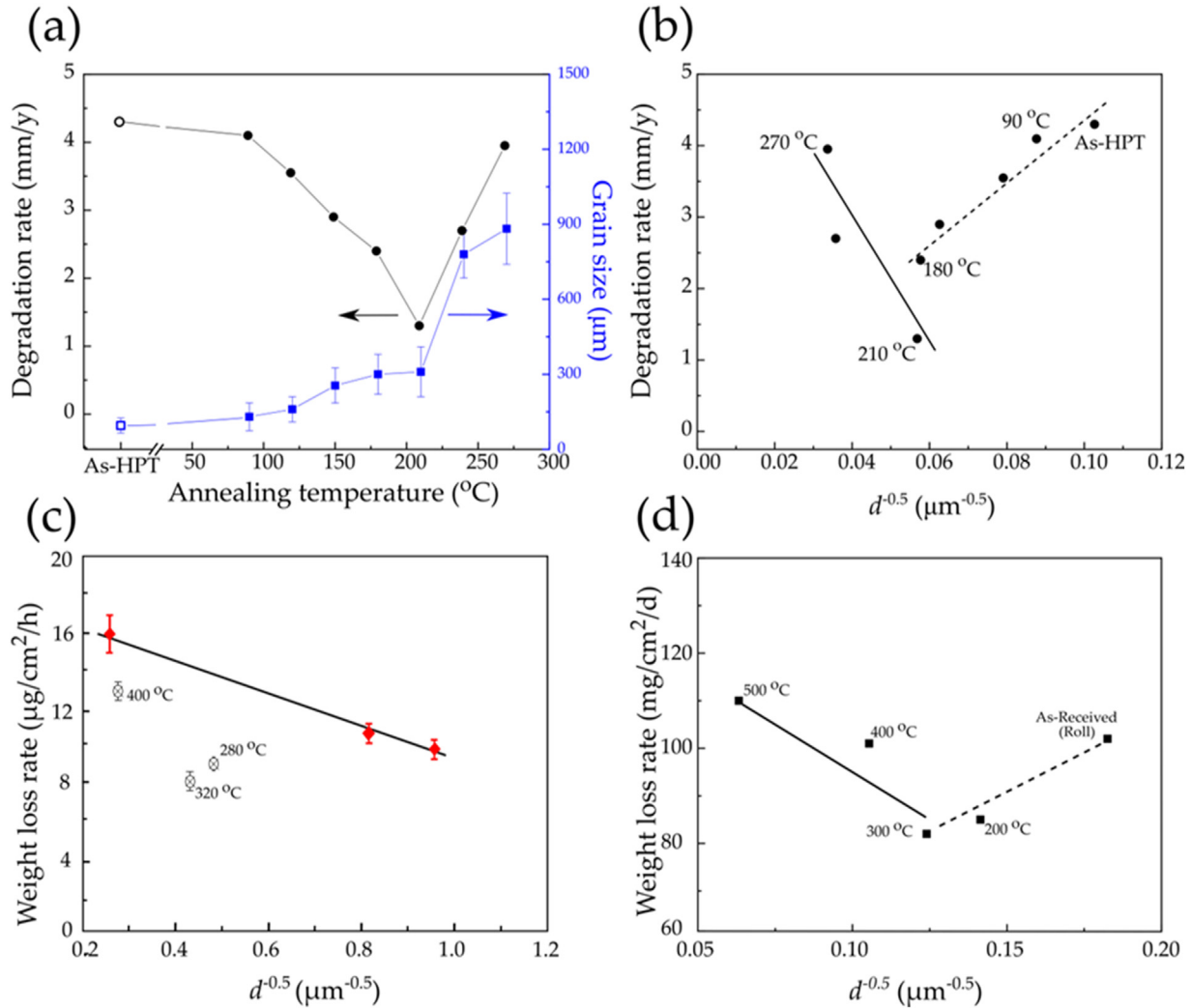
Fig. 14. (a) Degradation rate and grain size of HPT processed Mg-Zn-Ca alloy after annealing at different temperatures [137], (b) degradation rate agains $d^{-0.5}$, which is plotted based on the data in (a), (c) rates of the weight loss measured from the immersion tests on the as-received sample, the HRDSRed samples, and the annealed HRDSRed AZ61 alloy [53]. (d) Weight loss rate of as-received (hot-rolled) and annealed AZ31 alloy at 3.5 wt. % NaCl solution agains $d^{-0.5}$, which is plotted based on the data provided in the reference of [138]. The temperatures marked on the graph represent the post-deformation annealing temperatures.

Fig. 14 (c) shows the rates of weight loss obtained from the immersion tests on the as-received AZ61 alloy. The AZ61 alloy processed by HRDSR and the HRDSR-processed AZ61 alloy annealed at different temperatures are plotted against $d^{-0.5}$. The linear relationship is obtained from the rate of the weight loss, which decreases with an increasing $d^{-0.5}$. However, the linear relation does not hold when the data for the annealed HRDSRed samples are considered together. The annealed samples exhibit lower rates of corrosion than what is expected from the linear relation at the same grain size, implying that the corrosion resistance of the AZ61 alloy increases as the dislocation density substantially decreases by annealing.

Aung and Zhou [138] studied the corrosion resistance of the twinned and untwined microstructures of AZ31B alloy sheet in 3.5% NaCl solution. Fig. 14 (d) shows the grain size effect on the corrosion rate for the microstructures without deformation twins in the range of average grain size between

65 and 250 μm (annealed between 300 and 500 °C). The linear relationship is obtained from the rate of the weight loss, which decreases with an increasing $d^{-0.5}$. The samples with twinned microstructures, however, exhibit higher rates of corrosion than what is expected from the linear relation at the same grain size below d=65 μm, implying that the existence of twins accelerates the corrosion process. However, this result can be interpreted in terms of dislocation density as well because there is a high chance for the presence of high density dislocations in the as-rolled and low-temperature annealed samples. Yan et al. [139] showed that the solution-treated AZ80 alloy subjected to multi-directional compressions with 12 passes had ultrafine-grain structure consisting of dense ultrafine twins and the low corrosion rate was recorded from the ultrafine grained microstructure after aging in 3.0% NaCl solution. This result was attributed to the suppression of localized corrosion by the uniform distribution of fine β-$Mg_{17}Al_{12}$ on twin boundaries, indicating that deformation twins, which
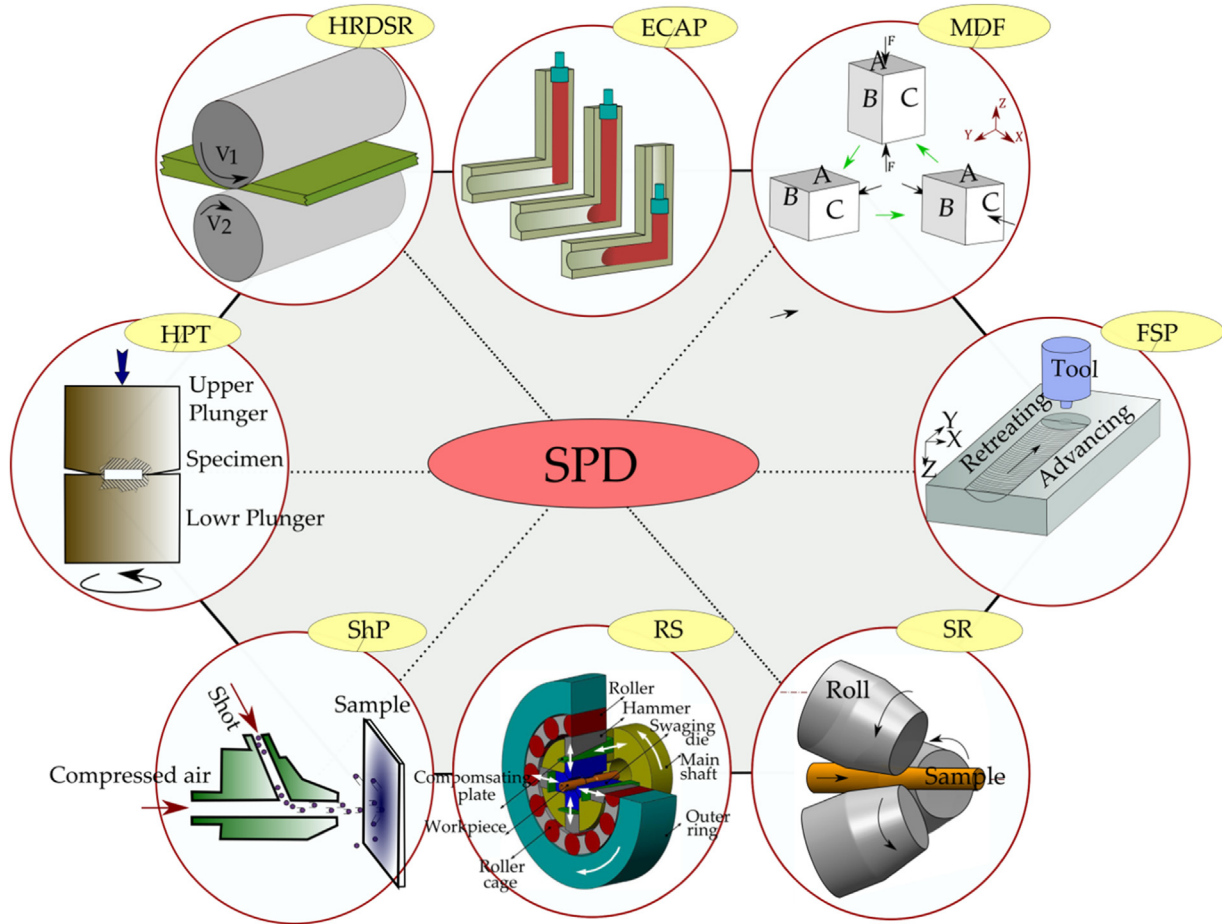
Fig. 15. Schematic representation of some popular SPD processes for producing ultrafine-grained Mg materials, including equal channel angular press (ECAP), multidirectional forging (MDF), friction stir processing (FSP), screw rolling (SR), rotary swaging (RS), shot peening (ShP), high-pressure torsion (HPT) and high-ratio differential speed rolling (HRDSR) processes [68,140–149].

are fine and densely distributed, can increase the corrosion resistance for precipitate-hardened Mg alloys by providing the nucleation sites of precipitates.

3. The SPD techniques used for corrosion studies of pure Mg and Mg alloys

To date, more than 60 methods of SPD have been developed, and it is expected that the figure will see a gradual increase in the future. The following section provides information about the most well-known SPD techniques that have been utilized to refine the microstructures of the pure Mg and Mg alloys. The schematic figures of the mentioned SPD methods are represented in Fig. 15.

3.1. Equal Channel Angular Press (ECAP)

Equal channel angular pressing or equal channel angular extrusion is one the most well-known SPD processes in which alloys are deformed through an angular channel [142,147,150,151]. The key controllable processing parameters for ECAP are the channel angle and the method of sample rotation around the centerline for the next passes [152–154].

ECAP effectively refines the microstructure through repeated cycles and modifies the texture to enhance the ductility of Mg alloys [155,156]. Either an increase or decrease in the corrosion rate after ECAP has been reported for pure Mg and Mg alloys [95,96,103,157]. Sekar et al. [158] showed that ECAP improved the resistance of galvanic corrosion in the ZE41 Mg–Al7075 galvanic couple, indicating that the ECAP process is also useful in connecting magnesium alloy components to other metals. Recently, Torkian et al. [159] applied ECAP to WE43 Mg alloys followed by extrusion and showed that ECAP plus extrusion processes considerably enhanced the corrosion resistance *in vivo* biodegradation tests (Fig. 16). The unprocessed sample with coarse grains was degraded severely during the period and thus did not exist in the body, while the ECAPed samples experienced less degradation. The degree of degradation decreased in the ECAPed samples as the ECAP pass number increased, implying that microstructural refinement effectively improved the bio-corrosion resistance.

3.2. Friction Stir Processing (FSP)

Based on the basic principles of a well-known solid-state joining process, friction stir welding (FSW), FSP has now
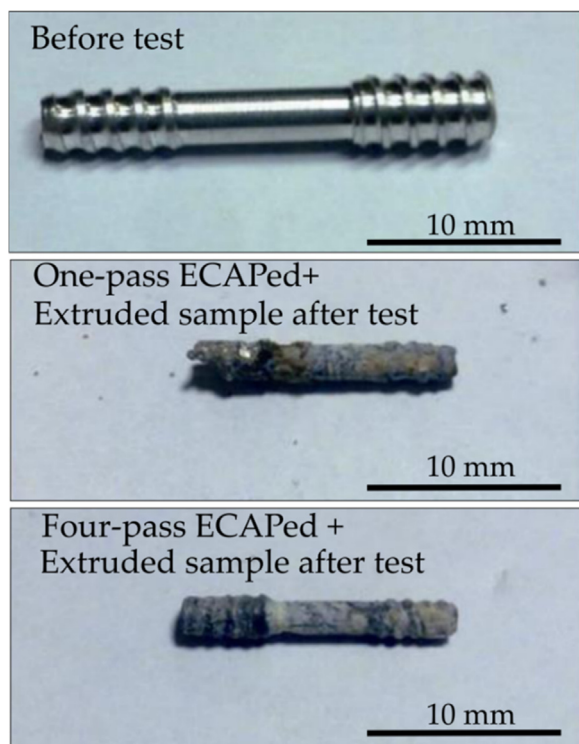
Fig. 16. The photographs of the implants before and after 12 weeks post-surgery [159].

become an effective method for the generation of an ultra-fine grained structure. In this process, a rotating pin connected to a shoulder is inserted into the material to modify its microstructure [160–162]. FSP has some benefits, making it unique among other metalworking techniques because it controls the processed zone by the length of the pin, modifies the mechanical properties by optimizing the designed tool as well as the heating/cooling rate, and performs solid-state microstructural refinement processing with homogenization in one step [145]. However, as this technique only modifies the alloy surface, improvement of bulk properties, such as tensile strength, cannot be expected for thick materials. The corrosion and surface hardness of a ZK60 alloy after FSP were studied by Liu et al. [163]. After 1 FSP pass, the grain size was reduced from 68.2 to 3.1 μm. This grain refinement resulted in a corrosion rate reduction from 12.5 to 5.0 mm/y.

3.3. High-Pressure Torsion (HPT)

HPT provides a condition in which a cylindrical specimen experiences torsional shear straining through a high hydrostatic pressure exerted by two plungers [164]. In this procedure, the small specimen is placed between the plunger and the support, and the plunger rotates and deforms the specimen through contact surface friction forces, subjecting the specimen to a high torsional strain. HPT can be performed for the desired number of turns at ambient and elevated temperatures and has become a potent scientific tool for studying the properties of SPD materials in recent years [51,164,165].

The disadvantage of this process is its limited sample size. A mixture of HPT and extrusion, which is called high-pressure torsion extrusion (HPTE) [166], has been proposed to overcome this limit. Silva et al. [165] reported that they achieved grain sizes of ∼130 and 160 nm from AZ31 and ZK60 alloys by using HPT. Parfenov et al. [167] reported that the grain size of an Mg-1Ca (X1) alloy was reduced from 42 μm to ∼ 100 nm after HPT and that grain refinement enhanced the corrosion resistance. The post-deformation annealing treatment, which increased the grain size to 1.1 μm, further decreased the corrosion rate due to dissolution of the large Mg_2Ca phase and the precipitation of nano-sized Mg_2Ca particles instead. Removal of dislocations via annealing can be another reason behind the enhanced corrosion resistance.

3.4. High-Ratio Differential Speed Rolling (HRDSR)

HRDSR is a modification of the conventional rolling process, or equal speed rolling (ESR), in which the upper and lower rollers rotate at different speeds. The ratio of the upper to lower roller speeds, defined as the speed ratio coefficient (R), is a key factor determining the final microstructure and hence the mechanical and corrosion properties [23,168,169]. The SPD effect has been often achieved at R≥2. The amount of shear strain increases with an increasing speed ratio. A higher amount of shear strain compared to ESR, which has been proven through FEM [24] and experimental analyses [170], results in an effective grain refinement and uniform dispersion of the fragmented secondary phase [171]. HRDSR has been demonstrated to be efficient in enhancing the mechanical properties of Mg alloys [172–181]. For instance, Kim et al. [168,182,183] showed that the HRDSRed AZ31 alloy had an exceptionally high yield strength of 380 MPa due to effective grain refinement and the strengthened basal texture, which is the highest yield strength of the AZ31 alloy to date. On the other hand, the ultrafine-grained HRDSRed Mg–9.25Zn–1.66Y alloy with an icosahedral quasicrystalline phase that is stable at high temperatures exhibited excellent superplasticity at elevated temperatures [184]. The above-mentioned advantages and capability of being used as a continuous process [25] make HRDSR an effective technique to produce SPD Mg materials in sheet form [146]. Kim and Kim [53] showed that after HRDSR on an AZ61 alloy, the corrosion rate in a 0.1 M NaCl solution (through a weight loss measurement) decreased from 0.81 to 0.50 mm/y. The corrosion rate was further decreased after subsequent annealing, despite the grain growth, due to the removal of dislocations from the interior grains. Seong and Kim [185] showed that the effective grain refinement and uniform dispersion of the nano-sized Mg_2Ca phase particles and formation of strong basal texture during the HDRSR process and the effective removal of dislocations by post-HRDSR annealing with minimizing grain growth can greatly improve the bio-corrosion resistance of Mg-Ca alloys. Fig. 17 shows the optical photographs of the HRDSR-processed Mg-Ca alloy sheets and the microstructure obtained by post-HRDSR annealing.
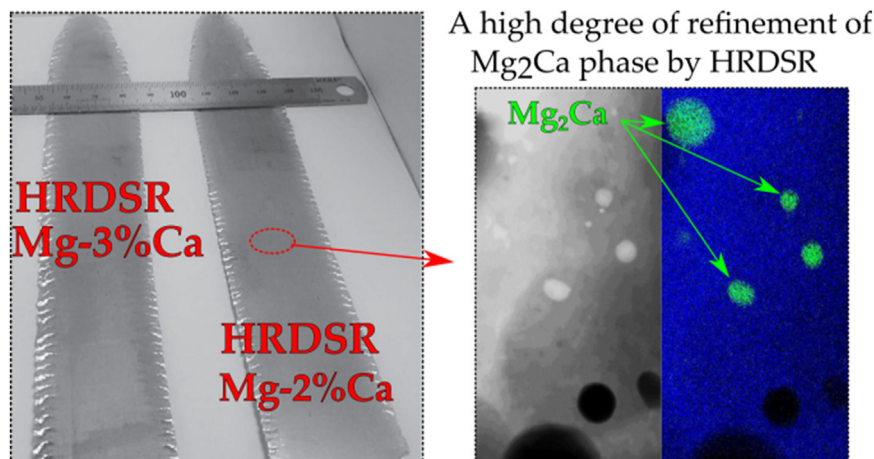
Fig. 17. The optical photographs of the HRDSR-processed Mg-Ca alloy sheets and the TEM micrographs for the HRDSR-processed samples after annealing [185].

3.5. Accumulative Roll Bonding (ARB)

The accumulative roll bonding (ARB) process was invented by Saito et al. [186] as an effective SPD method to provide ultra-fine grain structures without geometrical changes. During ARB process, a considerable amount of shear and compressive strain is accumulated [187]. ARB process is a profitable deformation method to manufacture large sheets with ultra-fine grain structure.

Limited studies on corrosion properties of the ARB-processed Mg alloys have been conducted. Pei et al. [188] found that ARB process resulted in significant refinement of grains and $Mg_{17}Al_{12}$ phase in the AZ63 alloy, leading to a decrease in micro-galvanic corrosion. Samiei et al. [189] investigated the effect of the ARB process on the microstructure, mechanical, and corrosion properties of the AZ31 alloy. Applying ARB resulted in remarkable enhancement of yield strength and hardness. The corrosion properties of the AZ31 alloy was, however, deteriorated after ARB due to the highly increased dislocation density.

3.6. Multi-Directional Forging (MDF)

MDF is a relatively low cost method that is suitable for large bulk components and can be performed without any special tools, making it appropriate for many potential applications. The process is also known as Multi-Axial Forging (MAF) [190–192] or Multi-Axial Deformation [193]. The MDF is comprised of three main steps. The deformation begins with applying a load in the first direction known as X-direction, and with rotating the cubic sample by 90° along its Z-direction, the material experiences a Y-directional deformation. The final stage relates to a ninety-degree rotation along the X-direction and exerting a load in the Z-direction. These three steps are repeated. MDF can be processed with or without a die [144,191,194–196]. However, due to the friction effect between the die and the sample, inhomogeneous deforma-

tion can occur, leading to an inhomogeneous microstructure in the specimens [144,197]. Researchers have achieved very high strength for an AZ61 alloy using this technique (UTS: 550 MPa), which is the largest value in the time of publishing data for Mg alloys. The elongation of this sample was 26%, which is also large for Mg alloys [198]. These results represent the capability of this process for producing effective grain refinement and texture randomization in Mg alloys. A low corrosion rate of 0.25±0.05 mm/y was recorded from the alloy processed by MDF, which is lower than that of high purity Mg and almost equal to that of ultra-purity Mg in a 3.5 wt. % NaCl solution saturated with $Mg(OH)_2$ [56,87,199]. This corrosion rate enhancement has been attributed to the uniform distribution of grain size and secondary phase particles in the matrix.

3.7. Rotary Swaging (RS)

As a hammer forging method for reducing the cross-section of pipes, wire, or billets, RS is an efficient technique to achieve superior mechanical properties while minimizing processing costs and decreasing metal losses. Samples processed by this procedure will have an excellent surface quality and condensed structures, with dimension tolerances that are more precise compared to other deformation methods, such as extrusion. As shown in Fig. 15, the quickly rotating dies swage the billet in the axial direction, providing permanent peripheral swaging in a continuous process. In recent years, RS has been considered an efficient technique for producing UFG structures, since it has shown an excellent potential for the SPD of steel, aluminum, titanium, and magnesium [68,148,200]. Martynenko et al. [148] utilized the RS process for the grain refinement of a WE43 alloy. The grain size decreased from 61.3 to 0.6 µm after RS. The highest yield strength (287 MPa) was achieved after RS at 325°C. The corrosion rate (measured by the hydrogen evolution method)

ARTICLE IN PRESS

JID: JMAA [m5+;October 15, 2022;1:50]

A. Bahmani, M. Lotfpour, M. Taghizadeh et al. Journal of Magnesium and Alloys xxx (xxxx) xxx
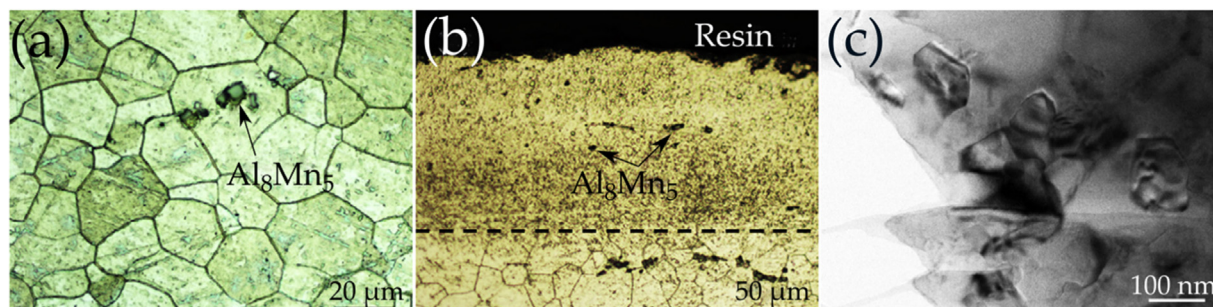
Fig. 18. Microstructures of the (a) as-received and (b, c) SShp treated AZ31 Mg alloy [209].

slightly decreased after RS (from 0.87 ± 0.21 to 0.73 ± 0.24 mm/y).

3.8. Screw Rolling (SR)

The process of Screw Rolling [60,201], also known as Radial-Shear Rolling (RSR) [141,143,202], three roll planetary milling [59,203,204] or three roll planetary rolling [205], is illustrated in Fig. 15. In this method, a material with a round cross-section undergoes a reduction in thickness by three planetary rolls. The SR can be an efficient technique for alloys that are difficult to deform. From the beginning, SR has been introduced as a process of intense plastic deformation for the structuring of long components, such as rods and pipes. The bulk shear, which is created by the helicoid motion of the material in the deformation region over determined trajectories, leads to a controllable increase in the material temperature. The temperature rise (100–150°C) then results in the elimination of the intermediate heating, thereby reducing the heat needed before rolling and saving energy. The amount of energy and force required for deformation is 12–15 times less in SR than in longitudinal rolling with a comparable reduction [143]. A significant improvement in yield strength of pure Mg [59] (from 52 to 140 MPa) was achieved. The grain size was reduced from 43 μm to approximately 1–3 μm after 11 passes by SR. The yield strength of the ZAX421 alloy was enhanced after SR from 225.3 to 308.6 MPa due to grain refinement and uniform dispersion of secondary phases. The corrosion rate decreased after SR. The best corrosion rate was achieved at the processing temperature of 300°C where the secondary phase distribution, grain size, and dislocation density were simultaneously well controlled [60].

3.9. Severe Shot Peening (SShP)

Derived from a surface treating technique known as conventional air blast shot peening (CABSP), SShP has now become one of the most effective and least demanding methods of SPD. In this process, the surface of the material is subjected to high-energy shots whose size and speed are adjustable, making it a suitable technique for various applications. This introduces numerous defects, dislocations, and grain boundaries onto the surface of the workpiece and transforms the coarse grains into nanostructures. Compared with other SPD techniques, SShP does not involve dimensional restrictions on the surface of the material, and has shown a high potential in improving both the mechanical and physical properties of metals in terms of hardness, fatigue strength, corrosion, and wear. This method has been applied to a wide range of materials, including stainless steels, cast iron, and aluminum alloys [140,206–208]. Liu et al. [209] shot peened AZ31 and AZ91 wrought alloys. The grain size of the surface of the AZ31 alloy was reduced from 32.5 μm to 130 nm (Fig. 18). The depth of the grain refinement due to shot peening was approximately 130 μm. The hydrogen evolution study showed that the corrosion rate of the as-received AZ31 alloy decreased from 18.8 to 8.8 mm/y in a 3.5% NaCl solution after 30 h of immersion. Bagherifard et al. [210] shot peened an AZ31 alloy and found that SShP enhanced the surface hardness from approximately 42 to 105 Hv due to effective grain refinement, but the corrosion rate was largely increased due to the development of residual stress in the damaged layer.

4. Effect of grain size (and other microstructural parameters) on corrosion rate of SPD-processed pure Mg and Mg alloys

The corrosion rates of pure Mg and Mg alloys subjected to various SPD processes as a function of the grain size is shown in Fig. 19. The related processing and testing conditions, grain size and mechanical properties are summarized in Table 1.

4.1. Corrosion rates of MDF processed Mg alloys

The data of pure Mg and Mg alloys subjected to MDF are shown in Fig. 19 (a). As seen for the majority of the studies, the corrosion rate decreased after MDF. The corrosion rate of the cast-homogenized Z6 alloy was significantly reduced after MDF from 0.92 to 0.36 mm/y after 5 days of immersion in 0.1 M NaCl [211]. The corrosion rate of pure Mg [94] shows the grain size effect on the corrosion rate in the absence of secondary phases and impurities. The corrosion rate of pure Mg increased after MDF at high temperatures (MDF at 300 and 340°C) due to grain growth and decreased after MDF at a low temperature (260°C) due to effective grain

Table 1
Corrosion and mechanical properties of various SPDed Mg alloys.

Type of SPD	Alloy	Grain Refine. (μm)	CR Trend by SPD	CR before SPD	Lowest CR after SPD	Method	Solution	Duration (h)	SPD condition	Best mechanical properties			Refs.
										UTS	YS	El	
ECAP	Pure Mg	1150 to 75	Inc.	5.04	120.96 (P#1)	P_w	S1, T1	6	- ECAP • Pass No: 6 • Pass speed: 0.5 mm.s^{-1} • T: 573 K				[95]
ECAP	AZ91	50 to 25	Inc.	2.52	60.48 (P#1)	P_w	S1, T1	48	- ECAP • Pass No: 12 • Pass speed: 0.5 mm.s^{-1} • T: 523 K				[266]
ECAP	AZ80	50.2 to 6.4	Inc. and Dec.	34.27	13.71 (Φ:110°, P#3)	P_i	S1, T1	As-immersed	- Homogenization: 400 °C, 18 h • ECAP • Pass No: 4 • Pass speed: 1 mm.s^{-1} • T: 598 K • Φ: 90° and 110°	492.08 (Φ: 90°, P#3)		27.63 (Φ: 110°, P#2)	[262]
ECAP	WEZK2200	1.12 to 0.25	Inc.	0.13	0.92 (P#1)	P_i	S2, T2	As-immersed	- Prepared by powder metallurgy - Extrusion • T: 250-400 °C • Ratio: 1:17 - ECAP • Pass No: 4 • T: 577 K • Φ: 90° • Ψ: 20°	307 (P#4)	303 (P#4)	11.4 (P#3)	[267]
ECAP	LAE422	21 (Extrusion) to 1.7	Dec.	6.03	5.23 (P#12)	P_w	S3, T1	168	- Extrusion • T: 350 °C • Ratio: 1:22 - ECAP • Pass No: 12 • T: 185-230°C • Pass speed: 5-10 mm·min^{-1} • Φ: 90° • Ψ: 0°				[268]

Table 1 (*continued*)

Type of SPD	Alloy	Grain Refine. (μm)	CR Trend by SPD	CR before SPD	Lowest CR after SPD	Method	Solution	Duration (h)	SPD condition	Best mechanical properties			Refs.
										UTS	YS	El	
ECAP	Mg-Y-Zn	170 (Cast) to 7	Dec. and Inc.	2.54	1.43 (P#8)	P_H	S4, T2	144	- ECAP • Pass No: 8 • T: 380°C • Pass speed: 5-10 mm·min^{-1} • Φ: 90˚ • Ψ: 0˚				[157]
ECAP	ZE41A	5 (P#8) to 2.5 (P#60)	Dec.	0.04	0.005 (P#60)	P_i	S2, T1	192	- ECAP • Pass No: 8, 16, 60 • T: 603 K				[216]
ECAP	ZK60	85 (Cast) to 1.95	Dec.	0.96	0.59	P_i	S3, T1	As-immersed	- ECAP and Extrusion • Pass No: 1 • Extrusion strain: 3.4 • ECAP strain: 2	351 (ECAP)	310 (ECAP)	17.1 (ECAP)	[152]
ECAP	Pure Mg	125 (Cast) to 2.6	Dec.	0.24	0.15 (P#8)	P_i	S3, T1	As-immersed	- ECAP • Pass No: 8 • T: 250°C • Φ: 90˚ • Route: B_c				[269]
ECAP	AZ31	47 (homogenized) to 3	Dec.	16.5	5.5 (P#4)	P_w	S4, T1	72	- Annealing: 340°C, 30 min • ECAP • Pass No: 4 • T: 300°C • Route: B_c				[85]
ECAP	Pure Mg	250 (Rolled) to 22	Neut.	1.02	1.02	P_i	S5, T2	As-immersed	- Hot roll - ECAP • Plastic strain: 0.76 • Pass No: 2 • T: 275°C • Pass No: 4 • T: 250°C	160	40	10	[270]

Table 1 (continued)

Type of SPD	Alloy	Grain Refine. (μm)	CR Trend by SPD	CR before SPD	Lowest CR after SPD	Method	Solution	Duration (h)	SPD condition	Best mechanical properties			Refs.
										UTS	YS	El	
ECAP	ZK60	7.5 (Extruded) to 0.7	Dec.	1.38	1.29	P_i	S5, T2	As-immersed	- ECAP - Plastic strain: 0.76 • Pass No: 4 • T: 250°C • Pass No: 4 • T: 150°C • Pass No: 4 • T: 100°C • Φ: 110˚ • Ψ: 20˚	340 (extruded alloy)	280 (extruded alloy)	33 (ECAPed alloy)	[270]
ECAP	AZ31	35 (Annealed) to 3.5	Inc.	1.66	2.10 (P#8, 300˚C)	P_H	S6, T2	24	- Annealing: 723 K, 24 h - ECAP • Pass No: 8 • Pass speed: 4 mm.s^{-1} • Plastic strain: 0.76 • T1: 573K • T2: 423K				[215]
ECAP	ZEXM2110	60 (Cast) to 0.75	Inc.	0.63	0.91	P_i	S2, T2	As-immersed	- ECAP • Pass No: 12 • Pass speed: 0.5 mm.s^{-1} • T1: 573K	225	170	12.5	[271]
ECAP	WE43	25 (Extrusion) to 10	Dec. and Inc.	0.38	0.14 (P#1)	P_w	S2, T2	336	- Homogenization: 500°C, 18 h - Extrusion • Preheated: 460°C, 2 h • Ratio: 64 • T: 460°C • ECAP • T: 250°C • Route: B_c • Pass No.: 3	380 (P#3)	300 (P#3)	20.9 (extruded)	[214]
ECAP	Pure Mg	1500 (Cast) to 9	Dec. and Inc.	2.87	0.09 (P#4, 360 °C)	P_H	S4, T2	504	- ECAE • Route: A • Pass No.: 3 • Φ: 90 ˚ • Ψ: 20 ˚ • Pass speed: 7 mm.s^{-1}	162 (P#1, 360°C +P#3, 200°C)	58 (P#1, 360°C +P#3, 200°C)	15.9 (P#1, 360°C +P#3, 200°C)	[102]

ARTICLE IN PRESS

Table 1 (*continued*)

Type of SPD	Alloy	Grain Refine. (μm)	CR Trend by SPD	CR before SPD	Lowest CR after SPD	Method	Solution	Duration (h)	SPD condition	Best mechanical properties			Refs.
										UTS	YS	El	
HPT	ZX20	97 μm (cast alloy) to 1.2 μm	Dec.	12.11	0.08 (HPT)	P_i	S4, T2	As-immersed	• HPT • Pressure: 5 Gpa • T: room • Pass No: 5				[50]
HPT	X1	42 μm (Homogenized alloy) to 0.1 μm	Dec.	19.74	1.09	P_w	S7, T2	768	• Homogenization: 450°C, 12 h • HPT • T: room • Pressure: 6 GPa • Pass No: 10 • Annealling: 250°C, 6 h				[219]
HPT	Pure Mg, AZ31, AZ91, ZK60	1000 μm (cast pure Mg) to 0.51 μm	Inc.	0.4 (cast pure Mg)	0.6 (HPT AZ31)	P_i	S1, T1	As-immersed	• HPT • T: room • Pressure: 6 GPa				[165]
MDF	ZK40	400 μm to 8 μm	Dec.	4.59	3.82	P_H	S4, T2	48	- Preheated: 300 ˚C, 3 h - Homogenization: 375 ˚C, 16 h - Bi-directional forging (BDF) • -Speed: 10 mm.s^{-1} • T: 375 ˚C for 15 min • Strain: 2	226.3		15.3	[272]
MDF	Z6	510 to 3.8	Dec.	0.88	0.36	P_H	S2, T2	120	- Homogenization: 400 ˚C, 24 h - MDF • Speed: 0.03 mm/s • Pass No: 3	193 (MDF)	138 (MDF)	7 (MDF)	[211]
MDF	ZGX420	65 to 1.8	Dec.	2.92	0.42 (P#1)	P_H	S1, T1	148	- Homogenization: 430 ˚C, 16 h, 510 ˚C, 20 h - MDF • T: 350 ˚C • Pressure: 350 KN • Speed: 2.4 KN/s • Pass No: 1, 3, 6				[263]
MDF	Pure Mg	16.5 to 13.8	Dec. and Inc.	2.97	2.55	P_H		168					[94]

Table 1 (*continued*)

Type of SPD	Alloy	Grain Refine. (μm)	CR Trend by SPD	CR before SPD	Lowest CR after SPD	Method	Solution	Duration (h)	SPD condition	Best mechanical properties			Refs.
										UTS	YS	El	
MDF	ZAX441	2.11 (extrude) to 1.5 (MDF-180°C)	Dec.	1.74	0.57	P_H	S8, T1	168	- Homogenization: 280°C, 0.5 h • Extrusion: T= 260°C • Ratio: 10:1 • Speed: 5 mm/s - MDF • Strain rate: $3 \times 10^{-3} s^{-1}$ • Strain of $\Sigma\dot{\varepsilon}= 2.7$ • Pass No: 9 • T: 180, 300°C				[108]
MDF	ZAX421	2.6 (extrude) to 1.14 (MDF-180°C) and 2.3 (MDF-300 °C)	Dec.	1.65	0.69	P_H	S8, T1	168	- Homogenization: 280°C, 0.5 h • Extrusion: T= 260°C • Ratio: 10:1 • Speed: 5 mm/s - MDF • Strain rate: $3 \times 10^{-3} s^{-1}$ • Strain of $\Sigma\dot{\varepsilon}= 2.7$ • Pass No: 9 • T: 180, 220, 260, 300°C	327	269		[57]
MDF	X1	3.4 (Extrusion) to 1.38 (MDF-220 °C) 3.44 (MDF-300 °C)	Dec.	1.09	0.25 (MDF300)	P_H	S8, T1	168	- Homogenization: 280°C, 0.5 h • Extrusion: T= 260°C • Ratio: 10:1 • Speed: 5 mm/s - MDF • Strain rate: $3 \times 10^{-3} s^{-1}$ • Strain of $\Sigma\dot{\varepsilon}= 2.7$ • Pass No: 9 • T: 220, 260, 300 and 340°C	202.72 (MDF220) 174.11 (MDF300)	241.01 (MDF220) 223.21 (MDF300)	12.32 (MDF220) 16.87 (MDF300)	[87]
MDF	WE43	64.9 μm (extruded alloy) to 0.93 μm	Dec.	2.16	1.58	P_w	S9, T1	336	- Homogenization: 525 ˚C, 8 h - Extrusion • T: 430 ˚C • Ratio: 6.6 - MDF • pass No: 28 • Strain: 17.5 • - T: 450 ˚C to 300 ˚C				[213]

ARTICLE IN PRESS

Table 1 (*continued*)

Type of SPD	Alloy	Grain Refine. (μm)	CR Trend by SPD	CR before SPD	Lowest CR after SPD	Method	Solution	Duration (h)	SPD condition	Best mechanical properties			Refs.
										UTS	YS	El	
HRDSR	Mg-Ca	350 μm (cast alloy) to 6.32 μm	Dec.	12.09 (cast alloy)	0.04	P_w	S2, T2		- Homogenization: 370 ˚C, 8 h - Extrusion • T: 350 ˚C • Ratio: 19.6 • HRDSR • Roll-speed ratio: 2 • T: 200 ˚C • - Pass No: 6				[185]
HRDSR	Mg-1.6Mn	95 μm (cast alloy) to 4 μm	Dec.	0.43	0.17	P_i	S3, T1	As-immersed	- HRDSR • Speed ratio: 3 • Thickness reduction: 67% • - Pass No: 2				[273]
HRDSR	AZ31	20 μm (extruded alloy) to 0.6 μm	Dec.	0.32	0.16	P_w	S5, T1	144	- HRDSR • Roll-speed ratio: 2 • T: 150 or 200 ˚C • - Thickness reduction: 66%				[217]
HRDSR	AZ61	17.4 μm (rolled alloy) to 1.09 μm	Dec.	0.81	0.50 (speed ratio of 3)	P_w	S3, T1		- HRDSR • Speed ratio: 2 or 3 • T: 150 ˚C • Thickness reduction: 66% or 67% • - Pass No: 2				[53]
Rotary swaging	WE43	61.3 μm (cast alloy) to 0.66 μm	Dec.	1.82	1.52	P_H	S9, 2T1	24	- Homogenization: 8 h, 525°C - Extrusion • Ratio: 6.55 - Rotary swaging • Maximum force: 8 kN • Frequency: 1920 impacts per minute • - T: 400-325°C	336	220	15.2	[69]

(*continued on next page*)

Table 1 (*continued*)

Type of SPD	Alloy	Grain Refine. (μm)	CR Trend by SPD	CR before SPD	Lowest CR after SPD	Method	Solution	Duration (h)	SPD condition	Best mechanical properties			Refs.
										UTS	YS	El	
FSP	AZ31	16.4 μm (annealed alloy) to 3.2 μm	Inc.	3.99	4.63	P_w	S9, T2		- Annealing: 340°C, 1 h - FSP • FSP tool: H13 tool steel • Travel speed: 100 mm/min • Rotational speed: 1100 rpm • - Penetration depth: 3 mm				[218]
FSP	ZK60	68.2 μm (aged alloy) to 3.1 μm (P#1)	Dec. and Inc.	12.53	5.01	P_H	S1, T1	120	- Aging: 448 K, 10 h - FSP • Passes No: 3 • Rotation speed: 1000 rpm • - Traveling speed: 90 mm/min				[163]
FSP	WE43	53 μm (cast alloy) to 2.7 μm	Dec.	38.41	15.12	P_w	S4, T1	6 days	- Rotation rate: 600 rpm • Traveling speed: 60 mm.min^{-1} - Passes No: 1				[220]
Shot peening	AZ31	53 μm (rolled and annealed alloy) to 2 μm	Inc.	0.48	7.33 (Repinned Severe Shot Peened)	P_i	S9, T1	As-immersed	- Shot Particles: Ceramic beads composed of zirconium oxide, silica and alumina with a nominal size of 0.1-0.15 mm and a hardness of 640-780 HV - Re-peened Particles: AGB6 are soda-lime glass beads with a nominal size and hardness ranging between 0.043–0.089 mm and 500–550 HV - Almen intensity (mm): 0.15, 0.4, 0.4 N - Surface coverage: 100, 1000, 1000 %				[210]

Table 1 (*continued*)

Type of SPD	Alloy	Grain Refine. (μm)	CR Trend by SPD	CR before SPD	Lowest CR after SPD	Method	Solution	Duration (h)	SPD condition	Best mechanical properties			Refs.
										UTS	YS	El	
Screw rolling	ZAXM4211	2.8 μm (extruded alloy) to 2 μm (T=180˚C)	Dec. and Inc.	5.94	1.38 (SR300)	P_H	S8, T1	7 days	- Homogenization: 340 ˚C, 12 h - Extrusion • T: 260 °C • Ram speed: 5 mm/s • Ratio: 10:1 - Screw rolling • - T: 220, 260, 300, 340 ˚C - diameter: 280 mm	327.4 (SR220) 317.1 (SR300)	308.6 (SR220) 272.2 (SR300)	8.3 (SR220) 8.3 (SR300)	[60]
Shot peening	AZ31	32.5 μm (rolled alloy) to 0.1 μm	Dec.	0.31	0.18	P_w	S1, T1	30	- Rotating speed of impeller: 2520 r/min- Peening balls: zirconia (400 mm in diameter)- Time: 1 h- T: room				[209]
Ext	AZ80	84.1 (Cast) to 4.6	Inc	10 (mpy)	300 (mpy)	P_w	S1,T1	72	Initial diameter: 70 mm Extruded diameter: 10.5 mm - Extrusion • T: 250 ˚C • Speed: 0.12 mm/min • Time: 1 h				[90]
Ext	Mg-xCa (x=0,0.4,1,2,3)	739.23 (Cast) to 6.02	Inc.	0.16	0.18	P_i	S2,T2	As-immersed	- Homogenization • T: 370 °C • T: 8 h - Indirect Extrusion • Ratio: 19.6 • T: 350 ˚C • Ram speed: 72 mm/min - Anneal • T: 250 ˚C • t: 3 min	234.1 (Extruded X0)	165.6 (Extruded X0)	34 (Extruded X0)	[117]
Ext	AZ91	3-5 (Extruded)	Inc.	1.01	1.66	P_w	S8,T1	12	- Extrusion • Ratio: 18:1 • T: 240 ˚C • Rate: 2-3 m/min				[223]

22

Table 1 (continued)

Type of SPD	Alloy	Grain Refine. (µm)	CR Trend by SPD	CR before SPD	Lowest CR after SPD	Method	Solution	Duration (h)	SPD condition	Best mechanical properties			Refs.
										UTS	YS	El	
cyclic extrusion and compression	3.0Nd-0.2Zn-0.4Zr	50 (Extruded) to 1 (CEC)	Dec.	1.6	1.25	P_w	S2,T2	120	- Solution treatment: • T: 540 ˚C • t: 10 h - Extrusion: • T: 350 ˚C • Ratio: 8 • Ram speed: 2 mm/s - CEC: • Pass Num: 8 • T: 350 ˚C • Ram speed: 2 mm/s	300	250	30	[224]
Ext	AZ61+xCa	15.8 (Extruded AZ61) to 15.9 (Extruded AZX610)	Inc.	0.71	1.76	P_w	S1,T1	72	- Homogenization: • T: 400 ˚C • t: 24 h - Extrusion: • T: 300 ˚C • Ratio: 30 • Ram speed: 1 m/min				[274]
Ext	ZX10+xAg	9.8 (Extruded ZX10) to 7.35 (Extruded ZX10 with 1 Ag)	Dec.	3.95	3.17	P_w	S4,T2	168	- Homogenization: • T: 450 ˚C • t: 24 h - Extrusion: • T: 350 ˚C • Ratio: 28	224 (ZX-1Ag)	132 (ZX-1Ag)	28 (ZX-1Ag)	[246]
Ext	AZXW6110	17-18	Dec.	1.84 (AZX611)	0.31 (AZXW6110)	P_w	S1,T1	72	- Homogenization: • T: 400 ˚C • t: 24 h - Extrusion: • T: 300 ˚C • Ratio: 30 • Ram speed: 1 m/min				[275]

Table 1 (*continued*)

Type of SPD	Alloy	Grain Refine. (μm)	CR Trend by SPD	CR before SPD	Lowest CR after SPD	Method	Solution	Duration (h)	SPD condition	Best mechanical properties			Refs.
										UTS	YS	El	
Ext	3.0Nd-0.2Zn-0.4Zr	45 (T4 sample) to 5 (Extruded)	Dec.	0.35	0.23	P_H	S4,T2	240	- Solution treatment: 540 ˚C, 10 h - Extrusion • T: 250 ˚C • Ratio: 25	234 (Ext.)	162 (Ext.)	26 (Ext.)	[248]
Ext	3.0Nd-0.2Zn-0.4Zr	45 (T4 sample) to 2 (Extruded)	Dec.	0.35	0.11	P_H	S4,T2	240	- Solution treatment: 540 ˚C, 10 h - Extrusion • T: 32 ˚C • Ratio: 8	312 (Ext.)	308 (Ext.)	12.2 (Ext.)	[249]
Ext	ZAX422		Inc.	1.74 (ZA42)	12.22 (ZAX422)	P_w	S8,T1	168	- Homogenization: 340 ˚C, 12 h - Extrusion • T: 260 ˚C • Ram speed: 5 mm/s • Ratio: 10:1	365.4 (Extruded ZAX422)	341.7 (Extruded ZAX422)	23.6 (Extruded ZA42)	[241]
Rolling	AZ31	21 (Extruded) to 14 (Rolled)	Dec.	29	18	P_w	S1,T1	45	- Rolling • Rolling speed: 0.2 m/s • Pass No: 2 - Anneal • T: 300 ˚C • t: 1 h				[276]
Rolling	LA51	94.3 (0% Rolled) to 83.4 (20% Rolled)	Dec.	40.32	10.5	P_w	S1,T1	336	- Extrusion • T: 380 ˚C - Rolling • T: room • Reduction: 20%				[277]

>S1= 3.5% NaCl, S2= Hank's, S3= 0.1 M NaCl, S4=SBF, S5=PBS, S6= RPMI-a 1640 Medium, S7=Ringer, S8= 3.5% NaCl+ Mg(OH)$_2$, S9= 0.9% NaCl

>T1= 25 ˚C, T2= 37 ˚C, P: pass number, P_W: corrosion rate by weight loss, P_H: corrosion rate by hydrogen evolution and P_i: corrosion rate by electrochemical polarization method.
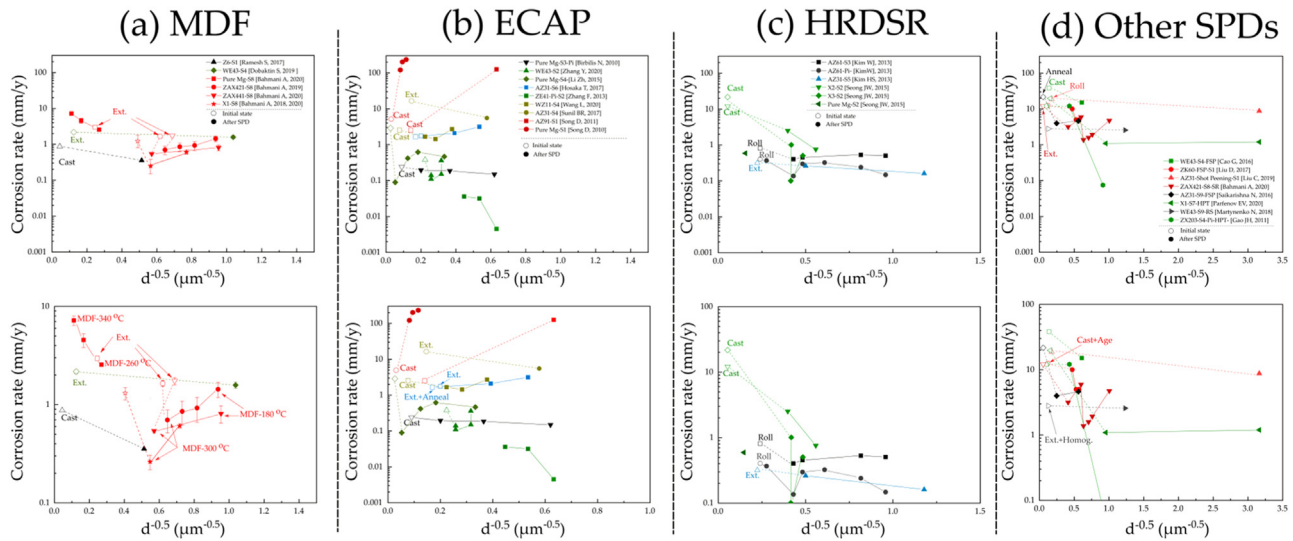
Fig. 19. Corrosion rates of magnesium alloys subjected to SPD processes: (a) MDF, (b) ECAP, (c) HRDSR and (d) other SPD processes. The plots are constructed using the raw data from the references of [50,53,57,60,85,94–96,103,108,148,157,163,185,209,211,213–220]. The types of solution media used for the corrosion tests are stated in Table 3. The plots at the bottom show the enlarged area (where the data points are clustered) in the plots at the top.

refinement. The corrosion rates of the extruded X1, ZAX421 and ZAX441 alloys also decreased after MDF [56,57,108]. However, a decrease in the corrosion rate with an increase in the MDF temperature below 300°C despite a less effective grain refinement at a higher MDF temperature is noted. This may be related to a higher dissolution of the secondary phase into the matrix at a higher processing temperature due to the increased solute solubility.

4.2. Corrosion rates of ECAP processed Mg alloys

The corrosion rates of pure Mg and Mg alloys subjected to the ECAP process are drawn as a function of the grain size in Fig. 19 (b). Corrosion rates in 0.1 M (0.6 wt. % NaCl) and Hank's solution (S2 and S3) are lower than those measured in other solutions, but a general trend of decreasing the corrosion rate with the grain refinement is observed. Both positive and negative slopes of the corrosion rate relative to the grain size are, however, observed in pure Mg without secondary phases. Song et al. [95] reported acceleration of the corrosion rate in pure Mg after ECAP, while Birbilis et al. [103] and other researchers [94,101,104] reported a decrease in the corrosion rate after ECAP in some cases [102]. The main differences in the processing conditions used by these researchers are the grain size range and the solution media type, as discussed in Fig. 3. Bahmani et al. [94] used 3.5 wt. % NaCl with a high amount of Cl⁻ ions, and op't Hoog et al. [104] used a 0.6 wt. % (0.1 M) NaCl solution, which is considered to be a low aggressive solution. According to Golappudi's study [106], aggressive solutions have a low capability of passivation because aggressive ions such as Cl⁻ attack the $Mg(OH)_2$ layer, which initially forms on the surface of Mg. The corrosion rates of Mg alloys such as ZE41 and AZ31 immersed in Hank's and SBF generally tend to decrease as the grain size decreases. For an AZ91 alloy with a

large amount of secondary phase, however, the corrosion rate increases when the cast microstructure is refined. This may be because the negative effect of breakage of the secondary phases on corrosion resistance is more pronounced than the positive effect of grain refinement.

4.3. Corrosion rates of Mg alloys processed by HRDSR or other SPD methods

The trend of corrosion-rate reduction by grain-size reduction has been observed from the majority of the alloys processed by HRDSR or other SPD processes (Fig. 19 (c) and (d)). In the case of HRDSR materials, the corrosion rate of Mg alloys decreased after processing in various solution media. This behavior has also been reported in the case of pure Ti for HRDSR [212]. The trend of decreasing the corrosion rate with a decreasing grain size is noted for the various alloys in the other SPD methods. However, the corrosion rate of the samples processed by SShP [209] and HPT [167] with nanoscale microstructures did not effectively decrease. This may be due to the accumulation of a high density of dislocations in non-equilibrium grain boundaries characterized by excess grain boundary energy and presence of long range elastic stresses during very heavy deformation at low temperatures. The corrosion properties of a ZAX421 alloy after extrusion and subsequent SR [60] show that the corrosion rate effectively decreased after SR, but the processing temperature affected the corrosion rate. The corrosion rate decreased by increasing the SR processing temperature from 220 to 300°C due to dissolution of the secondary phase, but increasing the temperature from 300 to 340°C resulted in an increase in the corrosion rate due to the enhanced grain growth. This trend has also been observed for X1 [56] and ZAX421[57] alloys processed by MDF (Fig. 19 (a)).

As reviewed above, for the majority of cases the corrosion rate reduction occurs after SPD due to grain refinement regardless of difference in SPD technique. The minimum grain sizes obtained by ECAP, MDF (and HRDSR, SR and FPS), HPT (and shot peening) used for corrosion studies of pure Mg and its alloys are near 0.1 μm, 1 μm and 2.5 μm, respectively. The SPD-processed Mg and its alloys show typical corrosion rates of 0.1 - 1 mm/year at grain sizes less than ∼ 4 μm. Grain refinement less than 1 μm appears to be not so effective in further improvement of corrosion resistance. When grain size is in the large range (where the degree of grain refinement via SPD is small), the positive effect of grain refinement on corrosion rate appears to be less distinct. This is because the negative effect on corrosion such as dislocation-density increase and break up a net-like shape secondary phase exceeds the positive effect of grain reduction that is small at large grain sizes. The Mg alloys processed under the SPD conditions and post-SPD heat treatments where grain refinement effectively occurred with minimizing the increase of dislocation density and secondary phase was broken finely and uniformly precipitated or dispersed over the matrix commonly exhibited the low corrosion rates.

4.4. Corrosion rates of various composition Mg alloys processed by SPD

The corrosion behavior of pure Mg and several commercial Mg alloys that have been subjected to various SPD processes has been drawn as a function of grain size for a given composition in Figs. 3 and 20 (a)–(c). For pure Mg, the corrosion rate tends to decrease as a result of the grain refinement in the small grain size range, as already discussed in Fig. 3. Li et al. [102] obtained a complicated trend of the corrosion rate relative to the grain size. They ran ECAP on pure Mg at different temperatures, including 200, 250, 300 and 360°C, for 4 passes. The corrosion rate of the pure Mg decreased after ECAP for all deformation temperatures compared to that of the cast Mg. Among the ECAPed materials, the lowest corrosion rate was obtained from the pure Mg ECAPed at 360°C, and the highest rate was obtained at 250°C. For pure Mg processed by MDF [94] where the dislocation density was low at all grain sizes due to the occurrence of full dynamic recrystallization in the investigated temperature range, however, increasing the processing temperature increased the corrosion rate. This is because the obtained grain size was larger at the larger processing temperature. The same trend of corrosion-rate reduction by grain-size reduction has been reported for other metals, such as pure Al [100,226], Fe [227] and Ti [228]. Corrosion-rate reduction by grain refinement is a general trend in the SPD AZ31, AZ61 and WE43 alloys, despite the difference in the SPD methods (Fig. 20 (a) and (b)). In the case of the AZ31 alloy ECAPed at a low temperature (ECAP-150°C), the corrosion rate during 24 h of immersion in an RPMI solution media increased compared to that of the as-received alloy due to the presence of high-density dislocations in the ECAPed state. The AZ31 alloy ECAPed at a higher temperature (ECAP-300°C) shows a lower corrosion
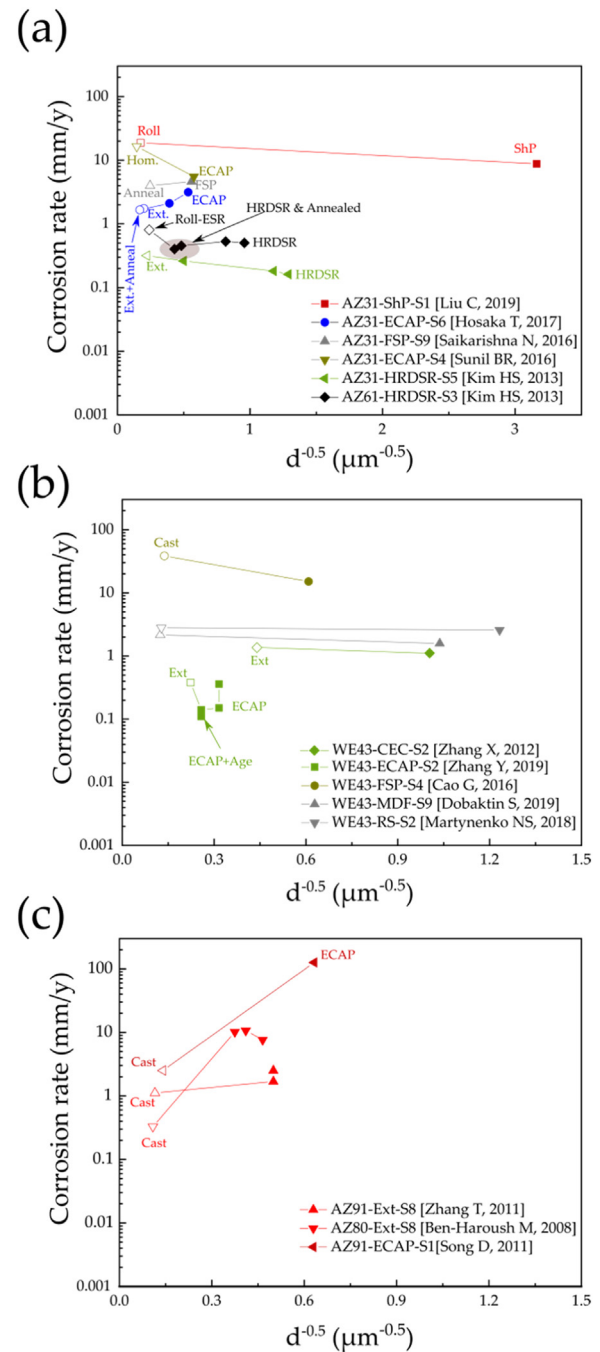

Fig. 20. Corrosion rates of commercial Mg alloys subjected to SPD: (a) AZ31 and AZ61 alloys, (b) WE43 and (c) AZ80 and AZ91 alloys. The plots are constructed using the raw data from the references of [53,69,85,90,94–96,102,103,185,213–215,217,218,220–225]. The types of solution media used for the corrosion tests are stated in Table 1.

rate than the ECAP-150°C alloy due to the high annealing temperature effect that reduces the lattice strain and dislocation density more effectively. Their observation that the corrosion rates of the as-received extruded AZ31 alloy decreased after annealing at 420°C also supports the negative effect of high dislocation density on corrosion [215]. For the AZ91 and AZ80 alloys, which have higher amounts of alloying elements and secondary phases, the trend is the opposite (Fig. 20 (c));

A. Bahmani, M. Lotfpour, M. Taghizadeh et al. *Journal of Magnesium and Alloys xxx (xxxx) xxx*

that is, the corrosion rate increased after SPD, despite grain refinement. This is most likely due to alteration of the secondary phase morphology from a net-like shape in the cast state to isolated shapes after plastic deformation. The trend of all results with the processing and testing conditions is given in Table 1.

Another point that can be observed in Figs. 3 and 20 is the effect of the solution media on the corrosion rate value. For instance, pure Mg immersed in a solution with a lower concentration of NaCl (S3 solution with 0.6 wt. % NaCl) [103,104] has lower corrosion rates in the same grain size range compared with those in the higher NaCl-containing solutions [94,101] (the S1 and S8 solutions with 3.5 wt. % NaCl)). The corrosion rates of the AZ31 and AZ61 alloys immersed in 0.9 [218] and 0.6 [53] wt. % NaCl solution are also lower than those of the AZ31 alloy in the 3.5 [163] wt. % NaCl solution media. Fig. 20 (c) shows that the corrosion rates of the AZ91 and AZ80 alloys in 3.5 wt. % NaCl saturated with $Mg(OH)_2$ (S8) are lower than that of the AZ91 alloy immersed in a 3.5 wt. % NaCl solution (S1), suggesting that the addition of $Mg(OH)_2$ to the solution media decreases the rate of Mg degradation.

5. Relationship between mechanical and corrosion properties of SPD-processed Mg alloys

When designing an industrial component, the material properties are the most important parameters that need to be considered; mechanical properties such as tensile and compressive strength, ductility and formability are the key factors. In this section, the mechanical and corrosion properties of SPDed Mg materials are compared with those of cast Mg and Mg alloys, and the results are discussed. Since different researchers have used various solution media for corrosion studies, graphs were drawn for each medium separately.

Fig. 21 shows the mechanical properties of Mg alloys relative to the corrosion rate in various solution media after different SPD processing routes. In the first row (Fig. 21 (a$_1$–a$_3$)), the plots for the cases when the 3.5 wt. % NaCl or 3.5 wt. % NaCl saturated with $Mg(OH)_2$ were used as the solution media are shown. These solution media are aggressive due to the presence of a high concentration of Cl$^-$ ions [229–232]. The yield strength (YS) and ultimate tensile strength (UTS) of several Mg alloys were enhanced after the SPD processes. The tensile ductility was also improved after SPD (it was especially pronounced when MDF was used). In the case of SR, however, elongation decreased due to the effect of a strengthened basal texture. Fig. 21 (b) and (c) show Mg alloys immersed in *in vitro* media, such as Hanks' solution (Fig. 21 (b)) and simulated body fluid (SBF, also called Kokubo's solution [233,234]) (Fig. 21 (c)). Mg alloys processed by various deformation methods, such as ECAP, FSP and HRDSR, have higher YS and UTS values than their cast or extruded (rolled) counterparts due to microstructural refinement and removal of casting defects, such as voids and solute segregation [235,236]. Grain refinement after SPD enhances the yield strength through the Hall-Petch relation [237]. In

the majority of the studied cases, corrosion (degradation) rate reduction was also observed after SPD. Running HRDSR on the pure Mg, X1 and X04 alloys resulted in enhancement of both the YS and UTS. Due to the large increase in the dislocation density after SPD, corrosion rates in Hank's solution were increased (Fig. 21 (b)), but annealing at 350°C after HRDSR reduced the corrosion rate and improved the tensile elongation significantly, while it reduced the YS [238]. Zhang et al. [214] reported that ECAP at 250°C enhanced the mechanical properties and corrosion behavior of a WE43 alloy immersed in Hank's solution (Fig. 21 (b)). After 2 passes of ECAP, a high strength of 330 MPa (UTS) and 295 MPa (YS) and a low corrosion rate of 0.15 mm/y after 2 weeks were obtained. A high strength and a low corrosion rate were also simultaneously obtained from the X1 Mg alloy processed by MDF. Improvement in the strength and elongation along with a reduction in the corrosion rate in SBF can also be observed from the pure Mg and the ZK60 alloy processed by ECAP and the WE43 alloy processed FSP (Fig. 21 (c)). Fig. 21 demonstrates the promising abilities of SPD processes in simultaneously improving both the mechanical and corrosion properties of Mg alloys).

6. Corrosion behavior of the SPD-processed Mg alloys

6.1. Case studies on the corrosion behavior of Mg alloys processed by SPD

Several researchers have studied the corrosion behavior of magnesium after plastic deformation. As the main approach of the current article is reviewing and assessing the corrosion behavior of Mg alloys processed by severe plastic deformation, here we first discuss the corrosion mechanism change after conventional plastic deformation, such as normal extrusion and rolling, and then the corrosion mechanism alteration after severe plastic deformation will be discussed. Ben-Haroush et al. [90] extruded an AZ80 alloy at different temperatures, including 250, 300 and 350°C, and found that the corrosion rate increased at all extrusion temperatures. The AZ80 alloy comprises a high content of aluminum, which forms a continuous net-like shape of the β phase in the as-cast microstructure. As previously proven in many studies, the β phase is cathodic relative to the magnesium alpha matrix [112,256,257]. However, the volta-potential difference of this phase relative to the matrix is small, making the β phase a good barrier against corrosion progress in the as-cast microstructure. Deformation by extrusion results in partial fragmentation and alignment of the β phase through the extrusion direction, which not only annihilates the barrier effect of this phase, but also forms a continuously aligned galvanic cell through the depth of the material, which results in a corrosion attack inside the alloy during immersion (Fig. 22).

Unlike the aforementioned case for the AZ80 alloy, Gui et al. reported [255,258] that the corrosion rate of VZKM3300 (Mg-3Gd-3Zn-0.3Zr-0.3Mn) decreased after extrusion. Fig. 23 shows that the decrease in the corrosion rate after extrusion is due to uniform dispersion of fine β phase particles
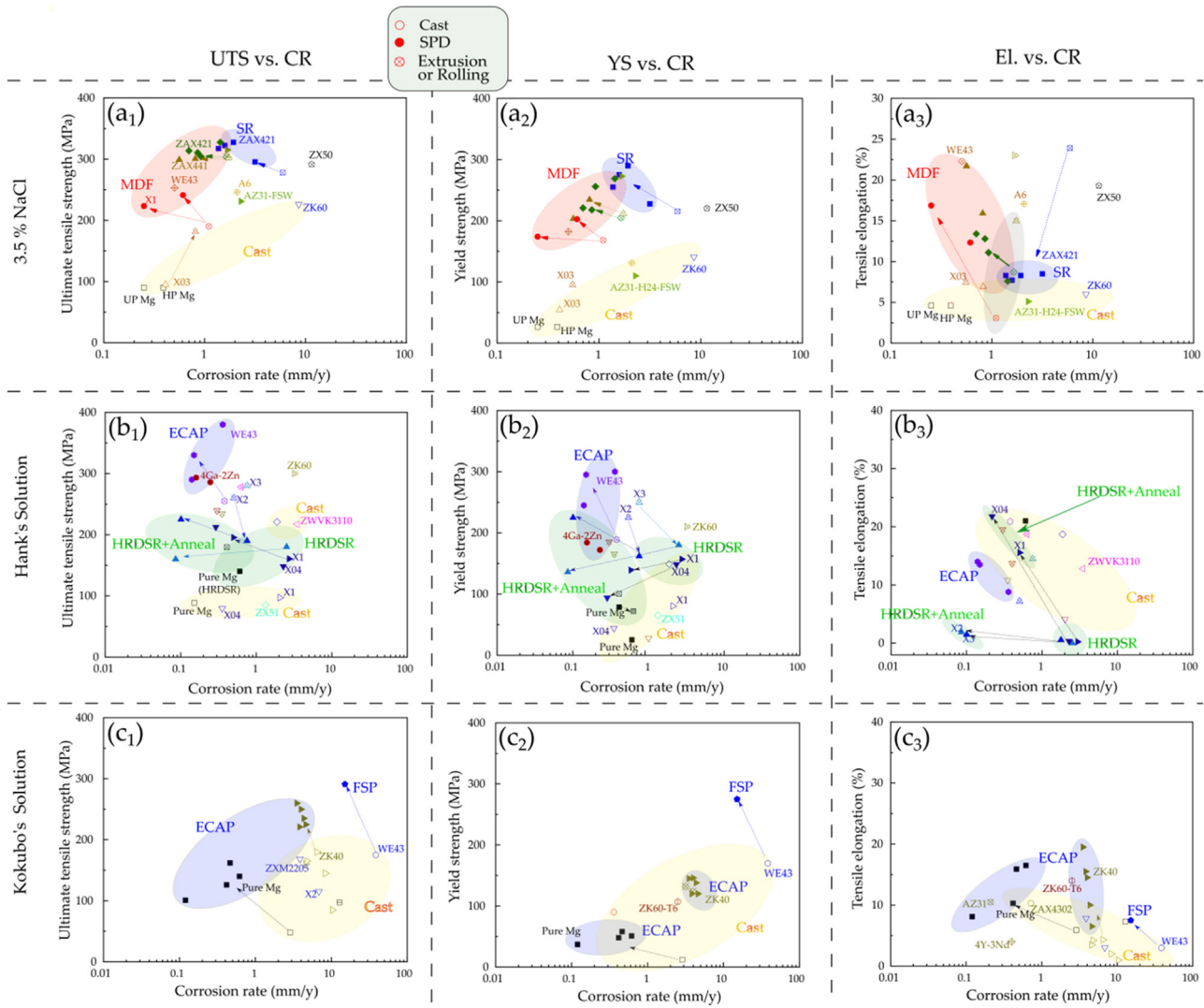
A. Bahmani, M. Lotfpour, M. Taghizadeh et al.

Fig. 21. Mechanical properties of magnesium alloys vs. the corrosion rate in (a1-a3) 3.5 wt. % NaCl or 3.5 wt. % NaCl saturated with Mg(OH)$_2$, (b1-b3) Hank's solution and (c1-c3) Konubo's SBF solution. The plots are constructed using the raw data from the references of [2,60,86,87,94,108,199,221,222,238–255].
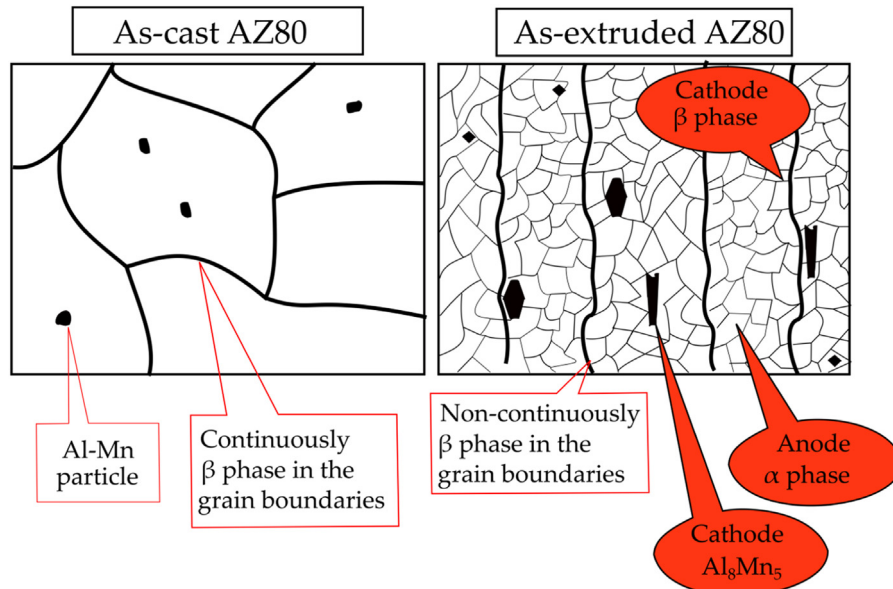

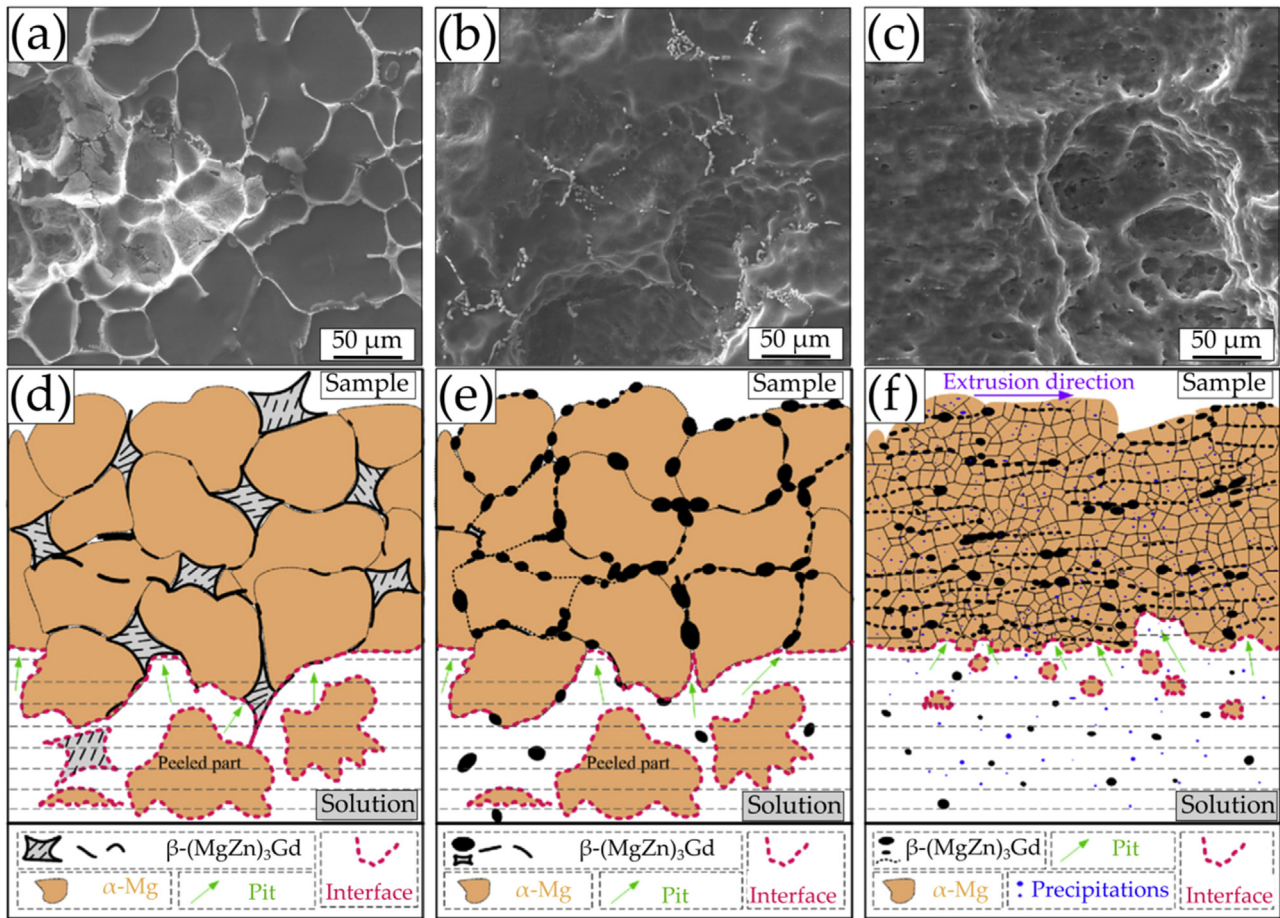Fig. 22. Secondary phase distribution in the cast and extruded AZ80 alloys [90].

Fig. 23. Corrosion morphology of the exposed surface of the VZKM3300 alloy in Hank's solution for 240 h after removal of corrosion products of the (a) as-cast, (b) heat treated and (c) hot extruded samples and a schematic representation of the corrosion mechanism for the (d) as-cast, (e) heat treated and (f) hot extruded samples [255].

on the refined grains, leading to uniform corrosion. When the β phase is not fully continuous or coarsely discontinuous in the cast and heat-treated materials, non-Faraday material loss and localized corrosion can occur, such that the large grains and secondary phases can be peeled off from the substrate due to corrosion of the matrix near secondary phases on grain boundaries, resulting in acceleration of the corrosion damage [122]. These results indicate that when the breakup of a continuous secondary phase is inevitable during plastic working, its effective refinement and uniform distribution are important in enhancing the corrosion resistance of Mg alloys. Jeong and Kim [117] also showed a decrease in the corrosion rate in Mg-Ca alloys after extrusion. As the Mg_2Ca phase acts as an anode in a micro-galvanic circuit between the Mg_2Ca phase and Mg matrix, breakup of the Mg_2Ca phase in the network structure by extrusion is advantageous in enhancing the corrosion resistance of Mg-Ca alloys because if it is continuous, then corrosion easily penetrates inside the material with degradation of the Mg_2Ca phase. For this reason, refinement of the grains and secondary phase by extrusion greatly improved the corrosion performance of Mg-Ca alloys.

The application of SPD to extruded Mg can further improve the corrosion resistance by improving the uniformity of the grain size. Bahmani and Shin [108] studied the corrosion behavior of extruded and MDFed ZAX441 alloys in a 3.5 wt. % NaCl saturated with $Mg(OH)_2$ (Fig. 24). They found that the extruded alloy with a mixture of elongated grains and fine grains corroded more than the MDFed alloys with fine grains. This is because the large grains (i.e. deformed grains), which were elongated through the extrusion direction, had been deeply corroded compared with dynamically recrystallized (DRXed) fine grains in the extruded sample. The MDFed materials with finer and more uniform grain size distributions exhibited less corrosion. This is one of the advantages of the SPD method, which can develop more homogenous and finer grains compared to conventional deformation methods, such as extrusion and rolling. The HRD-SRed Mg-Ca alloys also exhibited noticeably increased corrosion resistance compared to their extruded counterparts due to a more effective refinement of Mg_2Ca phase particles and grains by SPD [185].

Characterization of the corroded surface can provide significant information about the corrosion mechanism. SPD can
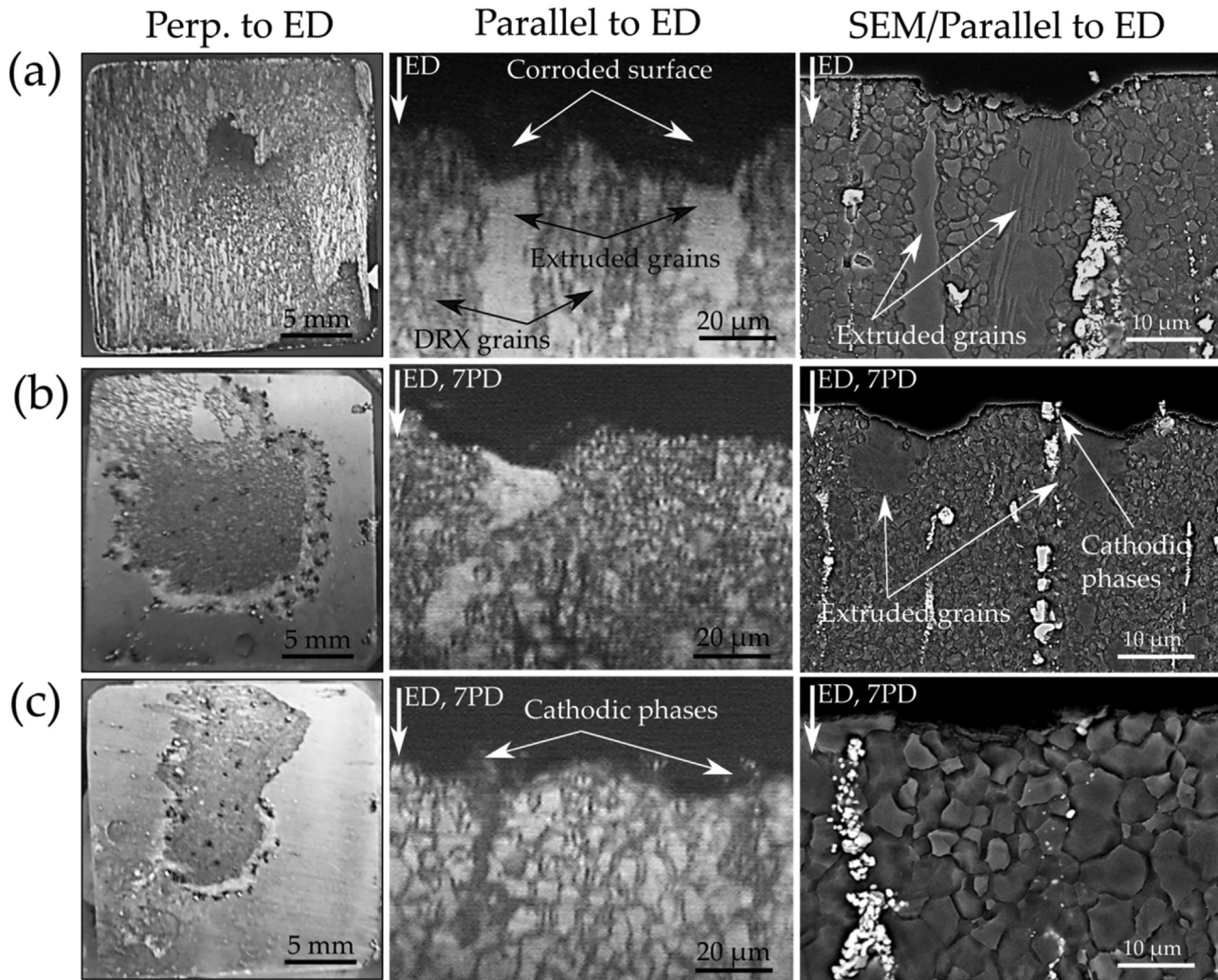
Fig. 24. The surfaces (perpendicular to the extrusion direction [ED]) and the longitudinal cross-section (parallel to the ED) of the ZAX441 alloy after 3 h of immersion: (a) extruded, (b) MDF-180°C, and (c) MDF-300°C [108].

change the initiation and propagation of corrosion attacks on the surface of materials through significant alteration of microstructural features. Depending on the type and conditions of SPD (e.g., temperature, number of passes, roll speed ratio and total accumulated strain), various microstructures can be obtained; hence, various corrosion mechanisms can take place. If the SPD process is run at a low temperature, such that high-density dislocations and lattice defects are created, the material surface will be highly activated (at least at the initial states of immersion) because dislocations and lattice defects act as active anodic zones, facilitating the removal of surface atoms by decreasing the local work function [259–261]. This behavior can be observed for pure Mg (Fig. 25) after the initial state of immersion for 2 min. The number of pits increased as the pass number increased (Fig. 25 (a_1–d_1)), indicating that the surface of this alloy became more activated for corrosion as the material was subjected to more plastic deformation [95]. Immersion for a longer period of time (2 h) (Fig. 25 (a_2–d_2)) also shows that the corroded area increased with the pass number. Due

to the increased immersion time, almost the entire surface of ECAPed pure Mg was corroded. Note that only a small surface portion of the as-cast Mg was corroded during the same immersion period.

The corrosion rate of the AZ91 alloy in 3.5 wt. % NaCl solutions also significantly increased after ECAP compared with that for the cast microstructure [95]. The corroded surfaces of the cast and ECAPed AZ91 alloys are shown in Fig. 26. ECAP processing significantly increased the amount of pitting corrosion and deteriorated the corrosion resistance of the AZ91 alloy. The deterioration of corrosion resistance by ECAP with the pass number might be related to the high generation of internal stress and dislocation density, which provide the preferred sites for corrosion [95]. Moreover, the network-shaped β phase in the as-cast condition, which acts as a barrier against corrosion attack, was broken up during the ECAP process.

Unlike the two cases addressed above, there are many cases where the corrosion progress was slowed upon application of SPD to Mg materials. Gao et al. [50] demonstrated that
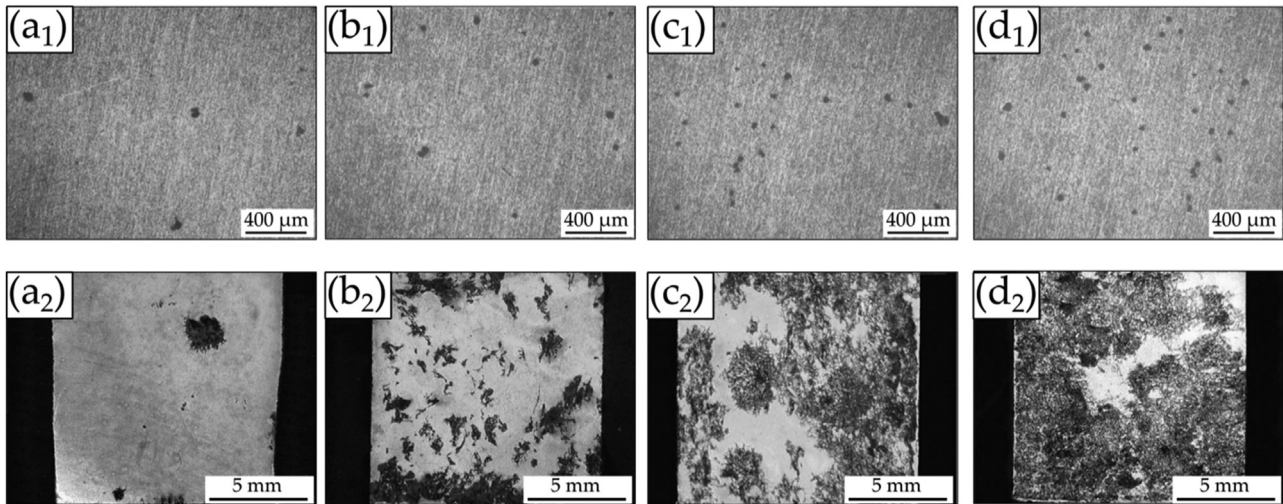
ARTICLE IN PRESS

JID: JMAA [m5+;October 15, 2022;1:50]

A. Bahmani, M. Lotfpour, M. Taghizadeh et al. Journal of Magnesium and Alloys xxx (xxxx) xxx

Fig. 25. Macrographic images of corroded surface pure Mg: (a) as-cast, (b) 1 pass, (c) 4 passes and (d) 6 passes by ECAP at 200°C. The top images are for the 2 min immersed samples, and the bottom images are for the 2 h immersed samples in a 3.5 wt. % NaCl solution [95].
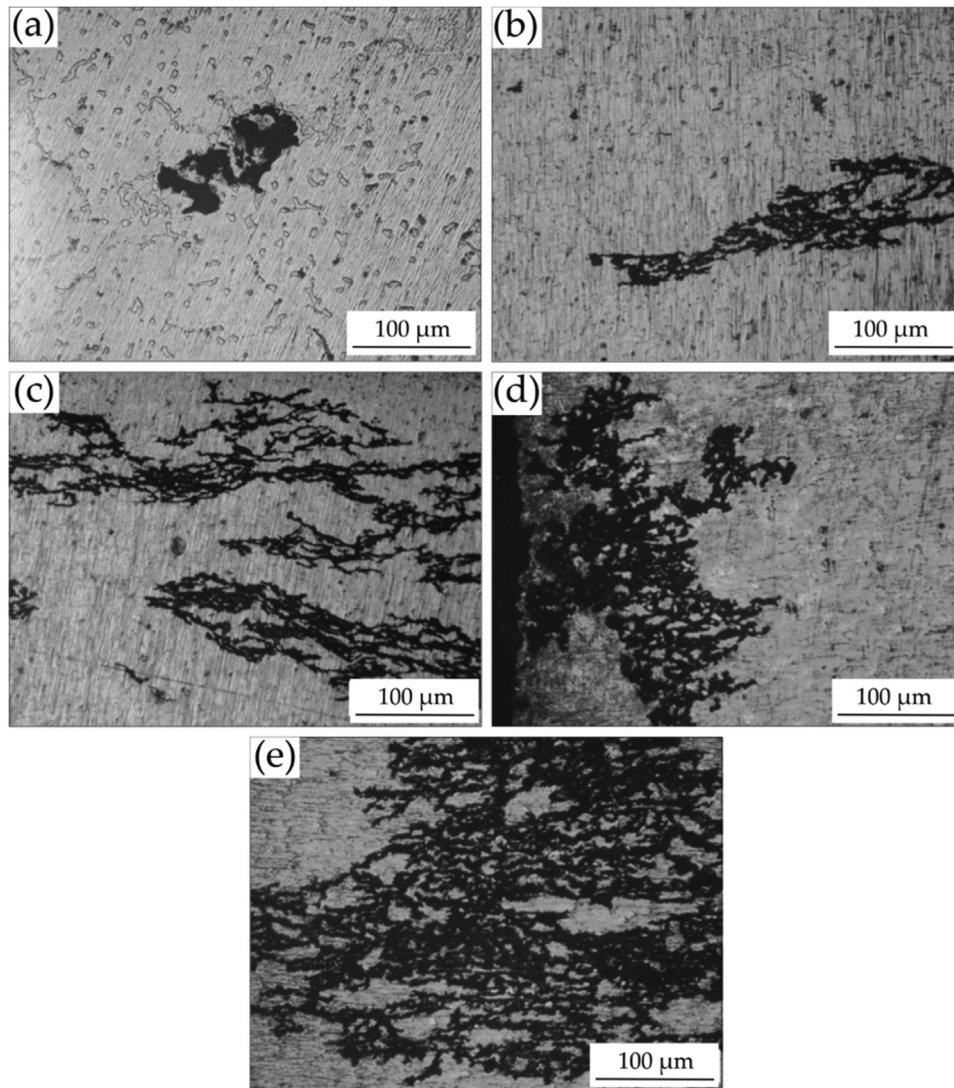

Fig. 26. Corrosion features of the as-cast and ECAPed AZ91D alloy samples after immersion for 10 min in a 3.5 wt. % NaCl solution: (a) as-cast state; (b) 1 pass; (c) 4; (d) 6 and (e) 12 passes [96].
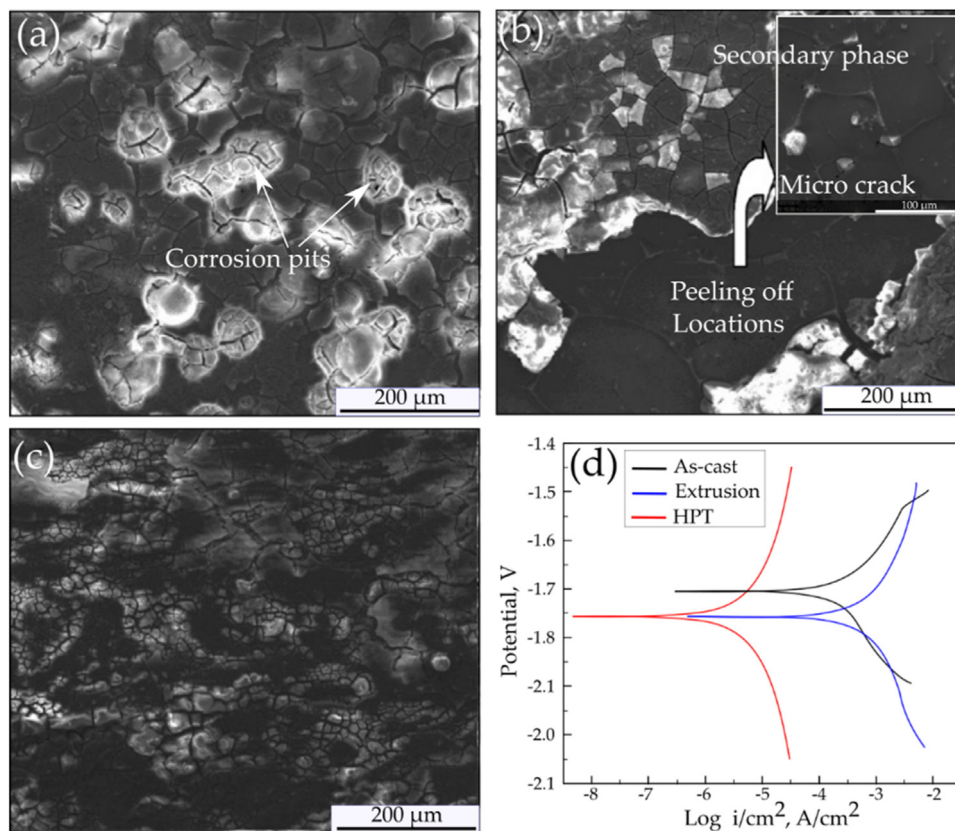
Fig. 27. SEM images of (a) as-cast, (b) conventionally extruded and (c) HPTed Mg-Zn-Ca alloy samples after immersion for 2 days of immersion in Kokubo's SBF solution and (d) a potentiodynamic analysis of the alloys in different processing conditions [50].

the HPT process created more grain boundaries and changed the localized corrosion mode to a more uniform corrosion mode (Fig. 27). They also showed that the formation of numerous lattice defects by HPT accelerates diffusion-controlled recovery during SPD, even at low temperatures, leading to relief of the local stress generated during the HPT process and consequently a more uniform corrosion. The polarization curve also showed that the corrosion current density significantly decreased after HPT, depicting the role of grain boundaries in the formation of a uniform Ca-P layer that increased the corrosion resistance against a severe attack by Cl^- ions.

Naik et al. [262] examined the corroded surface of an AZ80 Mg alloy processed by ECAP after immersion in a 3.5 wt. % NaCl solution and compared the results with those from the as-received sample (Fig. 28). Their study revealed that ECAP changed the corrosion mode from pitting corrosion to more filiform-like corrosion with shallow and randomly distributed pits, which could be attributed to the formation of a uniform passive layer on the surface of the highly refined grains.

Cao et al. [263] investigated the role of heat treatment and the effect of MDF on the corrosion microstructure of the Mg-4Zn-2Gd-0.5Ca alloy (Fig. 29). They found that after heat treatment (solution treatment), the pitting corrosion was significantly reduced due to a decrease in the amount of sec-

ondary phase. However, the MDF (at 350°C with a pressing rate of 2.4 KN/s) slightly enhanced the pitting corrosion, but the degree of pitting and the corrosion rates of the MDFed alloys were much lower than those of the as-cast counterpart. The corrosion rate increased with the pass number, although the fraction of un-DRXed grains continued to decrease by increasing the MDF pass number. This may be related to precipitation of more secondary phase particles from the solute supersaturated matrix with an increasing pass number, which causes more severe micro-galvanic corrosion.

Choi and Kim [264] reported that annealing at 250°C after HRDSR effectively decreased the corrosion rate when a uniform grain size distribution was obtained after annealing, but when a bimodal grain size distribution developed during annealing, the corrosion rate increased. The corroded surface of HRDSRed ZK60 with a bimodal grain-size distribution immersed in Hank's solution for 1 h and 2 h is shown in Fig. 30. Corrosion occurred heterogeneously and was preferentially initiated in regions where fine grains were agglomerated (Fig. 30 (a) and (b)). After an immersion time of 2 h (Fig. 30 (c) and (d)), deeper pits developed in the fine-grained regions, many of which were connected to form channels. This result was attributed to accelerated corrosion by forming a galvanic corrosion couple between the fine-grained and coarse-grained regions. Zeng et al. [265] studied the corrosion behavior of an extruded ZK60 alloy bar that has coarse
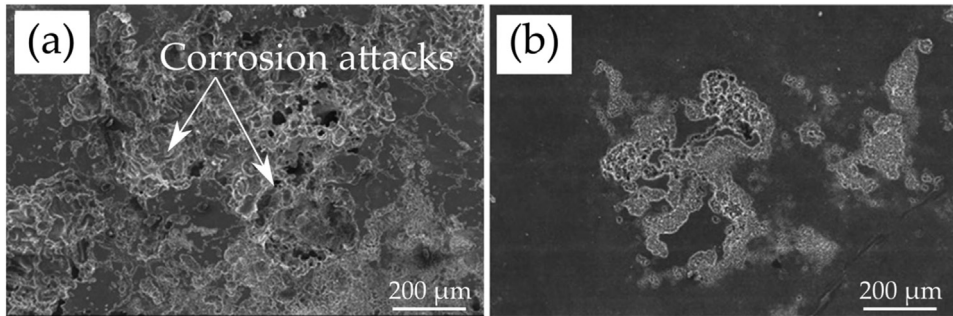
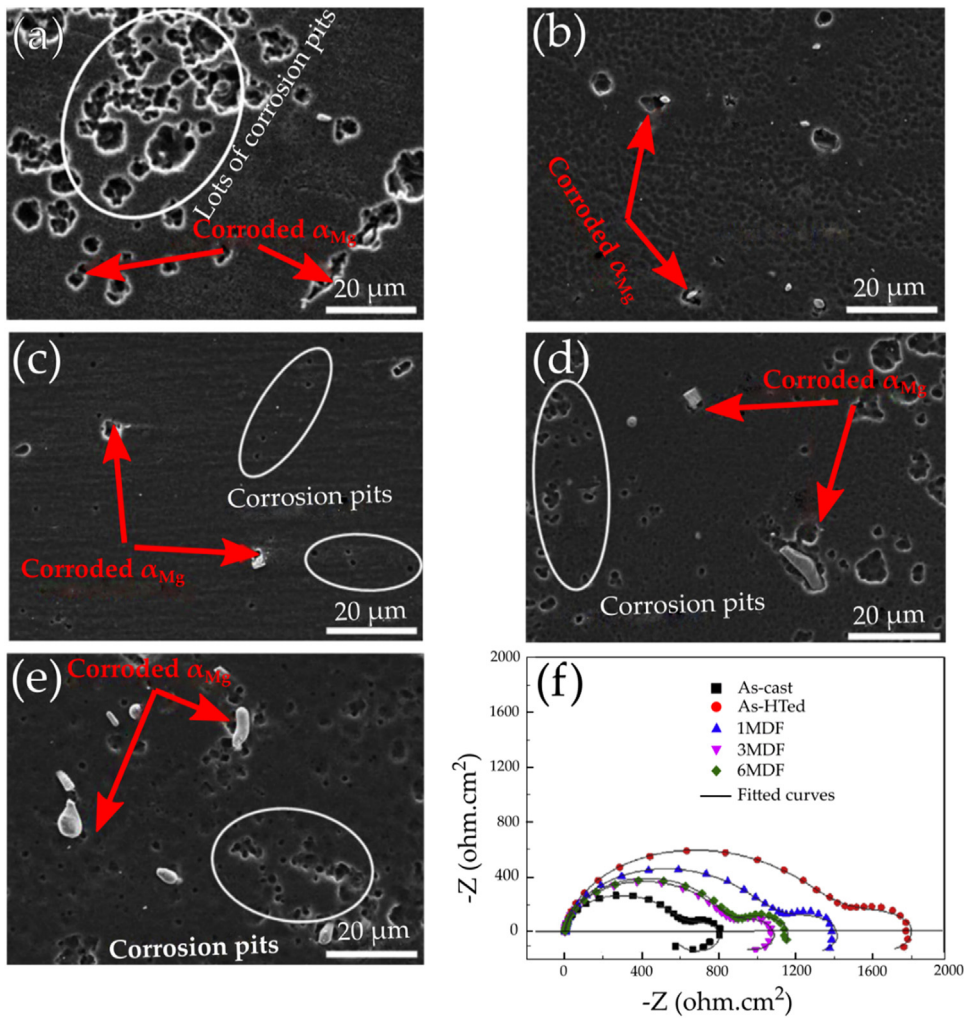Fig. 28. Corrosion morphology of the AZ80 Mg alloy: (a) as-received, (b) ECAPed [266].

Fig. 29. SEM micrographs of the corroded surfaces of the Mg-4Zn-2Gd-0.5Ca alloy immersed in 3.5 wt.% NaCl for 30 min: (a) cast and (b) as-heat treated, (c) MDF-1 pass, (d) MDF-3 passes, (e) MDF-6 passes and (f) Nyquist plot curves of the samples after 40 min of immersion [263].

grains on the outer skin and fine grains in the interiors, and they also observed the occurrence of preferential corrosion on the fine grains near the skin. These results indicate the importance of a uniform grain size distribution in addition to grain refinement in enhancing the corrosion properties of Mg alloys. Saikrishna et al. [218] studied the influence of bimodal grain size distribution on the corrosion behavior of a friction stir processed biodegradable AZ31 alloy in a 0.9% NaCl solution and found that the formation of the bimodal grain size distribution deteriorated the corrosion resistance.

The surface morphologies of the annealed HRDSRed pure Mg, Mg-0.4Ca (X04), and Mg-1Ca (X1) after immersion in Hank's solution (at three magnifications) are shown in Fig. 31. It can be seen that large and deep-scale pits formed in
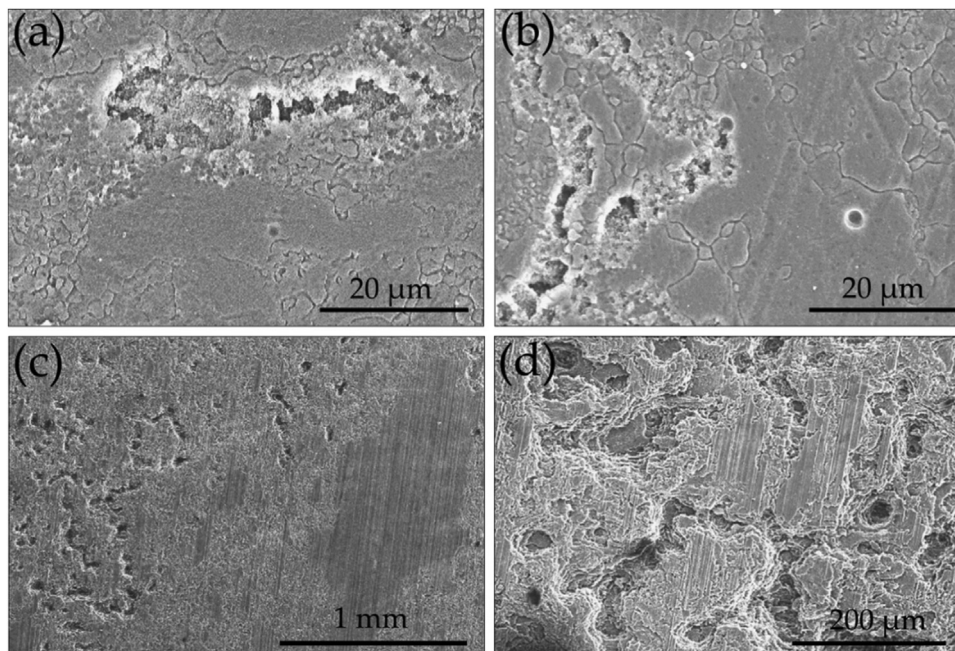
Fig. 30. Corroded surface of the HRDSRed ZK60 alloy and annealed at 250°C for 6 h observed after immersion for (a)(b) 2 h and (c)(d) 6 h [264].
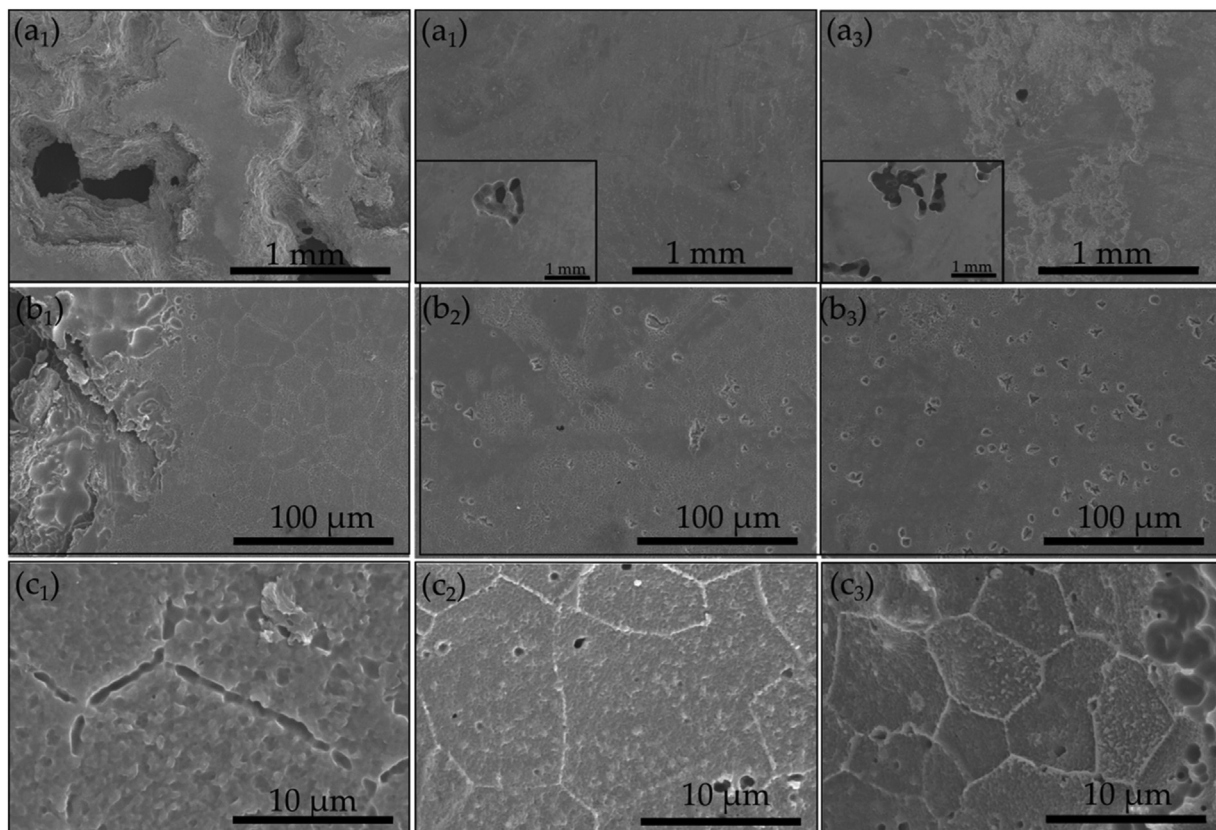

Fig. 31. The surface morphologies of the HRDSRed (a_1–a_3) pure Mg, (b_1–b_3) Mg-0.4Ca and (c_1–c_3) Mg-1.0Ca alloys annealed at 350°C for 30 min after 7 days of immersion in Hank's solution at 37±1°C (after removal of the corrosion products) [238].

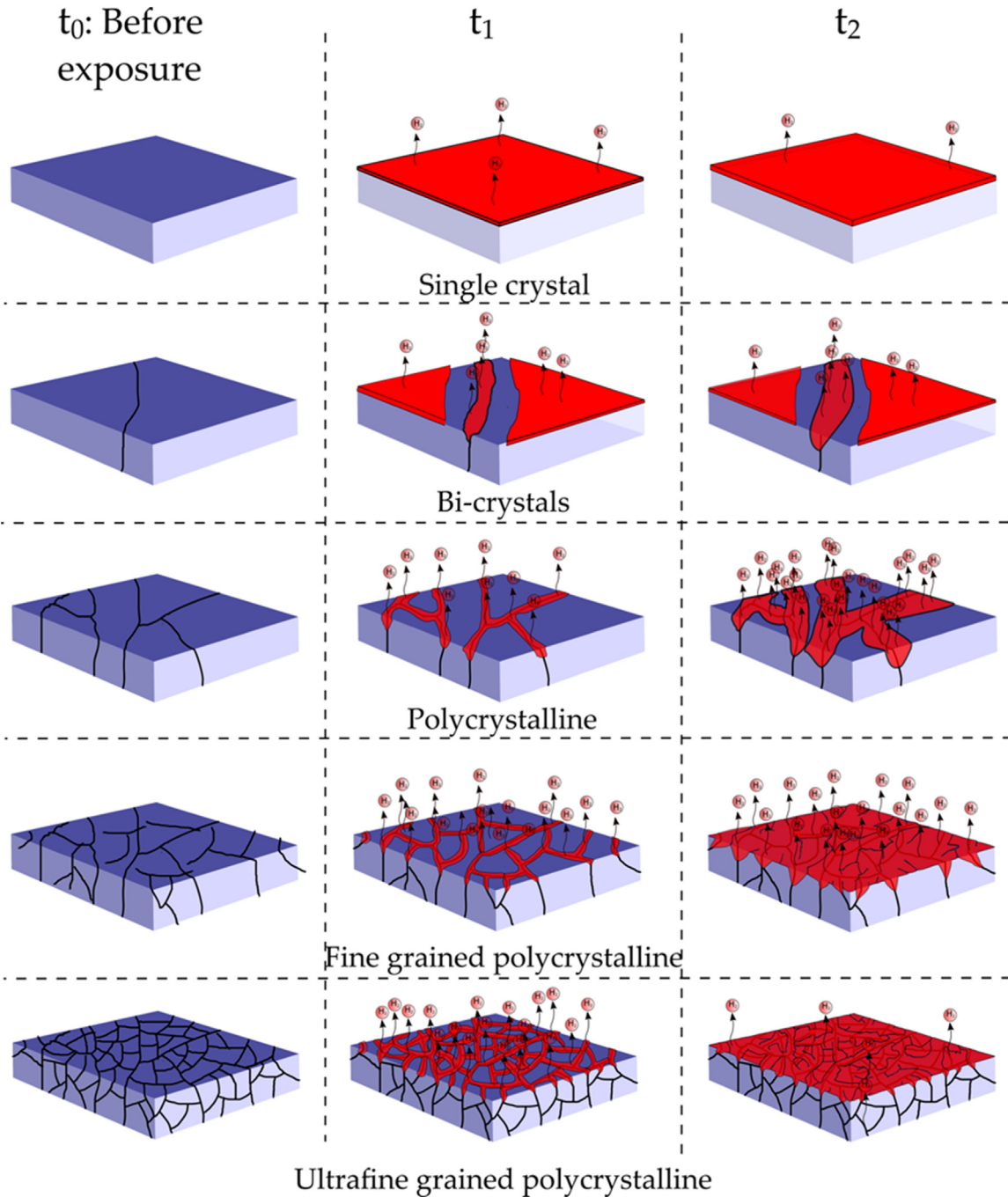A. Bahmani, M. Lotfpour, M. Taghizadeh et al.

Fig. 32. Schematic representation of the effect of grain refinement on the corrosion resistance [94].

the annealed HRDSRed pure Mg with a large grain size. The size and number of pits in the surfaces of the annealed HRDSRed Mg-0.4Ca (X04) and Mg-1Ca (X1) with small grain sizes (7–8 µm) and uniform grain size distributions were considerably smaller than those of the pure Mg. In the case of pure Mg, grain boundary corrosion took place by forming corroded channels along grain boundaries. However, in the annealed HRDSRed Mg-Ca alloys uniform corrosion occurred despite having lots of Mg$_2$Ca phase particles. This result indicates that effective grain refinement can improve the corrosion resistance of Mg alloys, even in the presence

of a secondary phase, if the particles are finely broken and uniformly dispersed in the matrix.

6.2. Corrosion mechanisms of Mg alloys processed by SPD

Based upon the reviewed corrosion behaviors of pure Mg and Mg alloys, the corrosion mechanisms of the SPD processed Mg and Mg alloys are discussed here. Fig. 32 schematically compares the corrosion progress in single-crystal, bicrystal and polycrystalline pure Mg. The corrosion rate from the beginning is expected to be uniform in single crystal Mg
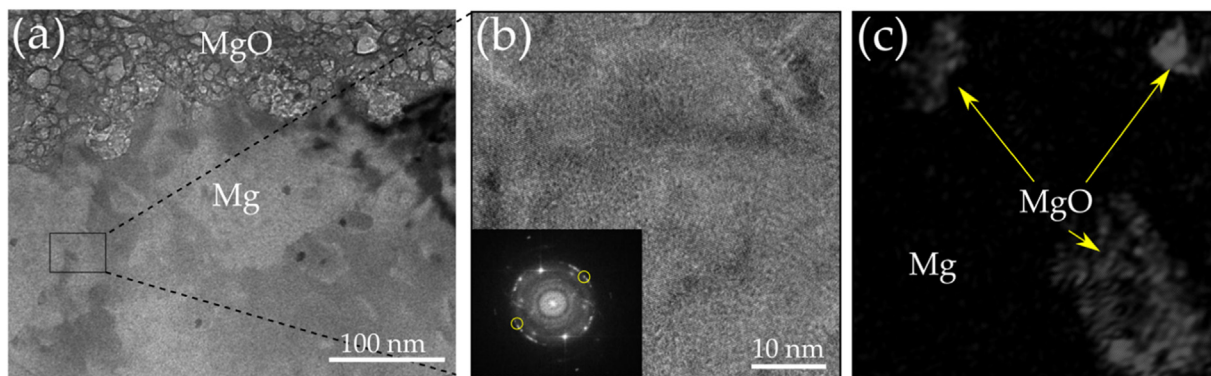
Fig. 33. (a) A TEM image taken around the surface region of HRDSRed AZ61. (b) High-resolution TEM image of HRDSR 3SP taken in the Mg substrate under the MgO layer (boxed area in (a)). (c) The inverse fast Fourier transform (IFFT) of the image in (b) using the selected spots in the diffraction pattern ring in (b) [53].

because there is no preferential site (grain boundary) for corrosion initiation. Therefore, a uniform $Mg(OH)_2$ layer forms on the surface. However, the presence of grain boundaries in a bi-crystal or polycrystalline Mg would stimulate the preferred corrosion initiation at grain boundaries and hence increase the corrosion rate. More grain boundaries are expected to result in more non-uniform corrosion. However, a significant increase in the area of grain boundaries, which can be attained through SPD, can lead to rapid formation of an $Mg(OH)_2$ layer that is more stable and better adherent to the substrate, thereby increasing the corrosion resistance [103]. This is because if a high density of grain boundaries are present in the microstructure of Mg, then the oxide that forms on the boundary regions in Mg, which is beneath the $Mg(OH)_2$ layer, may have a better coherency with the Mg matrix [152]. A fine-grained microstructure may also provide a means to relieve the stresses through the grain-boundary diffusion of vacancies, thus decreasing the degree of cracking in the MgO layer [152]. Kim and Kim [53] observed the formation of many MgO nanocrystals in a small-grained Mg substrate below the MgO layer (Fig. 33), which was attributed to the diffusion of oxygen atoms from the surface to the grain boundaries of the matrix. This formation of MgO nanocrystals may contribute to the stability of the MgO film by decreasing the sharpness of the stress gradient across the boundary between the MgO layer and the Mg substrate.

The corrosion mechanisms of pure Mg and Mg alloys before and after conventional and severe plastic deformation are schematically summarized in Fig. 34. Pure cast Mg usually has large grains (Fig. 34(a1)). Therefore, its corrosion resistance is poor. Conventional deformation, such as extrusion and rolling at high temperatures, refines the grains of pure Mg; however, a bimodal structure is typical in this process (Fig. 34(a2)). Therefore, the corrosion rate will still be high. After severe plastic deformation, however, ultrafine grains or even nanograins with a uniform grain size distribution can be achieved. If a high density of dislocations is present in the ultrafine-grained microstructure, however, the corrosion rate will be poor, despite significant grain refinement

(Fig. 34(a3)). Running SPD at higher temperatures or annealing after SPD at low temperatures can remove the dislocations in the grain interior and near the grain boundaries, which thereby decreases the corrosion rate (Fig. 34(a4)). When the SPD temperature or annealing temperature/time after SPD is too high/long, however, a grain-size increase due to grain growth occurs, which will decrease the corrosion resistance (Fig. 34(a5)).

In the case of alloys, there are two types of secondary phases, which are cathodic or anodic to the Mg matrix. A case when secondary phases exhibit the cathodic effect is shown in Fig. 34(b). The as-cast alloy with a continuous net-like phase has a low corrosion rate because the continuous phase acts as a barrier against corrosion progression (Fig. 34(b1)). However, when the secondary phase is not continuous and/or its electrochemical potential difference with the matrix is too high, this barrier effect will decrease. Thus, when the net-like phase is broken up during plastic deformation, corrosion will be accelerated near the secondary phases due to the micro-galvanic corrosion effect (Fig. 34(b2)). SPD is effective in breaking up the secondary phase to fine particles and uniformly dispersing the particles over the matrix. Therefore, if the refinement effect of the secondary phase is significant together with the grain refinement effect, uniform corrosion can occur despite the presence of the secondary phase. Then, the corrosion rate of the SPDed Mg alloys with a discontinuous cathodic secondary phase can be lower than that of their cast counterparts with a continuous net-like secondary phase. When the SPD temperature is sufficiently high or the SPDed samples are properly annealed, dislocations and secondary phases can be greatly removed (Fig. 34(b4)), resulting in a decrease in the corrosion rate. Increasing the SPD temperature or the annealing temperature beyond the optimum temperature, however, can increase rather than decrease the corrosion rate because of the pronounced grain-size increase by large grain growth (Fig. 34(b5)). As the presence of fine secondary phase particles is expected to retard grain growth, small grains can be retained during the annealing process for the removal of dislo-
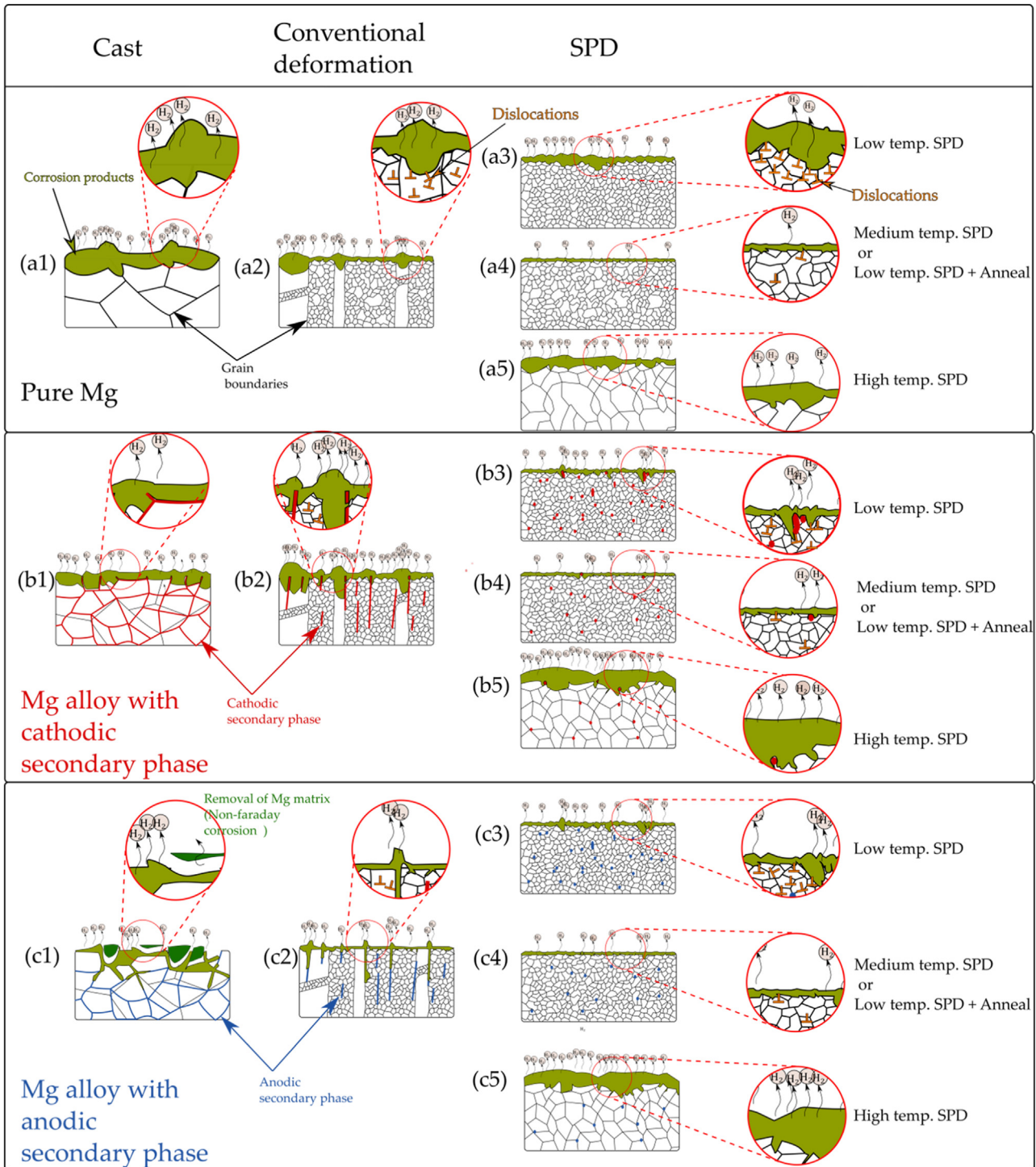
A. Bahmani, M. Lotfpour, M. Taghizadeh et al.

Fig. 34. Schematic summary of the corrosion mechanisms of Mg and Mg alloys after conventional deformation and severe plastic deformation.

cations in the alloys. which is advantageous for improving the corrosion resistance through grain-size reduction compared to pure Mg.

The cast alloy with an anodic secondary phase (Fig. 34(c1)) has a continuous and net-like secondary phase that will be preferentially corroded under immersion, increasing the susceptibility to non-Faradaic corrosion. In this case,

corrosion can easily attack inside the material by corroding the secondary phase that decorates the grain boundaries. The effective refinement and uniform dispersion of the anodic secondary phase via SPD and the removal of dislocations through static recovery or recrystallization by annealing can lead to the formation of microstructures, where nano-sized anodic secondary phase particles are uniformly dis-

persed in a fine-grained matrix with a low dislocation density. From this microstructure, the best corrosion resistance can be achieved.

7. Summary

The corrosion behavior of magnesium alloys after various severe plastic deformation processes was reviewed qualitatively and quantitatively. First, the effects of microstructural features on the corrosion of magnesium alloys were classified, and the effects of various solutions on the corrosion behavior of magnesium alloys were addressed. Then, the effects of the microstructure parameters, such as the grain size and secondary phase on the corrosion rate and corrosion behavior of magnesium alloys before and after SPD were analyzed. In addition, the effects of different SPD techniques on both the mechanical and corrosion properties of magnesium alloys were analyzed, and based on the analysis results the best strategies for simultaneously enhancing both the mechanical and corrosion properties of the Mg materials were proposed. Finally, alterations of the corrosion mechanisms after SPD were discussed by investigating the characteristics of the corroded surface after immersion in solution media. In summary, the following conclusions and suggestions can be presented here.

1. Severe plastic deformation techniques have a significantly positive effect on both the corrosion and mechanical properties of magnesium alloys. This simultaneous significant improvement of both the mechanical and corrosion properties shows a promising future for the application of SPD methods in producing high-performance Mg components.
2. Corrosion-rate reduction has been reported from most of the studied SPD techniques, regardless of the type of SPD. However, control of the processing conditions, which is different in different SPD methods, is crucial for achieving this goal.
3. It was determined that the grain size can decrease the corrosion rate of magnesium alloys after SPD due to the barrier function of grain boundaries for PCP corrosion and the formation of a stable passivation layer on the surface of fine grains. Solution media with less aggressive ions, such as Cl^-, appears to respond more effectively with respect to the grain-size reduction.
4. Dislocations that are formed after severe plastic deformation deteriorate the corrosion resistance of the interior grains. Therefore, proper annealing after severe plastic deformation is important. Another option is to determine the optimal processing temperature for SPD, which is not too low to create a high density of dislocations, and not too high to lose the grain refinement effect offered by SPD.
5. Texture has a significant effect on the corrosion behavior of Mg alloys. This is because the work function is different on different crystallographic planes. Basal planes with the highest planar density are more corrosion resistant than other planes. The basal texture and fine grains can exert a synergistic effect on improving the corrosion resistance.
6. Secondary phases are the source of precipitation hardening and therefore can enhance the yield and ultimate strengths. However, in the case of corrosion behavior, they act as the second part of a galvanic cell and thus accelerate the corrosion phenomena. Therefore, their fraction, distribution and size are critical in improving the corrosion properties of Mg alloys. After SPD, secondary phases can be fragmented and even dissolved into the matrix, depending on the SPD temperature. If the broken secondary particles are finely and uniformly distributed over the well-refined matrix, corrosion can occur uniformly, leading to suppression of accelerated and localized corrosion by micro-galvanic corrosion.

Suggestions

1. Solution treatment prior to SPD can greatly improve the formability and hence allows for effective grain refinement through SPD. The obtained material after the solution treatment followed by SPD will have fine grains with a small number of secondary phase particles. Thus, good corrosion resistance is expected from this type of microstructure. However, to achieve a high strength, a proper aging or precipitation process is suggested.
2. Choosing elements for the secondary phase that have a low potential difference relative to the matrix can decrease the negative role of micro-galvanic cells in corrosion. The addition of alloying elements such as Al, Ca and Y can improve the passivity. Proper addition of these elements can also enhance the mechanical properties.

Conflicts of interest

None.

Acknowledgements

Supplementary materials

Supplementary material associated with this article can be found, in the online version, at doi:10.1016/j.jma.2022.09.007.

References

[1] T. Xu, Y. Yang, X. Peng, J. Song, F. Pan, J. Magnes. Alloy. 7 (3) (2019) 536–544.
[2] F. Cao, Z. Shi, G.L. Song, M. Liu, M.S. Dargusch, A. Atrens, Corros. Sci. 90 (2015) 176–191.
[3] A. Atrens, G.L. Song, M. Liu, Z. Shi, F. Cao, M.S. Dargusch, Adv. Eng. Mater. 17 (4) (2015) 400–453.
[4] M.K. Kulekci, Int. J. Adv. Manuf. Technol. 39 (9-10) (2007) 851–865.

[5] A.A. Luo, A.K. Sachdev, Advances in Wrought Magnesium Alloys 2012, Woodhead Publishing Limited, pp. 393-426. doi:10.1533/9780857093844.3.393.

[6] A.A. Luo, J. Magnes. Alloy. 1 (1) (2013) 2–22.

[7] A. Luo, J. Mater. Manuf. 114 (2005) 411–421.

[8] B.R. Powell, A.A. Luo, P.E. Krajewski, Adv. Mater. Automot. Eng. (2012) 150–209, doi:10.1533/9780857095466.150.

[9] W.A. Monteiro, Light Met. Alloy. Appl. (2014) 229–241 Chapter 10, doi:10.5772/58460.

[10] L. Ren, L. Fan, M. Zhou, Y. Guo, Y. Zhang, C.J. Boehlert, G. Quan, Int. J. Lightweight Mater. Manuf. 1 (2) (2018) 81–88.

[11] E. Nyberg, J. Peng, N.R. Neelameggham, Magnes. Technol. 2016 (2016) 7–8.

[12] A. Wendt, K. Weiss, A. Ben-Dov, M. Bamberger, B. Bronfin, S.N. Mathaudhu, A.A. Luo, N.R. Neelameggham, E.A. Nyberg, W.H. Sillekens, in: Essential Readings in Magnesium Technology, Springer International Publishing, Cham, 2016, pp. 65–69.

[13] I. Ostrovsky, Y. Henn, New challenges in aeronautics, ASTEC'07, Moscow, 2007.

[14] S. Agarwal, J. Curtin, B. Duffy, S. Jaiswal, Mater. Sci. Eng. C Mater. Biol. Appl. 68 (2016) 948–963.

[15] P. Sekar, S. Narendranath, V. Desai, J. Magnes. Alloy. 15 (2021) 1147–1163.

[16] A. Atrens, G.L. Song, F. Cao, Z. Shi, P.K. Bowen, J. Magnes. Alloy. 1 (3) (2013) 177–200.

[17] R.Z. Valiev, R.K. Islamgaliev, I.V. Alexandrov, Prog. Mater. Sci. 45 (2) (2000) 103–189.

[18] A. Azushima, R. Kopp, A. Korhonen, D.Y. Yang, F. Micari, G. Lahoti, P. Groche, J. Yanagimoto, N. Tsuji, A. Rosochowski, CIRP Ann. 57 (2) (2008) 716–735.

[19] G. Faraji, H.S. Kim, H.T. Kashi, Severe Plastic Deformation: Methods, Processing and Properties, Elsevier, 2018.

[20] G. Faraji, H.S. Kim, Mater. Sci. Technol. 33 (8) (2016) 905–923.

[21] E. Bagherpour, N. Pardis, M. Reihanian, R. Ebrahimi, Int. J. Adv. Manuf. Technol. 100 (5-8) (2019) 1647–1694.

[22] Y. Sun, C. Shen, Q. Lai, W. Liu, D.W. Wang, K.F. Aguey-Zinsou, Energy Storage Mater. 10 (2018) 168–198.

[23] W.J. Kim, J.D. Park, W.Y. Kim, J. Alloy. Compd. 460 (1-2) (2008) 289–293.

[24] Y.H. Ji, J.J. Park, W.J. Kim, Mater. Sci. Eng. A Struct. Mater. 454-455 (2007) 570–574.

[25] W.Y. Kim, W.J. Kim, Mater. Sci. Eng. A Struct. Mater. 594 (2014) 189–192.

[26] X. Liu, S. Chen, J.K.H. Tsoi, J.P. Matinlinna, Regen. Biomater. 4 (5) (2017) 315–323.

[27] C.N. Elias, J.H.C. Lima, R. Valiev, M.A. Meyers, JOM 60 (3) (2008) 46–49.

[28] B.J. Luthringer, F. Feyerabend, R. Willumeit-Romer, Magnes. Res. 27 (4) (2014) 142–154.

[29] G.E. Jai Poinern, S. Brundavanam, D. Fawcett, Am. J. Biomed. Eng. 2 (6) (2013) 218–240.

[30] S. Jafari, S.E. Harandi, R.K. Singh Raman, JOM 67 (5) (2015) 1143–1153.

[31] G. Qiang, E. Mostaed, C. Zanella, Y. Zhentao, M. Vedani, Rare Met. Mater. Eng. 43 (11) (2014) 2561–2566.

[32] Y.F. Zheng, X.N. Gu, F. Witte, Mater. Sci. Eng. R Rep. 77 (2014) 1–34.

[33] Q. Chen, G.A. Thouas, Mater. Sci. Eng. R Rep. 87 (2015) 1–57.

[34] S. Qiao, Y. Wang, R. Zan, H. Wu, Y. Sun, H. Peng, R. Zhang, Y. Song, J. Ni, S. Zhang, X. Zhang, ACS Biomater. Sci. Eng. 6 (3) (2020) 1755–1763.

[35] N. Anisimova, M. Kiselevskiy, N. Martynenko, B. Straumal, R. Willumeit-Römer, S. Dobatkin, Y. Estrin, J. Biomed. Mater. Res. B Appl. Biomater. 108 (1) (2020) 167–173.

[36] C. Shuai, L. Liu, Y. Yang, C. Gao, M. Zhao, L. Yi, S. Peng, Appl. Sci. 8 (11) (2018) 2109.

[37] Y. Wu, G. He, Y. Zhang, Y. Liu, M. Li, X. Wang, N. Li, K. Li, G. Zheng, Y. Zheng, Q. Yin, Sci. Rep. 6 (1) (2016) 21736.

[38] Y. Estrin, N. Martynenko, N. Anisimova, D. Temralieva, M. Kiselevskiy, V. Serebryany, G. Raab, B. Straumal, B. Wiese, R. Willumeit-Romer, S. Dobatkin, Materials 12 (23) (2019) (Basel).

[39] W.Q. Huang, W.Q. Long, X.F. Mo, N.Q. Zhang, H. Luo, F.Y. Lin, J. Huang, C.X. Zhang, Sci. Rep. 9 (1) (2019) 5764.

[40] A.M. Jorge Jr, E. Prokofiev, M.R.M. Triques, V. Roche, W.J. Botta, C.S. Kiminami, G.I. Raab, R.Z. Valiev, T.G. Langdon, Int. J. Hydrog. Energy 42 (34) (2017) 21822–21831.

[41] I. Sabirov, N.A. Enikeev, M.Y. Murashkin, R.Z. Valiev, Bulk Nanostructured Materials with Multifunctional Properties, SpringerBriefs in Materials, 2015, pp. 101–113, doi:10.1007/978-3-319-19599-5_4.

[42] D. Eliezer, G. Hamu, C.E. Cross, T. Böllinghaus, Effect of grain refinement on the strength and corrosion of AZ31 magnesium alloy following severe plastic deformation, (2006).

[43] H. Wang, Y. Estrin, H. Fu, G. Song, Z. Zúberová, Adv. Eng. Mater. 9 (11) (2007) 967–972.

[44] J. Zhang, X. Ou, D. Yang, Z. Sun, J. Wuhan Univ. Technol. Mater. Sci. Ed. 24 (4) (2009) 515–519.

[45] R.C. Zeng, J. Chen, W. Dietzel, R. Zettler, J.F. dos Santos, M.L. Nascimento, K.U. Kainer, Corros. Sci. 51 (8) (2009) 1738–1746.

[46] H. Seifiyan, M. Heydarzadeh Sohi, M. Ansari, D. Ahmadkhaniha, M. Saremi, J. Magnes. Alloy. 7 (4) (2019) 605–616.

[47] R.S. Mishra, Z.Y. Ma, Mater. Sci. Eng. R Rep. 50 (1-2) (2005) 1–78.

[48] Z. Pu, O. Dillon Jr, I. Jawahir, D. Puleo, in: Proceedings of the International Manufacturing Science and Engineering Conference, 2010, pp. 271–277.

[49] Z. Pu, O.W. Dillon, D.A. Puelo, I.S. Jawahir, T.S.N.S. Narayanan, I.S. Park, M.H. Lee, in: Surface Modification of Magnesium and its Alloys for Biomedical Applications, Woodhead Publishing, 2015, pp. 103–133.

[50] J.H. Gao, S.K. Guan, Z.W. Ren, Y.F. Sun, S.J. Zhu, B. Wang, Mater. Lett. 65 (4) (2011) 691–693.

[51] D. Ahmadkhaniha, Y. Huang, M. Jaskari, A. Järvenpää, M.H. Sohi, C. Zanella, L.P. Karjalainen, T.G. Langdon, J. Mater. Sci. 53 (24) (2018) 16585–16597.

[52] T.J. Lee, W.J. Kim, J. Alloy. Compd. 817 (2020) 153298.

[53] H.S. Kim, W.J. Kim, Corros. Sci. 75 (2013) 228–238.

[54] Z. Shi, W.J. Kim, F. Cao, M.S. Dargusch, A. Atrens, J. Magnes. Alloy. 3 (4) (2015) 271–282.

[55] P. Trivedi, K. Nune, R. Misra, Surf. Coat. Technol. 315 (2017) 250–257.

[56] A. Bahmani, S. Arthanari, K.S. Shin, J. Alloy. Compd. 856 (2021).

[57] A. Bahmani, S. Arthanari, K.S. Shin, Int. J. Adv. Manuf. Technol. 105 (2019) 785–797.

[58] S. Dobatkin, E. Lukyanova, N. Martynenko, N.Y. Anisimova, M. Kiselevskiy, M. Gorshenkov, N.Y. Yurchenko, G.I. Raab, V. Yusupov, N. Birbilis, IOP Conf. Ser. Mater. Sci. Eng. 194 (2017) 012004.

[59] M. Diez, H.E. Kim, V. Serebryany, S. Dobatkin, Y. Estrin, Mater. Sci. Eng. A Struct. Mater. 612 (2014) 287–292.

[60] A. Bahmani, S. Arthanari, K.S. Shin, J. Alloy. Compd. 813 (2020) 152155.

[61] L. Lu, T. Liu, J. Chen, Z. Wang, Mater. Des. 1980-2015 (36) (2012) 687–693.

[62] M.R. Sahu, T.S.S. Kumar, U. Chakkingal, Trans. Indian Inst. Met. 74 (2021) 791–798.

[63] B.R. Sunil, A.A. Kumar, T.S. Sampath Kumar, U. Chakkingal, Mater. Sci. Eng. C Mater. Biol. Appl. 33 (3) (2013) 1607–1615.

[64] R. Sundar, P. Ganesh, R.K. Gupta, G. Ragvendra, B.K. Pant, V. Kain, K Rakesh, R. Kaul, K.S. Bindra, Lasers Manuf. Mater. Process. 6 (4) (2019) 424–463.

[65] Y. Guo, S. Wang, W. Liu, T. Xiao, G. Zhu, Z. Sun, Metals 9 (11) (2019) 1237.

[66] S.Q. Zhu, H.G. Yan, J.H. Chen, Y.Z. Wu, B. Su, Y.G. Du, X.Z. Liao, Scr. Mater. 67 (4) (2012) 404–407.

[67] X. Feng, Y. Sun, X. Feng, J. He, S. Wan, Russ. J. Non Ferr. Met. 61 (6) (2020) 658–666.

[68] C. Wang, Z. Yu, Y. Cui, S. Yu, X. Ma, H. Liu, Met. Sci. Heat Treat. 60 (11-12) (2019) 777–782.

ARTICLE IN PRESS

[69] N. Martynenko, E. Luk'yanova, M. Morozov, V. Yusupov, S. Dobatkin, Y.Z. Estrin, Met. Sci. Heat Treat. 60 (3-4) (2018) 253–258.

[70] W.T. Huo, W. Zhang, J.W. Lu, Y.S. Zhang, J. Alloy. Compd. 720 (2017) 324–331.

[71] H. Cao, W. Huo, S. Ma, Y. Zhang, L. Zhou, Materials 11 (7) (2018) 1–16 (Basel), doi:10.3390/ma11071232.

[72] V.C. Shunmugasamy, E. Khalid, B. Mansoor, Mater. Today Commun. 26 (2021) 1–12, doi:10.1016/j.mtcomm.2021.102129.

[73] B. Sułkowski, M. Janoska, G. Boczkal, R. Chulist, M. Mroczkowski, P. Pałka, J. Magnes. Alloy. 8 (3) (2020) 761–768.

[74] W. Zhao, D. Liu, R. Chiang, H. Qin, X. Zhang, H. Zhang, J. Liu, Z. Ren, R. Zhang, G.L. Doll, V.K. Vasudevan, Y. Dong, C. Ye, J. Mater. Process. Technol. 285 (2020).

[75] X. Hou, H. Qin, H. Gao, S. Mankoci, R. Zhang, X. Zhou, Z. Ren, G.L. Doll, A. Martini, N. Sahai, Y. Dong, C. Ye, Mater. Sci. Eng. C Mater. Biol. Appl. 78 (2017) 1061–1071.

[76] R. Bertolini, S. Bruschi, A. Ghiotti, L. Pezzato, M. Dabalà, Procedia CIRP 71 (2018) 105–110.

[77] M. Efe, W. Moscoso, K.P. Trumble, W.D. Compton, S. Chandrasekar, Acta Mater. 60 (5) (2012) 2031–2042.

[78] R. Bertolini, S. Bruschi, A. Ghiotti, Procedia Manuf. 26 (2018) 217–227.

[79] T. Mineta, H. Sato, Mater. Sci. Eng. A Struct. Mater. 735 (2018) 418–422.

[80] N. Fakhar, M. Sabbaghian, J. Alloy. Compd. 862 (2021) 1–10, doi:10.1016/j.jallcom.2020.158334.

[81] D. Fabijanic, A. Taylor, K.D. Ralston, M.X. Zhang, N. Birbilis, Corrosion 69 (6) (2012) 527–535.

[82] N. Li, Y.D. Li, Y.X. Li, Y.H. Wu, Y.F. Zheng, Y. Han, Mater. Sci. Eng. C Mater. Biol. Appl. 35 (2014) 314–321.

[83] M.T. Pérez-Prado, D. Valle, O.A. Ruano, Scr. Mater. 51 (11) (2004) 1093–1097.

[84] A. Nikfahm, I. Danaee, A. Ashrafi, M.R. Toroghinejad, Trans. Indian Inst. Met. 67 (1) (2014) 115–121.

[85] B.R. Sunil, T.S. Kumar, U. Chakkingal, V. Nandakumar, M. Doble, V.D. Prasad, M. Raghunath, Mater. Sci. Eng. C 59 (2016) 356–367.

[86] A. Bahmani, K.S. Shin, in: Effects of Severe Plastic Deformation on Mechanical Properties and Corrosion Behavior of Magnesium Alloys, Springer International Publishing, Cham, 2018, pp. 369–371.

[87] K.S. Shin, A. Bahmani, Magnesium alloy having excellent strength and corrosion resistance and manufacturing method for the same, Korean Patents, Korea, 2020.

[88] https://www.scopus.com/.

[89] https://scholar.google.com/.

[90] M. Ben-Haroush, G. Ben-Hamu, D. Eliezer, L. Wagner, Corros. Sci. 50 (6) (2008) 1766–1778.

[91] G. Song, A. Atrens, Adv. Eng. Mater. 5 (12) (2003) 837–858.

[92] A. Atrens, Z. Shi, S.U. Mehreen, S. Johnston, G.L. Song, X. Chen, F. Pan, J. Magnes. Alloy. 8 (2020) 989–998.

[93] M.A. Meyers, K.K. Chawla, Cambridge University Press, 2008.

[94] A. Bahmani, S. Arthanari, K.S. Shin, J. Magnes. Alloy. 8 (2020) 134–149.

[95] D. Song, A. Ma, J. Jiang, P. Lin, D. Yang, J. Fan, Corros. Sci. 52 (2) (2010) 481–490.

[96] D. Song, A.B. Ma, J.H. Jiang, P.H. Lin, D.H. Yang, J.F. Fan, Corros. Sci. 53 (1) (2011) 362–373.

[97] J. Chen, G. Chen, H. Yan, B. Su, X. Gong, B. Zhou, J. Mater. Eng. Perform. 26 (10) (2017) 4748–4759.

[98] K.D. Ralston, N. Birbilis, C.H.J. Davies, Scr. Mater. 63 (12) (2010) 1201–1204.

[99] C.S. Obayi, R. Tolouei, A. Mostavan, C. Paternoster, S. Turgeon, B.A. Okorie, D.O. Obikwelu, D. Mantovani, Biomatter 6 (2016) e959874.

[100] K.D. Ralston, D. Fabijanic, N. Birbilis, Electrochim. Acta 56 (4) (2011) 1729–1736.

[101] T. Zheng, Y. Hu, S. Yang, J. Magnes. Alloy. 5 (2017) 404–411.

[102] Z. Li, S.J. Zhou, N. Huang, Int. J. Miner. Metall. Mater. 22 (6) (2015) 639–647.

[103] N. Birbilis, K.D. Ralston, S. Virtanen, H.L. Fraser, C.H.J. Davies, Sci. Technol. 45 (3) (2010) 224–230.

[104] C. op't Hoog, N. Birbilis, Y. Estrin, Adv. Eng. Mater. 10 (6) (2008) 579–582.

[105] K.D. Ralston, N. Birbilis, Corrosion 66 (7) (2010) 075005-075005-13.

[106] S. Gollapudi, Corros. Sci. 62 (2012) 90–94.

[107] S. Pawar, T.J.A. Slater, T.L. Burnett, X. Zhou, G.M. Scamans, Z. Fan, G.E. Thompson, P.J. Withers, Acta Mater. 133 (2017) 90–99.

[108] A. Bahmani, K.S. Shin, Corrosion 76 (8) (2020) 750–765.

[109] G. Han, J.Y. Lee, Y.C. Kim, J.H. Park, D.I. Kim, H.S. Han, S.J. Yang, H.K. Seok, Corros. Sci. 63 (2012) 316–322.

[110] D. Ahmadkhaniha, M. Fedel, M. Heydarzadeh Sohi, F. Deflorian, Surf. Eng. Appl. Electrochem. 53 (5) (2017) 439–448.

[111] C.D. Lee, C.S. Kang, K.S. Shin, Met. Mater. 6 (5) (2000) 441.

[112] C.D. Lee, C.S. Kang, K.S. Shin, Met. Mater. 6 (4) (2000) 351–358.

[113] M.F. Hurley, C.M. Efaw, P.H. Davis, J.R. Croteau, E. Graugnard, N. Birbilis, Corrosion 71 (2) (2015) 160–170.

[114] N. Birbilis, M.A. Easton, A.D. Sudholz, S.M. Zhu, M.A. Gibson, Corros. Sci. 51 (3) (2009) 683–689.

[115] P. Jiang, C. Blawert, M.L. Zheludkevich, Corros. Mater. Degrad. 1 (2) (2020) 92–158.

[116] P.P. Wu, F.J. Xu, K.K. Deng, F.Y. Han, Z.Z. Zhang, R. Gao, Corros. Sci. 127 (2017) 280–290.

[117] Y.S. Jeong, W.J. Kim, Corros. Sci. 82 (2014) 392–403.

[118] H.Y. Choi, W.J. Kim, J. Alloy. Compd. 696 (2017) 736–745.

[119] H.Y. Choi, W.J. Kim, J. Alloy. Compd. 664 (2016) 25–37.

[120] J.Y. Choi, W.J. Kim, J. Alloy. Compd. 614 (2014) 49–55.

[121] M. Esmaily, J.E. Svensson, S. Fajardo, N. Birbilis, G.S. Frankel, S. Virtanen, R. Arrabal, S. Thomas, L.G. Johansson, Prog. Mater. Sci. 89 (2017) 92–193.

[122] H. Pan, K. Pang, F. Cui, F. Ge, C. Man, X. Wang, Z. Cui, Corros. Sci. 157 (2019) 420–437.

[123] C.Z. Zhang, S.J. Zhu, L.G. Wang, R.M. Guo, G.C. Yue, S.K. Guan, Mater. Des. 96 (2016) 54–62.

[124] K. Yasakau, Corros. Mater. Degrad. 1 (3) (2020) 345–372.

[125] P.R. Cha, H.S. Han, G.F. Yang, Y.C. Kim, K.H. Hong, S.C. Lee, J.Y. Jung, J.P. Ahn, Y.Y. Kim, S.Y. Cho, J.Y. Byun, K.S. Lee, S.J. Yang, H.K. Seok, Sci. Rep. 3 (2013) 2367.

[126] P. Priya, X. Yan, S. Chaudhuri, Comput. Mater. Sci. 175 (2020) 109541.

[127] Z. Luo, H. Zhu, T. Ying, D. Li, X. Zeng, Surf. Sci. 672-673 (2018) 68–74.

[128] R. Xin, Y. Luo, A. Zuo, J. Gao, Q. Liu, Mater. Lett. 72 (2012) 1–4.

[129] M. Liu, D. Qiu, M.C. Zhao, G. Song, A. Atrens, Scr. Mater. 58 (5) (2008) 421–424.

[130] K.S. Shin, M.Z. Bian, N.D. Nam, JOM 64 (6) (2012) 664–670.

[131] K. Hagihara, M. Okubo, M. Yamasaki, T. Nakano, Corros. Sci. 109 (2016) 68–85.

[132] G.L. Song, JOM 64 (6) (2012) 671–679.

[133] Q. Jiang, X. Ma, K. Zhang, Y. Li, X. Li, Y. Li, M. Ma, B. Hou, J. Magnes. Alloy. 3 (4) (2015) 309–314.

[134] B.J. Wang, D.K. Xu, Y.C. Xin, L.Y. Sheng, E.H. Han, Sci. Rep. 7 (1) (2017) 16014.

[135] R.S. Lillard, G.F. Wang, M.I. Baskes, J. Electrochem. Soc. 153 (2006) B358–B364.

[136] D.W. Li, H.Y. Wang, D.S. Wei, Z.X. Zhao, Y. Liu, ACS Omega 5 (3) (2020) 1448–1456.

[137] C. Zhang, S. Guan, L. Wang, S. Zhu, L. Chang, J. Mater. Res. 32 (6) (2017) 1061–1072.

[138] N.N. Aung, W. Zhou, Corros. Sci. 52 (2) (2010) 589–594.

[139] C. Yan, Y. Xin, X.B. Chen, D. Xu, P.K. Chu, C. Liu, B. Guan, X. Huang, Q. Liu, Nat. Commun. 12 (1) (2021) 4616.

[140] S. Bagherifard, D.J. Hickey, A.C. de Luca, V.N. Malheiro, A.E. Markaki, M. Guagliano, T.J. Webster, Biomaterials 73 (2015) 185–197.

[141] S. Dobatkin, S. Galkin, Y. Estrin, V. Serebryany, M. Diez, N. Martynenko, E. Lukyanova, V. Perezhogin, J. Alloy. Compd. 774 (2019) 969–979.

[142] M. Furukawa, Z. Horita, M. Nemoto, T. Langdon, J. Mater. Sci. 36 (12) (2001) 2835–2843.

[143] S. Galkin, Steel Transl. 44 (1) (2014) 61–64.

[144] H. Huang, J. Zhang, Mater. Sci. Eng. A Struct. Mater. 674 (2016) 52–58.

[145] Z. Ma, Metall. Mater. Trans. A 39 (3) (2008) 642–658.

[146] W. Polkowski, Differential Speed Rolling: A New Method For a Fabrication of Metallic Sheets with Enhanced Mechanical Properties, In-TechOpen, 2016.

[147] R.Z. Valiev, T.G. Langdon, Prog. Mater. Sci. 51 (7) (2006) 881–981.

[148] N. Martynenko, E. Lukyanova, M. Gorshenkov, M. Morozov, V. Yusupov, N. Birbilis, S. Dobatkin, Y. Estrin, Mater. Sci. Forum 941 (2018) 808–813.

[149] A.I. Alateyah, T.A. Aljohani, M.O. Alawad, H.A. El-Hafez, A.N. Al-mutairi, E.S. Alharbi, R. Alhamada, B.W. El-Garaihy, W.H. El-Garaihy, Metals 11 (2) (2021) 1–19, doi:10.3390/met11020363.

[150] D.H. Shin, I. Kim, J. Kim, Y.T. Zhu, Mater. Sci. Eng. A Struct. Mater. 334 (1) (2002) 239–245.

[151] G.B. Hamu, D. Eliezer, L. Wagner, J. Alloy. Compd. 468 (1-2) (2009) 222–229.

[152] D. Orlov, K.D. Ralston, N. Birbilis, Y. Estrin, Acta Mater. 59 (15) (2011) 6176–6186.

[153] I.A. Shahar, T. Hosaka, S. Yoshihara, B.J. MacDonald, Procedia Eng. 184 (2017) 423–431.

[154] W.J. Kim, C.W. An, Y.S. Kim, S.I. Hong, Scr. Mater. 47 (1) (2002) 39–44.

[155] G. Manjunath Naik, N. Sannayellappa, S. Selvin Satheesh Kumar, J. Met. Mater. Miner. 29 (2) (2019) 1–20, doi:10.14456/jmmm.2019.13.

[156] W.J. Kim, H.T. Jeong, Mater. Trans. 46 (2) (2005) 251–258.

[157] L.S. Wang, J.H. Jiang, B. Saleh, Q.Y. Xie, Q. Xu, H. Liu, A.B. Ma, Acta Metall. Sin. (Engl. Lett.) 33 (2020) 1180–1190.

[158] P. Sekar, N. Sanna, V. Desai, Mater. Corros. 71 (4) (2019) 571–584.

[159] A. Torkian, G. Faraji, M.S. Pedram, Rare Met. 40 (3) (2019) 651–662.

[160] B. Bagheri, M. Abbasi, Adv. Manuf. 8 (1) (2020) 82–96.

[161] M. Balakrishnan, I. Dinaharan, R. Palanivel, R. Sivaprakasam, J. Magnes. Alloy. 3 (1) (2015) 76–78.

[162] Q. Liu, Q.X. Ma, G.Q. Chen, X. Cao, S. Zhang, J.L. Pan, G. Zhang, Q.Y. Shi, Corros. Sci. 138 (2018) 284–296.

[163] D. Liu, M. Shen, Y. Tang, Y. Hu, L. Zhao, Met. Mater. Int. 25 (5) (2019) 1182–1190.

[164] K. Edalati, Z. Horita, Mater. Sci. Eng. A Struct. Mater. 652 (2016) 325–352.

[165] C.L. Silva, R.B. Soares, P.H.R. Pereira, R.B. Figueiredo, V.F. Lins, T.G. Langdon, Adv. Eng. Mater. 21 (3) (2019) 1801081.

[166] Y. Ivanisenko, R. Kulagin, V. Fedorov, A. Mazilkin, T. Scherer, B. Baretzky, H. Hahn, Mater. Sci. Eng. A Struct. Mater. 664 (Supplement C) (2016) 247–256.

[167] E.V. Parfenov, O.B. Kulyasova, V.R. Mukaeva, B. Mingo, R.G. Farrakhov, Y.V. Cherneikina, A. Yerokhin, Y.F. Zheng, R.Z. Valiev, Corros. Sci. 163 (2020) 1–32, doi:10.1016/j.corsci.2019.108303.

[168] A. Bahmani, W.J. Kim, Materials 13 (18) (2020) 1–22, doi:10.3390/ma13184159.

[169] W.J. Kim, B.G. Hwang, M.J. Lee, Y.B. Park, J. Alloy. Compd. 509 (34) (2011) 8510–8517.

[170] W.J. Kim, B.H. Lee, J.B. Lee, M.J. Lee, Y.B. Park, Scr. Mater. 63 (7) (2010) 772–775.

[171] W.J. Kim, S.I. Hong, J.M. Lee, S.H. Kim, Mater. Sci. Eng. A Struct. Mater. 559 (2013) 325–332.

[172] T.Y. Kwak, W.J. Kim, J. Mater. Sci. Mater. Med. 33 (9) (2017) 919–925.

[173] T.Y. Kwak, W.J. Kim, Mater. Sci. Eng. A Struct. Mater. 684 (2017) 284–291.

[174] T.Y. Kwak, H.K. Lim, S.H. Han, W.J. Kim, Scr. Mater. 103 (2015) 49–52.

[175] Y.H. Kim, W.J. Kim, Met. Mater. Int. 21 (2) (2015) 374–381.

[176] W.J. Kim, I.B. Park, Scr. Mater. 68 (3-4) (2013) 179–182.

[177] W.J. Kim, S.I. Hong, Y.H. Kim, Scr. Mater. 67 (7-8) (2012) 689–692.

[178] W.J. Kim, I.B. Park, S.H. Han, Scr. Mater. 66 (8) (2012) 590–593.

[179] W.J. Kim, I.K. Moon, S.H. Han, Mater. Sci. Eng. A Struct. Mater. 538 (2012) 374–385.

[180] W.J. Kim, H.W. Lee, S.J. Yoo, Y.B. Park, Mater. Sci. Eng. A Struct. Mater. 528 (3) (2011) 874–879.

[181] W.J. Kim, H.G. Jeong, H.T. Jeong, Scr. Mater. 61 (11) (2009) 1040–1043.

[182] W.J. Kim, Y.G. Lee, M.J. Lee, J.Y. Wang, Y.B. Park, Scr. Mater. 65 (2011) 1105–1108.

[183] Z.R. Zeng, Y.M. Zhu, R.L. Liu, S.W. Xu, C.H.J. Davies, J.F. Nie, N. Birbilis, Acta Mater. 160 (2018) 97–108.

[184] W.J. Kim, Y.J. Yoo, Mater. Sci. Eng. A Struct. Mater. 643 (2015) 47–50.

[185] J.W. Seong, W.J. Kim, Acta Biomater. 11 (2015) 531–542.

[186] Y. Saito, H. Utsunomiya, N. Tsuji, T. Sakai, Acta Mater. 47 (2) (1999) 579–583.

[187] X. Huang, N. Tsuji, N. Hansen, Y. Minamino, Mater. Sci. Eng. A Struct. Mater. 340 (1) (2003) 265–271.

[188] Y. Pei, Y. Gui, T. Huang, F. Chen, J. Guo, S. Zhong, Z. Song, Mater. Res. Express 7 (6) (2020) 1–11, doi:10.1088/2053-1591/ab9c61.

[189] S. Samiei, G. Dini, M. Ebrahimian-Hosseinabadi, Met. Mater. Int. (2022), doi:10.1007/s12540-022-01202-y.

[190] R. Zhang, D. Wang, S. Yuan, Mater. Des. 134 (C) (2017) 250–258 Supplement.

[191] S. Jaiswal, S. Agrawal, A. Dubey, D. Lahiri, Eng. Rep. 3 (1) (2020), doi:10.1002/eng2.12286.

[192] R. Łyszkowski, T. Czujko, R.A. Varin, J. Mater. Sci. 52 (5) (2017) 2902–2914.

[193] N.Y. Yurchenko, N.D. Stepanov, G.A. Salishchev, V.N. Serebryany, N.S. Martynenko, E.A. Lukyanova, L.L. Rokhlin, N. Birbilis, S.V. Dobatkin, Y.Z. Estrin, J. Magnes. Alloy. 10 (2021) 266–280.

[194] A. Takayama, X. Yang, H. Miura, T. Sakai, Mater. Sci. Eng. A Struct. Mater. 478 (1-2) (2008) 221–228.

[195] H. Miura, G. Yu, X. Yang, Mater. Sci. Eng. A Struct. Mater. 528 (22-23) (2011) 6981–6992.

[196] C. Cui, W. Zhang, W. Chen, J. He, X. Chen, J. Hou, J. Magnes. Alloy. (2021), doi:10.1016/j.jma.2021.01.001.

[197] Q.F. Zhu, L. Li, C.Y. Ban, Z.H. Zhao, Y.B. Zuo, J.Z. Cui, Trans. Nonferr. Met. Soc. China 24 (5) (2014) 1301–1306.

[198] H. Miura, W. Nakamura, M. Kobayashi, Procedia Eng. 81 (2014) 534–539.

[199] A. Bahmani, Development of High Strength and Corrosion Resistant Magnesium Alloys Using Severe Plastic Deformation Process, Seoul National University, 2018.

[200] Y. Yang, X. Chen, J. Nie, K. Wei, Q. Mao, F. Lu, Y. Zhao, Mater. Res. Lett. 9 (6) (2021) 255–262.

[201] B. Gigov, V. Tsonev, N. Nikolov, Y. Marcheva, N. Nikolov, S. Stoilova, I. Kralov, M. Todorov, V. Stoilov, in: Proceedings of the MATEC Web Conference, 234, 2018.

[202] T.K. Akopyan, A.S. Aleshchenko, N.A. Belov, S.P. Galkin, Phys. Met. Metall. 119 (3) (2018) 241–250.

[203] Y.M. Hwang, W.M. Tsai, F.H. Tsai, I. Her, Int. J. Mach. Tools Manuf. 46 (12-13) (2006) 1555–1562.

[204] Y. Li Wang, A. Molotnikov, M. Diez, R. Lapovok, H.E. Kim, J. Tao Wang, Y. Estrin, Mater. Sci. Eng. A Struct. Mater. 639 (Supplement C) (2015) 165–172.

[205] C.K. Shih, C. Hung, J. Mater. Process. Technol. 142 (3) (2003) 702–709.

[206] S. Bagherifard, I. Fernandez-Pariente, R. Ghelichi, M. Guagliano, Int. J. Fatigue 65 (2014) 64–70.

[207] S. Bagherifard, D.J. Hickey, S. Fintova, F. Pastorek, I. Fernandez–Pariente, M. Bandini, T.J. Webster, M. Guagliano, Acta Biomater. 66 (2018) 93–108.

[208] L. Trško, M. Guagliano, O. Bokůvka, F. Nový, Procedia Eng. 74 (2014) 246–252.

[209] C. Liu, H. Zheng, X. Gu, B. Jiang, J. Liang, J. Alloy. Compd. 770 (2019) 500–506.

[210] S. Bagherifard, D.J. Hickey, S. Fintová, F. Pastorek, I. Fernandez–Pariente, M. Bandini, T.J. Webster, M. Guagliano, Acta Biomater. 66 (2018) 93–108.

ARTICLE IN PRESS

JID: JMAA
[m5+;October 15, 2022;1:50]

A. Bahmani, M. Lotfpour, M. Taghizadeh et al.
Journal of Magnesium and Alloys xxx (xxxx) xxx

[211] S. Ramesh, G. Anne, H.S. Nayaka, S. Sahu, M.R. Ramesh, J. Mater. Eng. Perform. 28 (4) (2019) 2053–2062.

[212] H.S. Kim, W.J. Kim, Corros. Sci. 89 (2014) 331–337.

[213] S. Dobatkin, N. Martynenko, N. Anisimova, M. Kiselevskiy, D. Prosvirnin, V. Terentiev, N. Yurchenko, G. Salishchev, Y. Estrin, Materials 12 (21) (2019).

[214] Y. Zhang, M. Gao, I.P. Etim, L. Tan, K. Yang, Mater. Technol. 35 (7) (2020) 402–410.

[215] T. Hosaka, S. Yoshihara, I. Amanina, B.J. MacDonald, Procedia Eng. 184 (2017) 432–441.

[216] F. Zhang, A. Ma, J. Jiang, H. Xu, D. Song, F. Lu, Y. Nishida, Prog. Nat. Sci. Mater. Int. 23 (4) (2013) 420–424.

[217] H.S. Kim, G.H. Kim, H. Kim, W.J. Kim, Corros. Sci. 74 (2013) 139–148.

[218] N. Saikrishna, G. Pradeep Kumar Reddy, B. Munirathinam, B.R. Sunil, J. Magnes. Alloy. 4 (1) (2016) 68–76.

[219] E. Parfenov, O. Kulyasova, V. Mukaeva, B. Mingo, R. Farrakhov, Y.V. Cherneikina, A. Yerokhin, Y. Zheng, R. Valiev, Corros. Sci. 163 (2020) 108303.

[220] G. Cao, D. Zhang, W. Zhang, W. Zhang, Materials 9 (7) (2016) (Basel).

[221] F. Cao, Z. Shi, J. Hofstetter, P.J. Uggowitzer, G. Song, M. Liu, A. Atrens, Corros. Sci. 75 (2013) 78–99.

[222] F. Cao, Z. Shi, G.L. Song, M. Liu, A. Atrens, Corros. Sci. 76 (2013) 60–97.

[223] T. Zhang, Y. Shao, G. Meng, Z. Cui, F. Wang, Corros. Sci. 53 (5) (2011) 1960–1968.

[224] X. Zhang, G. Yuan, Z. Wang, Mater. Lett. 74 (2012) 128–131.

[225] G. Cao, D. Zhang, W. Zhang, C. Qiu, J. Alloy. Compd. 636 (2015) 12–19.

[226] M.K. Chung, Y.S. Choi, J.G. Kim, Y.M. Kim, J.C. Lee, Mater. Sci. Eng. A Struct. Mater. 366 (2) (2004) 282–291.

[227] S.G. Wang, C.B. Shen, K. Long, F. Zhang, F.H. Wang, Z.D. Zhang, J. Phys. Chem. B 110 (2006) 377–382.

[228] A. Balyanov, Scr. Mater. 51 (3) (2004) 225–229.

[229] M.C. Zhao, M. Liu, G.L. Song, A. Atrens, Corros. Sci. 50 (11) (2008) 3168–3178.

[230] W. Liu, F. Cao, A. Chen, L. Chang, J. Zhang, C. Cao, Corrosion 68 (2012) 045001.

[231] J. Przondziono, W. Walke, J. Szala, E. Hadasik, J. Wieczorek, IOP Conf. Ser. Mater. Sci. Eng. 22 (2011) 1–12, doi:10.1088/1757-899x/22/1/012017.

[232] S. Abbasi, M. Aliofkhazraei, H. Mojiri, M. Amini, M. Ahmadzadeh, M. Shourgeshty, Phys. Chem. Surf. 53 (3) (2017) 573–578.

[233] T. Kokubo, H. Takadama, Biomaterials 27 (15) (2006) 2907–2915.

[234] M. Lotfpour, C. Dehghanian, M. Emamy, A. Bahmani, M. Malekan, A. Saadati, M. Taghizadeh, M. Shokouhimehr, J. Magnes. Alloy. 15 (2021) 2078–2096.

[235] A. Bahmani, N. Hatami, N. Varahram, P. Davami, M.O. Shabani, Int. J. Adv. Manuf. Technol. 64 (9) (2013) 1313–1321.

[236] J. Campbell, Castings Practice: The 10 Rules of Casting, Butterworth-Heinemann, Oxford, 2004.

[237] H. Yu, Y. Xin, M. Wang, Q. Liu, J. Mater. Sci. Mater. Med. 34 (2) (2018) 248–256.

[238] J.W. Seong, W.J. Kim, Corros. Sci. 98 (2015) 372–381.

[239] Z. Shi, F. Cao, G.L. Song, M. Liu, A. Atrens, Corros. Sci. 76 (2013) 98–118.

[240] F. Cao, Corrosion and Stress Corrosion Cracking of Magnesium Alloys, University of Queensland PhD Thesis (2015).

[241] A. Bahmani, B. Nayebi, S. Bornay Zonoozi, L. Wang, M. Shokouhimehr, Mater. Charact. 167 (2020) 1–14, doi:10.1016/j.matchar.2020.110475.

[242] B. Ahmad, Development of High Strength and Corrosion Resistant Magnesium Alloys Using Severe Plastic Deformation Process, 서울대학교 대학원, 2018 bytes.

[243] Y.H. Jang, S.S. Kim, C.D. Yim, C.G. Lee, S.J. Kim, Sci. Technol. 42 (2) (2007) 119–122.

[244] G.R. Argade, S.K. Panigrahi, R.S. Mishra, Corros. Sci. 58 (2012) 145–151.

[245] G.R. Argade, S. Sanders, G. Mohandass, A. Alsaleh, F. D'Souza, T.D. Golden, R.S. Mishra, J. Mater. Eng. Perform. 28 (2) (2019) 852–862.

[246] Y. Ma, D. Wang, H. Li, F. Yuan, C. Yang, J. Zhang, Mater. Res. Express 7 (1) (2020) 015414.

[247] L. Li, T. Wang, Y. Wang, C.C. Zhang, H. Lv, H. Lin, W.B. Yu, C.J. Huang, J. Magnes. Alloy. 8 (2) (2020) 499–509.

[248] X. Zhang, G. Yuan, L. Mao, J. Niu, P. Fu, W. Ding, J. Mech. Behav. Biomed. Mater. 7 (2012) 77–86.

[249] X. Zhang, G. Yuan, J. Niu, P. Fu, W. Ding, J. Mech. Behav. Biomed. Mater. 9 (2012) 153–162.

[250] B. Homayun, A. Afshar, J. Alloy. Compd. 607 (2014) 1–10.

[251] H.R. Bakhsheshi Rad, M.H. Idris, M.R.A. Kadir, S. Farahany, A. Fereidouni, M.Y. Yahya, Appl. Mech. Mater. 121-126 (2011) 568–572.

[252] H.R. Bakhsheshi-Rad, M.H. Idris, M.R. Abdul-Kadir, A. Ourdjini, M. Medraj, M. Daroonparvar, E. Hamzah, Mater. Des. 53 (2014) 283–292.

[253] H.R. Bakhsheshi-Rad, E. Hamzah, S. Farahany, M.P. Staiger, J. Mater. Eng. Perform. 24 (2) (2014) 598–608.

[254] V. Bazhenov, A. Koltygin, A. Komissarov, A. Li, V. Bautin, R. Khasenova, A. Anishchenko, A. Seferyan, J. Komissarova, Y. Estrin, J. Magnes. Alloy. 8 (2) (2020) 352–363.

[255] Z. Gui, Z. Kang, Y. Li, J. Alloy. Compd. 685 (2016) 222–230.

[256] A. Pardo, M.C. Merino, A.E. Coy, F. Viejo, R. Arrabal, S. Feliú, Electrochim. Acta 53 (27) (2008) 7890–7902.

[257] A. Pardo, M.C. Merino, A.E. Coy, R. Arrabal, F. Viejo, E. Matykina, Corros. Sci. 50 (3) (2008) 823–834.

[258] Z. Gui, Z. Kang, Y. Li, Mater. Sci. Eng. C Mater. Biol. Appl. 96 (2019) 831–840.

[259] T.S. Orlova, A.V. Ankudinov, A.M. Mavlyutov, N.N. Resnina, Adv. Mater. 57 (1) (2018) 110–115.

[260] R.K. Khisamov, I.M. Safarov, R.R. Mulyukov, Y.M. Yumaguzin, Phys. Solid State 55 (1) (2013) 1–4.

[261] D.Y. Li, MRS Proc. 887 (2005) 1–9, doi:10.1557/PROC-0887-Q05-03.

[262] G.M. Naik, S. Narendranath, S.S. Kumar, J. Mater. Eng. Perform. 28 (5) (2019) 2610–2619.

[263] F.F. Cao, K.K. Deng, K.B. Nie, J.W. Kang, H.Y. Niu, J. Alloy. Compd. 770 (2019) 1208–1220.

[264] H.Y. Choi, W.J. Kim, J. Mech. Behav. Biomed. Mater. 51 (2015) 291–301.

[265] R. Zeng, K.U. Kainer, C. Blawert, W. Dietzel, J. Alloy. Compd. 509 (13) (2011) 4462–4469.

[266] D. Song, A. Ma, J. Jiang, P. Lin, D. Yang, J. Fan, Corros. Sci. 53 (1) (2011) 362–373.

[267] M. Gholami-Kermanshahi, V.D. Neubert, M. Tavakoli, F. Pastorek, B. Smola, V. Neubert, Adv. Eng. Mater. 20 (10) (2018) 1800121.

[268] P. Minárik, E. Jablonská, R. Král, J. Lipov, T. Ruml, C. Blawert, B. Hadzima, F. Chmelík, Mater. Sci. Eng. C 73 (2017) 736–742.

[269] N. Birbilis, K. Ralston, S. Virtanen, H. Fraser, C. Davies, Corros. Eng. Sci. Technol. 45 (3) (2010) 224–230.

[270] E. Mostaed, M. Vedani, M. Hashempour, M. Bestetti, Biomatter 4 (1) (2014) e28283.

[271] D. Song, C. Li, N. Liang, F. Yang, J. Jiang, J. Sun, G. Wu, A. Ma, X. Ma, Mater. Des. 166 (2019) 107621.

[272] L. Chen, Y. Sheng, X. Wang, X. Zhao, H. Liu, W. Li, Materials 11 (4) (2018) 551.

[273] M.G. Kim, J.K. Kim, H.S. Kim, W.J. Kim, J.H. Han, J. Korean Phys. Soc. 72 (6) (2018) 692–698.

[274] S.M. Baek, H.J. Kim, H.Y. Jeong, S.D. Sohn, H.J. Shin, K.J. Choi, K.S. Lee, J.G. Lee, C.D. Yim, B.S. You, H.Y. Ha, S.S. Park, Corros. Sci. 112 (2016) 44–53.

[275] S.M. Baek, J.S. Kang, H.J. Shin, C.D. Yim, B.S. You, H.Y. Ha, S.S. Park, Corros. Sci. 118 (2017) 227–232.

[276] B. Jiang, Q. Xiang, A. Atrens, J. Song, F. Pan, Corros. Sci. 126 (2017) 374–380.

[277] Q. Xiang, B. Jiang, Y. Zhang, X. Chen, J. Song, J. Xu, L. Fang, F. Pan, Corros. Sci. 119 (2017) 14–22.